



Delft University of Technology

A Journey on Quantum Sound

Developing a scalable platform for integrated hybrid quantum systems

Zivari, A.

DOI

[10.4233/uuid:35ea1e1f-b302-44de-874b-8faaf1e13993](https://doi.org/10.4233/uuid:35ea1e1f-b302-44de-874b-8faaf1e13993)

Publication date

2024

Document Version

Final published version

Citation (APA)

Zivari, A. (2024). *A Journey on Quantum Sound: Developing a scalable platform for integrated hybrid quantum systems*. [Dissertation (TU Delft), Delft University of Technology].
<https://doi.org/10.4233/uuid:35ea1e1f-b302-44de-874b-8faaf1e13993>

Important note

To cite this publication, please use the final published version (if applicable).
Please check the document version above.

Copyright

Other than for strictly personal use, it is not permitted to download, forward or distribute the text or part of it, without the consent of the author(s) and/or copyright holder(s), unless the work is under an open content license such as Creative Commons.

Takedown policy

Please contact us and provide details if you believe this document breaches copyrights.
We will remove access to the work immediately and investigate your claim.

A JOURNEY ON QUANTUM SOUND

DEVELOPING A SCALABLE PLATFORM FOR INTEGRATED
HYBRID QUANTUM SYSTEMS

A JOURNEY ON QUANTUM SOUND

**DEVELOPING A SCALABLE PLATFORM FOR INTEGRATED
HYBRID QUANTUM SYSTEMS**

Dissertation

for the purpose of obtaining the degree of doctor
at Delft University of Technology,
by the authority of the Rector Magnificus Prof. dr. ir. T.H.J.J. van der Hagen,
chair of the Board for Doctorates,
to be defended publicly on
27/05/2024 at 10:00 o'clock

by

AMIRPARSA ZIVARI

Master of Science in Electrical Engineering - Photonics,
Sharif University of Technology, Iran,
born in Tehran, Iran.

This dissertation has been approved by the promotor.

Composition of the doctoral committee:

Rector Magnificus,	voorzitter
Prof. dr. S. Gröblacher,	Technische Universiteit Delft, promotor
Prof. dr. L. (Kobus) Kuipers,	Technische Universiteit Delft, copromotor

Independent members:

Prof. dr. P.G. Steeneken,	Technische Universiteit Delft
Prof. dr. E. Verhagen,	TU Eindhoven / AMOLF
Prof. dr. W.G. van der Wiel,	University of Twente
Prof. dr. A. Schliesser,	University of Copenhagen
Dr. A. Bienfait,	Ecole Normale Supérieure de Lyon
Prof. dr. S. Otte,	Technische Universiteit Delft, reserve member



Keywords: quantum acoustics, integrated phononics, optomechanics, quantum optics

Printed by: Gildeprint, Enschede

Front & Back: Artistic depiction of quantum sound journey, conceived by Amirparsa Zivari in blender and the AI Midjourney.

Copyright © 2023 by A. Zivari

ISBN 978-94-6384-582-3 (Paperback)

ISBN 978-94-6384-583-0 (Ebook)

An electronic version of this dissertation is available at
<http://repository.tudelft.nl/>.

CONTENTS

Summary	vii
Samenvatting	ix
1 Introduction	1
1.1 Quantum networks	2
1.2 Hybrid quantum devices	3
1.2.1 Phonons as intermediaries	4
1.2.2 Phonons in quantum technology	5
1.3 Integrated systems	7
1.3.1 Integrated phononic technology	8
1.4 Quick summary of chapters	9
References	11
2 Non-classical mechanical states guided in a phononic waveguide	17
2.1 Introduction	19
2.2 Methods	19
2.3 Results	21
2.3.1 Basic and classical characterizations	21
2.3.2 Routing non-classical mechanical states	23
2.4 Conclusion and discussion	25
2.5 Supplementary Information	28
2.6 Appendix	39
References	41
3 On-chip distribution of quantum information using traveling phonons	45
3.1 Introduction	46
3.2 Methods	47
3.2.1 Device design	47
3.2.2 Theoretical studies of time-bin entanglement protocol	47
3.3 Results	49
3.3.1 Basic and classical characterizations	49
3.3.2 Time-bin phononic entanglement	51
3.3.3 Optomechanical bell test with time-bin entangled phonons	51
3.4 Conclusion and discussion	54
3.5 Supplementary Information	56
3.6 Appendix	63
References	66

4	A single-phonon directional coupler	71
4.1	Introduction	73
4.2	Device Design and Characterization	74
4.3	Coherent drive measurement	76
4.4	Single phonon splitting	78
4.5	Conclusion	80
4.6	Supplementary Information	81
4.7	Appendix	86
	References	89
5	Conclusion	93
	References	95
	Curriculum Vitæ	97
	List of Publications	99
	Acknowledgments	101

SUMMARY

Recently, quantum networks have emerged as a focal point of research and discussion due to their promise in overcoming the limitations of classical networks, offering unparalleled capabilities in secure communication, quantum computation, and distributed quantum information processing. Simply speaking, a quantum network is a network in which the nodes are capable of storing and processing quantum information and communicate via quantum channels. Unlike classical computers and networks, in which components at nodes and the interconnections between them are mostly made of electronics circuits, there is not a homogeneous system for all the applications in a quantum network. This in particular, increases the need for implementation of heterogeneous quantum systems. An important milestone in the development of hybrid quantum networks are the interconnections between different components at the nodes, which serve as quantum channels. A quantum channel is an interconnection between two quantum systems that can route carriers of quantum information, while preserving their coherence over the routing process. Finding such a channel, with carriers having the ability to couple to different quantum systems is not trivial. Although quanta of mechanical vibrations - known as "phonons" - have shown great potential for this task, as they can couple to many different types of quantum systems.

The aim of this thesis is to design an integrated platform using highly confined GHz phonons, with scalability as a primary consideration. This platform serves as an on-chip phononic quantum channel, enabling the ability to perform on-chip operations directly on single phonons on a chip. Moreover, the designed structures in this thesis are advantageous for advanced quantum acoustics experiments and pave the way towards having full coherent control on phonons on a chip.

In order to provide a foundation for our work, chapter 1 serves as an introduction. We give more details about quantum networks and the systems that are used in it, as quantum memories, processors, etc. We then give a quick overview over different phononic systems in a hybrid quantum network architecture, and the benefits of highly confined phonons. In chapter 2 we demonstrate a phononic quantum channel for routing single phonons, as the fundamental building block of our platform. The phononic waveguide is coupled to a single mode optomechanical cavity, which we use as a source and detector for exciting and detecting single phonons optomechanically. We study this platform experimentally both in the classical and in the quantum regime and we show its capability to excite, route and retrieve single phonons. However, the dispersion of the phononic waveguide limits the performance of our device. We further improve our design of the phononic waveguide in chapter 3, and show the ability to route a quantum state (a time-bin encoded superposition state) in our phononic channel. Routing quantum states without loss of coherence, is an essential requirement for every quantum channel. We further perform an optomechanical Bell-test to confirm the non-classical

nature of our system and to demonstrate its potential as a multimode optomechanical quantum memory. Moreover, we take one step further towards having more on-chip coherent control on phonons, by realizing a directional coupler for single phonons in chapter 4. This provides more ability to perform operations on single phonons on a chip directly, such as creating entanglement and superposition. At last, in chapter 5 we summarize the results discussed throughout this thesis and provide an outlook on how these findings may contribute to the future technologies and developments.

SAMENVATTING

Kwantumnetwerken zijn recent naar voren gekomen als een centraal onderzoeksonderwerp en discussieonderwerp vanwege hun belofte om de beperkingen van klassieke netwerken te overwinnen. Zij beloven ongeëvenaarde mogelijkheden op het gebied van veilige communicatie, kwantumrekenen en gedistribueerde kwantuminformatieverwerking. Simpel gezegd is een kwantumnetwerk een netwerk waarin de knooppunten in staat zijn kwantuminformatie op te slaan en te verwerken, en waarin de knooppunten communiceren via kwantumkanalen. In tegenstelling tot klassieke computers en netwerken, waarbij de componenten bij knooppunten en de verbindingen tussen hen voornamelijk bestaan uit elektronische circuits, is er geen homogeen systeem voor alle toepassingen in een kwantumnetwerk. Dit verhoogt met name de behoefte aan de implementatie van heterogene kwantumsystemen. Een belangrijke mijlpaal in de ontwikkeling van hybride kwantumnetwerken is de verbinding tussen verschillende componenten bij de knooppunten, die dienen als kwantumkanalen. Een kwantumkanaal is een verbinding tussen twee kwantumsystemen die dragers van kwantuminformatie kan routen, terwijl deze dragers hun coherentie behouden tijdens het routingsproces. Het vinden van zo een kanaal, waarbij de dragers het vermogen hebben om te koppelen aan verschillende kwantumsystemen, is niet triviaal. Kwanta van mechanische trillingen - bekend als "fononen"- bieden een groot potentieel voor deze taak, omdat ze kunnen koppelen aan veel verschillende soorten kwantumsystemen.

Het doel van dit proefschrift is het ontwerpen van een geïntegreerd platform dat gebruik maakt van sterk geconfineerde GHz-fononen, waarbij schaalbaarheid van groot belang is. Dit platform dient als een on-chip fononisch kwantumkanaal, waardoor de mogelijkheid ontstaat om on-chip bewerkingen rechtstreeks op enkele fononen op een chip uit te voeren. Bovendien zijn de ontworpen structuren in dit proefschrift voordelig voor geavanceerde kwantumakoestische experimenten. Ze maken de weg vrij voor volledige coherente controle over fononen op een chip.

In hoofdstuk 1 van dit proefschrift geven we een inleiding en beschrijven we de basis van ons werk. We geven meer details over kwantumnetwerken en de systemen die daarbij worden gebruikt, zoals kwantumgeheugens, processors, enzovoort. Daarna geven we een kort overzicht van verschillende fononische systemen in een hybride kwantumnetwerkarchitectuur, en de voordelen van sterk geconfineerde fononen. In hoofdstuk 2 demonstreren we de fundamentele bouwsteen van ons platform, een fononisch kwantumkanaal voor het routen van enkele fononen. De fononische golfgeleider is gekoppeld aan een optomechanische single-mode trillholte, die we gebruiken als bron en detector voor het optomechanisch opwekken en detecteren van enkele fononen. We bestuderen dit platform experimenteel zowel in het klassieke regime als in het kwantumregime en tonen zijn vermogen om enkele fononen op te wekken, te routen en terug te halen. De dispersie van de fononische golfgeleider beperkt echter de prestaties van ons platform.

We verbeteren ons ontwerp van de fononische golfgeleider in hoofdstuk 3 en tonen zijn vermogen om een kwantumtoestand (een time-bin encoded superpositietoestand) in het fononische kanaal te routen. Het routen van kwantumtoestanden zonder verlies van coherentie is een essentiële vereiste voor elk kwantumkanaal. We voeren verder een optomechanische Bell-test uit om de niet-klassieke aard van ons systeem te bevestigen en om het potentieel ervan als multimode optomechanisch kwantumgeheugen te demonstreren. Bovendien zetten we een stap naar meer on-chip coherente controle over fononen door een directionele koppelaar voor enkele fononen te realiseren in hoofdstuk 4. Dit biedt meer mogelijkheden om bewerkingen op enkele fononen op een chip rechtstreeks uit te voeren, zoals het creëren van verstrengeling en superpositie. Ten slotte, in hoofdstuk 5, vatten we de in dit proefschrift besproken resultaten samen en geven we een vooruitblik op hoe deze resultaten kunnen bijdragen aan toekomstige technologieën en ontwikkelingen.

1

INTRODUCTION

"And no one showed us to the land
And no one knows the where's or why's
But something stirs and something tries
And starts to climb toward the light"
- [Pink Floyd - Echoes]

In the past few years, the field of quantum information and computation has come into the spotlight in the community, especially after achieving quantum advantage for quantum computation. Therefore, the need for realizing quantum networks and quantum communication channels has increased significantly. In this manner, heterogeneous quantum networks can be designed to leverage the strengths of different quantum systems for various tasks and applications, such as quantum communication, distributed quantum computing, or quantum memories. Gigahertz (GHz) phonons - quanta of mechanical vibrations - have proven to be promising intermediaries for interconnecting different quantum systems and realizing hybrid quantum networks. Their long coherence time and lifetime are particularly advantageous for quantum memory applications. Due to their slow propagation speed, coherent control of propagating mechanical modes is a relatively straightforward task, if compared to photons. This is beneficial for the realization of quantum delay lines. In this thesis, we develop a platform for the realization of hybrid quantum technologies on a chip. In particular, we develop a platform where different quantum resources can potentially communicate and exchange quantum information via phononic channels in form of travelling phononic wavepackets. At the same time, our platform can also serve as a testbed for fundamental studies in quantum acoustics, aiming at the investigation of the quantum properties of phonons. In this chapter, we first give a general overview of quantum networks and hybrid quantum systems and discuss about how phonons are used in this field of research, the recent developments and potential future studies. We try to answer the question of "what" type of mechanical systems we use and "why" we use them in simple words, and also give a clear idea about where our approach stands in this novel and interesting field of research and technology.

1.1. QUANTUM NETWORKS

Quantum networks represent a paradigm shift in the world of communication, promising to redefine the way we exchange information by leveraging the powerful phenomena of quantum mechanics [1], such as superposition and entanglement that are not available in classical networks. Quantum networks hold the potential to revolutionize secure communication, computation, and thus serving as a fundamental component in the establishment of a quantum internet. Consequently, in the past few decades the field has gained significant interest and attention in from both the scientific and industrial communities. This is driven by advancements in quantum technologies, increasing awareness of quantum's potential applications, and the need for efficient communication systems. The potential mainly stem from ability of a quantum internet to transmit quantum bits (qubits) - fundamentally different from classical bits - between nodes of a quantum network. Moreover, entanglement between nodes in a quantum network leads to large distance correlations and information transfer [1] via techniques such as quantum teleportation [2]. A fundamental configuration of a quantum network is to consider nodes as physical systems which are communicating with each other via quantum channels [3]. The main challenge in realizing such a network is to distribute quantum information across the network, for which coherent quantum channels are needed. A quantum channel, indeed, must be able to preserve quantum coherence over the propagation distance and to mediate interactions between interconnected systems at the quantum mechanical level. For any practical implementation of long-distance quantum networks, quantum repeaters and memories are also crucial components in this scheme in order to entangle (i.e. link) distant nodes. In order to explain the basic working principle, in Fig. 1.1, we present a simple form of a quantum network based on Duan-Lukin-Cirac-Zoller (DLCZ) proposal [4]. In this scheme the quantum network consists of two nodes, at which a quantum memory (or/and a processor) is entangled to a "flying qubit" - a qubit that can travel long distances in a quantum channel - such as photons. By performing an entanglement swapping on the flying qubits at a different station (the dashed box in Fig.1.1), the quantum memories at the nodes that are placed at a long distance become entangled with each other. The entanglement swapping is based on entangling the flying qubits and a following measurement in the Bell axis. This is a simple form of a quantum repeater and entanglement distribution over long distances.

Nowadays in the quantum networks, the quantum memories and repeaters in a node are mainly systems such as atomic ensembles [4–6], color centers and other solid-state systems [7–10]. These systems together with superconducting qubits can also be used as quantum processors for quantum computing applications in each node [11, 12].

From a very general point of view, quantum networks can be classified as homogeneous and heterogeneous. Homogeneous quantum networks consist of components that are of the same type or technology. For example, a network that uses only optical photons within each node and to interconnect different nodes would be considered a homogeneous quantum network. These networks are often designed for specific applications or research purposes where a uniform platform is advantageous. On the contrary, Heterogeneous quantum networks involve the integration of different types of quantum systems or technologies. This could mean combining various qubit technologies, such as superconducting qubits, trapped ions, or solid-state qubits, within the same

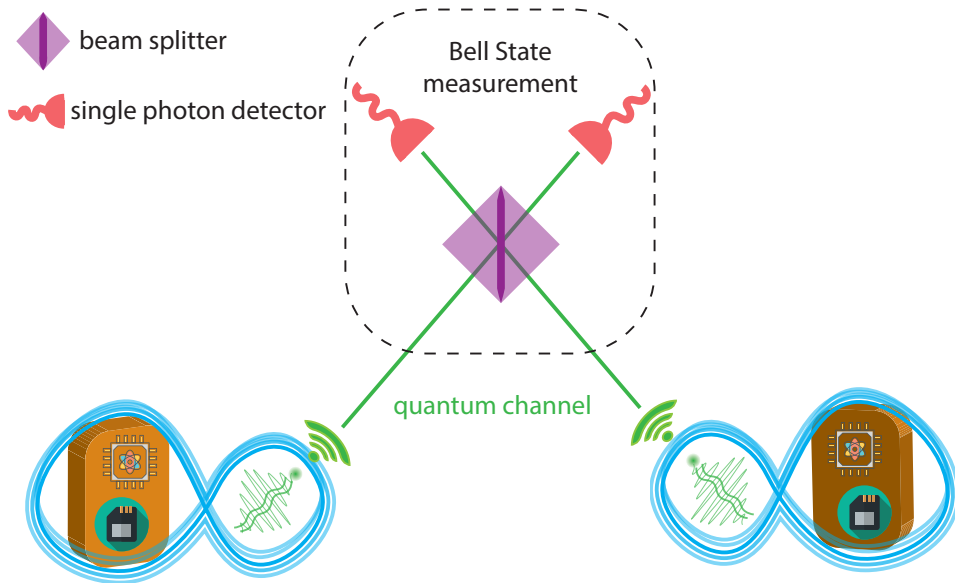


Figure 1.1: A simple schematic of a quantum network based on DLCZ protocol. A quantum memory/processor is entangled to a flying qubit (namely photons) at each node. The flying qubits can travel to long distances via quantum channels to a different station where a Bell-State measurement is performed. After the measurement in the Bell basis, the two distant nodes entangle and the information distributes over long distances.

network and interconnect them using quantum channels such as optical fibers. Heterogeneous quantum networks can be engineered to take advantage of the unique capabilities of various quantum systems, enabling a range of functions and applications, such as quantum communication, distributed quantum computing, and quantum information storage using state-of-the-art systems for each task.

1.2. HYBRID QUANTUM DEVICES

In the past decade, a lot of research has been done on realizing quantum networks and processors using different platforms, as mentioned previously. Each of these platforms has its own advantages and disadvantages over the others, which make it unique for certain types of applications in a quantum network. For instance, superconducting qubits have been shown to be strong candidates for quantum computing and processing, however they usually suffer from short lifetime and coherence time, which make them less suitable as quantum memories and repeaters. On the other hand, color centers, solid state qubits and trapped ions are proven to have up to minutes-long coherence time, which is ideal for memories and repeaters [7, 13]. Another important factor for implementing a quantum network is the ability to transfer quantum information over long distances. Most of the aforementioned platforms are not straightforward for long distance communications - e.g. for the case of NV centers, down conversion of the wavelength to telecom wavelength is needed [14] - while telecom-band photons can be used for this

specific task [15, 16].

Since all these different platforms benefit from different potentials, making them unique for different applications, the need for implementing heterogeneous quantum systems has been increasing significantly over the past years. Combining these platforms together would remarkably enhance the capabilities of a quantum network, by using the state-of-the-art system for each particular task in the network.

Transferring a quantum state between two different systems with high fidelity, is a necessary requirement in realizing a hybrid quantum system. In general terms, the excitation transfer is typically described by an interaction Hamiltonian of a state-swap type of $H_{int} = \hbar g(a^\dagger b + ab^\dagger)$, in which a and b represent the annihilation operators for the coupled systems A and B [17], and g the coupling rate between them. Achieving large interactions for efficient state swap is usually difficult when dealing with different quantum systems. One potential challenge is usually poor matching (e.g. spatial, impedance, etc.) between two systems. For instance, while the spin-spin or the spin-orbit coupling can be relatively large in atomic scales, when a single atom or electron, is placed close to a superconducting circuit, the coupling achieved from the qubit field is orders of magnitude smaller, due to the spatial mismatch of the mm-size qubit circuit and the nm-size atom.

Up to this date, there are many different hybrid platforms developed [17], such as single atoms interacting with light in an optical cavity [18–20], superconducting qubits coupled to a spin ensemble in diamond [21, 22], single spins coupled to microwave photons [23, 24], single electronic spin coupled to mechanical vibrations [25], superconducting qubits coupled to mechanical vibrations [26–31], and optomechanical systems in which mechanical vibrations are coupled to an optical field [32–38]. In Fig. 1.2, we plot the coupling rate in some of the developed hybrid quantum systems, versus the coherence time of the two systems. An important criteria to consider is to have the coupling strength larger than the typical decay rate of a system in order to fully swap its quantum state onto another system ($gT_{2,A,B} \gg 1$).

Each of these hybrid systems have their own unique advantages (and disadvantages). For instance, atomic-molecular-optical (AMO) systems are almost ideal realization of an isolated quantum system and can be controlled at single quantum levels. On the other hand, solid state systems and in general chip-based-technologies promise scalability, benefiting from developments in nanotechnology.

1.2.1. PHONONS AS INTERMEDIARIES

In the past decade, phonons - quanta of mechanical vibrations - have been actively used in hybrid quantum systems and have shown to be great intermediaries for interconnecting various quantum hybrid systems, as they can couple to many different quantum systems, such as telecom photons, superconducting qubits and electronic spins, as shown in Fig. 1.2. Moreover, their long coherence time, specifically in the case of highly confined phonons [34, 37] makes them good candidates for quantum memory usage. In addition to these, the strain and stress field in the material caused by the mechanical vibration, can propagate in the material. As a result, phonons can also travel as sound (mechanical) waves in a material, a property that can be exploited for short distance quantum computation between two nodes on a chip, paving the way towards realizing

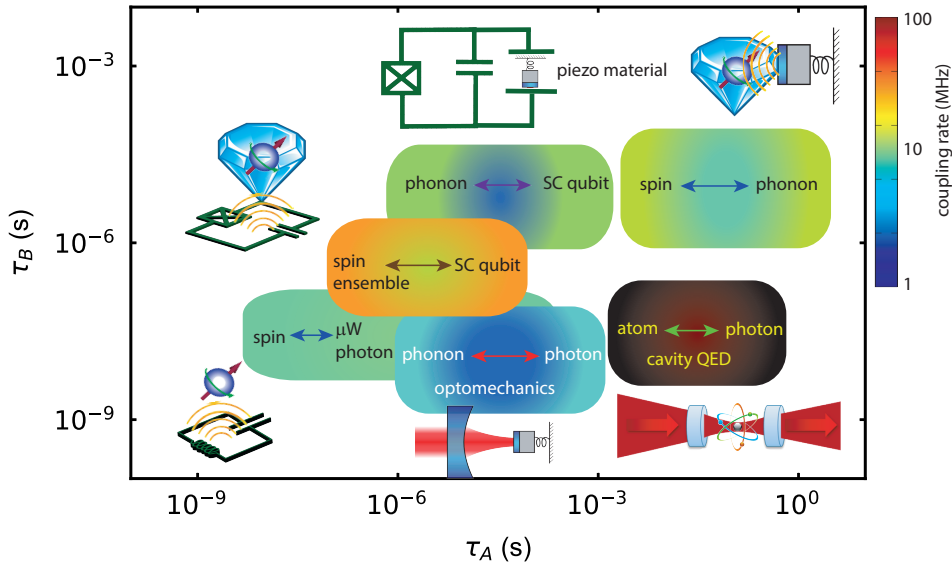


Figure 1.2: The approximate coupling rate in different hybrid quantum systems that can be realistically achieved, versus the decay time of the two systems. $\tau_{A,B}$ represent the typical decay time of system A,B with system A having a longer coherence time.

quantum-lab-on-a-chip architectures. In the early days of classical computers, mechanical delay line memories (now obsolete) were used [39, 40], owing to their slow propagation speed (compared to photons of the same frequency) and long lifetime. A similar idea can be used in quantum networks and computers in order to realize hybrid devices and processors, as well as quantum delay lines for short distance (on-chip) information transfer and quantum multimode memories, using traveling acoustic waves.

1.2.2. PHONONS IN QUANTUM TECHNOLOGY

As mentioned earlier, recently, there has been several studies on the quantum properties of mechanical vibrations, using different platforms such as surface acoustic waves (SAWs), bulk acoustic waves (BAWs) or using confined mechanical modes. A simple sketch is shown in Fig. 1.3 to give an overview over different types of mechanical systems used in quantum technologies. These systems differ from each other in coherence time and lifetime, as well as coupling to the second quantum system (in hybrid architecture). Here we try to introduce some of the abovementioned phononic platform that have been studied so far as hybrid quantum devices, in more details.

BULK ACOUSTIC WAVES (BAWs) [41–43]

These systems consist of mechanical vibrations that propagate inside a bulk medium of a material. These modes are excited, for example, electromechanically, by applying an AC voltage, using metallic electrodes, to a piezoelectric material placed at the surface of the bulk medium 1.3a, that induces bulk vibrations. The electromechanical coupling can

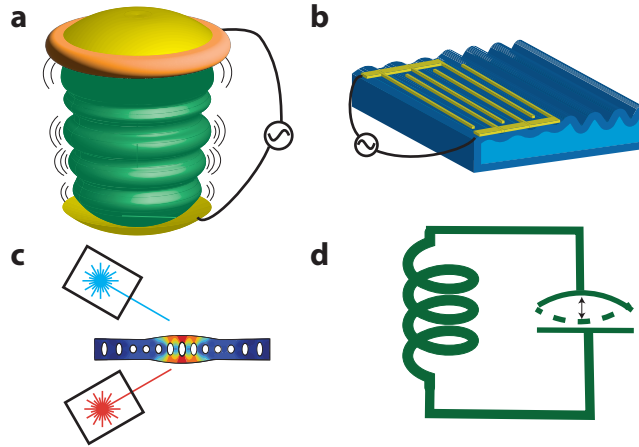


Figure 1.3: Mechanical excitations in different hybrid quantum systems. a) BAWs, that are propagating phononic modes inside a bulk of a piezoelectric material, electromechanically excited by metallic electrodes. b) SAWs, confined on a surface of a piezoelectric material, propagating in a direction transverse to the surface. These waves are usually excited (and detected) electromechanically using IDTs. c) Highly confined phonons coupled to optical photons, in a phononic crystal architecture that is mainly used in optomechanical systems. d) Confined phonons as an oscillating plate of a capacitor in a GHz microwave circuit. Phonons are optomechanically coupled to microwave photons.

be made as large as a few hundred kHz enabling strong coupling between the microwave circuit and the mechanical resonator. The phononic lifetime in these systems is usually limited by the bulk dissipation and phononic scattering inside the bulk medium. These systems lack phononic confinement in lateral direction and, for this reason, they are difficult to scale up and integrate with other systems.

SURFACE ACOUSTIC WAVES (SAWs) [26, 28, 30, 44]

This term corresponds to the mechanical vibrations that is confined on a surface of a material. In most cases, the material is a piezoelectric, and is connected to inter-digital-transducers (IDTs) and microwave-frequency circuits, that is used to excite and measure the acoustic waves. An IDT consists of series of metallic fingers that are deposited directly on the surface of the piezoelectric material. These fingers are spaced by half a wavelength of the mechanical wave and therefore by applying AC voltage on these metallic fingers, with the certain frequency matching the frequency of the acoustic wave, the propagating phonons are excited on the surface of the piezoelectric material. An inverse method is used for detecting the acoustic waves, i.e. when the acoustic wave hits the IDTs, it induces an AC voltage that can be measured. The coupling in these systems is usually electro-mechanical and it can be made as large as a few MHz. Matching the frequency of the microwave circuit (e.g. the superconducting qubit circuit) to that of the phonons, allows full state swap between the microwave photons and phononic excitations in the strong coupling regime ($g \gg \tau_{A,B}^{-1}$). The design of the IDTs are usually quite straightforward and can be engineered to impedance match the microwave circuit to the phononic impedance, and achieve large electromechanical coupling rates. More-

over, the bandwidth of the coupling is controllable by design. However, these systems usually suffer from short phononic lifetime (in the order of $1\text{-}2\ \mu\text{s}$) due to the lack of lateral confinement of the phononic field combined with the mechanical dissipation in the piezoelectric material. Besides, because of the lateral extension of the phononic wave, these systems are not scalable and are not suitable for integrated architectures.

HIGHLY CONFINED PHONONS IN ELECTROMECHANICAL SYSTEMS [31, 45, 46]

In addition to the aforementioned electromechanical systems, recently there has been some research, using highly confined GHz phonons, electromechanically coupled to superconducting qubits or microwave circuits, mediated via piezoelectric effects. These systems have a phononic crystal design that allows bandgap engineering of phononic structures and confining GHz phonons to a small mode volume. A strong coupling rate of about $\sim 10\text{MHz}$ can be achieved in these systems.

HIGHLY CONFINED PHONONS IN NANOMECHANICAL RESONATORS

There are many recent studies on highly confined phonons (in the form of mechanical nanoresonators). These systems utilize physics of optomechanics (phonons coupled to photons), and are used in two different frequency regime by using either microwave photons or optical/telecom photons.

Optomechanical systems using optical photons: The mechanical frequency in these systems vary between tens of kHz to MHz range using silicon-nitride membranes or strings as the mechanical resonator [47–49], to a few GHz, using photonic/phononic crystal structures [31, 35, 37]. In the case of low-frequency mechanics, active cooling methods (such as feedback cooling or laser cooling) is needed in order to reach the mechanical ground state. On the contrary, GHz phonons can be passively cooled down to the ground state in a dilution refrigerator at milli-Kelvin temperatures. Photo-elastic effect is often the dominant effect for phonon-photon coupling in these systems.

Optomechanical systems using microwave photons: [50–53] In these systems the mechanical frequency is usually in the order of $\sim 10\text{MHz}$ and it is by a moving plate of a capacitor in a GHz microwave LC circuit. Because of the low frequency of the mechanical mode, active cooldowns are needed, which is usually done by the sideband-cooling using the microwave circuit. The optomechanical coupling rate in the order of hundreds of hertz can be achieved with these architectures.

In this thesis, we design hybrid quantum devices for quantum acoustics applications as well as other potential quantum protocols, using confined phonons and telecom light, in a cavity optomechanics architecture. This configuration is particularly interesting for integrated chip designs and is straightforward to scale up. In the following part of this chapter, we provide an overview about integrated systems, advancements in nanotechnology and its importance in nowadays technologies.

1.3. INTEGRATED SYSTEMS

As a start, let's try to find an answer to the question of "why integrated circuits are important?" As individual technologies continue to evolve, integrating them into unified and scalable systems enables the development of innovative products, services, and solutions. Importantly, the capacity to miniaturize components has played a pivotal role in

the development of innovative technologies. This capacity allows for the fabrication of integrated circuits containing thousands of elements, all within a compact millimeter-scale footprint [54–56]. In more details, reducing the footprint of a device has numerous advantages such as:

- **Space Efficiency:** Smaller devices occupy less physical space, which can be crucial in environments where space is limited or expensive. It allows for more efficient use of available space.
- **Cost Reduction:** Smaller devices typically require fewer materials and components, which can lead to lower manufacturing and maintenance costs. However, they usually require higher level technologies and manufacturing machines that can be significantly more expensive. Although this is a perpetual trade-off for any technological improvement.
- **Environmental Impact:** Having a smaller environmental footprint, leads to reduced material usage and lower energy consumption during manufacturing and operation contribute to a decrease in the device's overall environmental impact. This is particularly relevant in terms of sustainability and reducing electronic waste.
- **Scalability:** Scalability is one of the most important aspects of integrated technologies, that makes them useful for nowadays usage. A scalable system can accommodate a growing number of information and devices without a significant degradation in performance or/and taking too much space. This ensures a sensible resource consumption even as usage expands. This has become an important factor in developing any kind of technologies in the modern world.

Therefore, making integrated and scalable hybrid quantum devices is of great importance in order to properly substitute the nowadays classical technologies, and handle the large amount of users, data and information. In the past century, integrated Complementary Metal-Oxide-Semiconductor (CMOS) electronic circuits have been revolutionary for many technologies. In Fig. 1.4, the typical feature size of integrated circuits on a chip is plotted over years. It's important to note that this size reduction, or scaling, has been a cornerstone of Moore's Law, which posits that the number of transistors on a microchip doubles approximately every two years. Similarly there has been numerous amount of research for miniaturizing photonic components, enabling photonic circuits with thousands of components on a mm-scale chip. Therefore, in analogy to photonics, achieving integrated phononic circuitry is a prerequisite for the usage of phonon in quantum networks in future technologies.

1.3.1. INTEGRATED PHONONIC TECHNOLOGY

Having integrated phononic circuits, would help developing a scalable hybrid quantum system, that would satisfy the demand caused by large number of users (and nodes) in a quantum network. This would pave the way towards commercializing hybrid quantum networks using phonons as intermediaries in the future. High contrast refractive index medium are necessary for realizing integrated photonic circuits. Similarly, high contrast acoustic index is needed in order to implement integrated phononic circuitry. Recently,

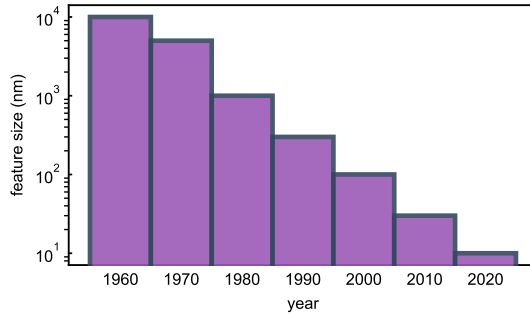


Figure 1.4: The approximate feature size in integrated circuit fabrication over the years [57]

there has been multiple studies in different research groups in order to realize such a concept for phononic waves. Some of these research include using high-index phononic materials such as gallium-nitride (GaN) on a low-index substrate such as sapphire, to study spin-orbit coupling of phonons and different phononic polarizations [58, 59], 2D suspended structures and phononic edge modes [60, 61], as well as nanowires with controllable electronic and phononic properties [62].

In this thesis, we focus on quasi 1D structures of suspended silicon as a platform to route and coherently manipulate phononic excitations [63, 64], and use a similar design of optomechanical cavity for source and detectors of single phonons. Such a system is particularly interesting since can be used not only in optomechanics, but in principle can be integrated with other types of single phonon sources [46].

1.4. QUICK SUMMARY OF CHAPTERS

This thesis is devoted to design, fabrication and characterization of devices which serve as building blocks for both quantum acoustic experiments and generally quantum hybrid systems. In particular, the focus of the work here presented is to develop quantum channels for highly confined phonons in 1D structures. We want to build a platform for having more coherent control over traveling phonons on a chip, which essentially provides more degree of freedom to manipulate different quantum systems on a chip. This platform can be used later on for interconnecting different heterogeneous quantum systems in a quantum network, as well as for performing fundamental studies on single quantum of mechanical vibrations.

In order to achieve this, we design a quasi-1D phononic waveguide, using phononic bandgap engineering, which can be used to route single phonons between different quantum systems on a chip that communicate via traveling phonons. Furthermore, we investigate the capability of this structure for routing quantum states, using a traveling entangled phononic state. As a next step, we demonstrate a phononic beam splitter, which provides more opportunities for distributing and manipulating quantum information on a chip using traveling phonons. The designs provided in this thesis are building blocks for implementing more advanced hybrid quantum systems on a chip. We use

optomechanical techniques to excite and detects single phonons, however our designs can potentially be integrated with other types of single phonon sources and detectors such as superconducting qubits.

In the following, we briefly summarise the work that is carried out in each chapter of this thesis and how it paves the way towards our goal.

- **Chapter 2:** In this chapter we design a phononic waveguide, based on phononic crystal design. With this device we route highly confined phonons in quasi 1D structures and introduce basic characterization techniques and parameters in order to investigate the performance of the device in the quantum regime. Furthermore, we investigate the routing of single phonons and show that it can be, in principle, used to time-multiplex information at single quantum level.
- **Chapter 3:** In this chapter we first show an improved version of our phononic waveguides, and we use a different fabrication recipe that further improves the quantum performance. The advanced design of the device, allows us to route quantum information - i.e. time-bin entangled phonons - on our chip. In order to do that, we introduce and investigate the basis of a work frame for creating, routing and detecting time-bin entangled phonons. Moreover, we perform an optomechanical Bell-test using our time-bin entangled phonons as one qubit and optical photons as the flying qubit. This will complete the most basic tool for routing quantum information on chip and realize hybrid quantum networks.
- **Chapter 4:** Here we move one step closer towards a platform for full coherent control over single phonons on a chip. After realizing a phononic waveguide, the next tool in order to perform more complicated quantum acoustics experiments on chip is a phononic directional coupler. We design and fabricate an integrated phononic directional coupler and show its performance for different splitting ratios in the classical regime. We further use a device with 50:50 splitting ratio, as a 50:50 beam splitter and investigate the performance of the device in quantum regime. The design is based on two adjacent phononic waveguides, mechanically coupled to each other.

REFERENCES

- [1] S. Wehner, D. Elkouss, and R. Hanson, Quantum internet: A vision for the road ahead, *Science* **362**, eaam9288 (2018).
- [2] C. H. Bennett, G. Brassard, C. Crépeau, R. Jozsa, A. Peres, and W. K. Wootters, Teleporting an unknown quantum state via dual classical and Einstein-Podolsky-Rosen channels, *Phys. Rev. Lett.* **70**, 1895 (1993).
- [3] H. J. Kimble, The quantum internet, *Nature* **453**, 1023 (2008).
- [4] L. M. Duan, M. D. Lukin, J. I. Cirac, and P. Zoller, Long-distance quantum communication with atomic ensembles and linear optics., *Nature* **414**, 413 (2001).
- [5] J. Rui, Y. Jiang, S.-J. Yang, B. Zhao, X.-H. Bao, and J.-W. Pan, Operating spin echo in the quantum regime for an atomic-ensemble quantum memory, *Physical Review Letters* **115**, 133002 (2015).
- [6] A. I. Lvovsky, B. C. Sanders, and W. Tittel, Optical quantum memory, *Nature photonics* **3**, 706 (2009).
- [7] C. E. Bradley, J. Randall, M. H. Aboeib, R. C. Berrevoets, M. J. Degen, M. A. Bakker, M. Markham, D. J. Twitchen, and T. H. Taminiau, A ten-qubit solid-state spin register with quantum memory up to one minute, *Phys. Rev. X* **9**, 031045 (2019).
- [8] M. H. Aboeib, J. Cramer, M. A. Bakker, N. Kalb, M. Markham, D. J. Twitchen, and T. H. Taminiau, One-second coherence for a single electron spin coupled to a multi-qubit nuclear-spin environment, *Nature Communications* **2018** 9:1 **9**, 1 (2018), [arXiv:1801.01196](https://arxiv.org/abs/1801.01196).
- [9] T. Zhong, J. M. Kindem, J. G. Bartholomew, J. Rochman, I. Craiciu, E. Miyazono, M. Bettinelli, E. Cavalli, V. Verma, S. W. Nam, *et al.*, Nanophotonic rare-earth quantum memory with optically controlled retrieval, *Science* **357**, 1392 (2017).
- [10] M. P. Hedges, J. J. Longdell, Y. Li, and M. J. Sellars, Efficient quantum memory for light, *Nature* **465**, 1052 (2010).
- [11] S. Saito, X. Zhu, R. Amsüss, Y. Matsuzaki, K. Kakuyanagi, T. Shimo-Oka, N. Mizuochi, K. Nemoto, W. J. Munro, and K. Semba, Towards realizing a quantum memory for a superconducting qubit: Storage and retrieval of quantum states, *Physical review letters* **111**, 107008 (2013).
- [12] H.-L. Huang, D. Wu, D. Fan, and X. Zhu, Superconducting quantum computing: a review, *Science China Information Sciences* **63**, 1 (2020).
- [13] Y. Wang, M. Um, J. Zhang, S. An, M. Lyu, J.-N. Zhang, L.-M. Duan, D. Yum, and K. Kim, Single-qubit quantum memory exceeding ten-minute coherence time, *Nature Photon.* **11**, 646 (2017).

- [14] A. Dréau, A. Tchebotareva, A. E. Mahdaoui, C. Bonato, and R. Hanson, Quantum frequency conversion of single photons from a nitrogen-vacancy center in diamond to telecommunication wavelengths, *Phys. Rev. Appl.* **9**, 064031 (2018).
- [15] B. Hensen, H. Bernien, A. E. Dréau, A. Reiserer, N. Kalb, M. S. Blok, J. Ruitenberg, R. F. L. Vermeulen, R. N. Schouten, C. Abellán, W. Amaya, V. Pruneri, M. W. Mitchell, M. Markham, D. J. Twitchen, D. Elkouss, S. Wehner, T. H. Taminiau, and R. Hanson, Loophole-free Bell inequality violation using electron spins separated by 1.3 kilometres, *Nature* **526**, 682 (2015).
- [16] M. Aspelmeyer, T. Jennewein, M. Pfennigbauer, W. Leeb, and A. Zeilinger, Long-distance quantum communication with entangled photons using satellites, *IEEE Journal of Selected Topics in Quantum Electronics* **9**, 1541 (2003).
- [17] G. Kurizki, P. Bertet, Y. Kubo, K. Mølmer, D. Petrosyan, P. Rabl, and J. Schmiedmayer, Quantum technologies with hybrid systems, *Proceedings of the National Academy of Sciences* **112**, 3866 (2015).
- [18] J. D. Thompson, T. G. Tiecke, N. P. de Leon, J. Feist, A. V. Akimov, M. Gullans, A. S. Zibrov, V. Vuletić, and M. D. Lukin, Coupling a single trapped atom to a nanoscale optical cavity, *Science* **340**, 1202 (2013).
- [19] Y. Colombe, T. Steinmetz, G. Dubois, F. Linke, D. Hunger, and J. Reichel, Strong atom–field coupling for bose–einstein condensates in an optical cavity on a chip, *Nature* **450**, 272 (2007).
- [20] A. Reiserer and G. Rempe, Cavity-based quantum networks with single atoms and optical photons, *Rev. Mod. Phys.* **87**, 1379 (2015).
- [21] X. Zhu, S. Saito, A. Kemp, K. Kakuyanagi, S.-i. Karimoto, H. Nakano, W. J. Munro, Y. Tokura, M. S. Everitt, K. Nemoto, *et al.*, Coherent coupling of a superconducting flux qubit to an electron spin ensemble in diamond, *Nature* **478**, 221 (2011).
- [22] S. Saito, X. Zhu, R. Amsüss, Y. Matsuzaki, K. Kakuyanagi, T. Shimo-Oka, N. Mizuochi, K. Nemoto, W. J. Munro, and K. Semba, Towards realizing a quantum memory for a superconducting qubit: Storage and retrieval of quantum states, *Phys. Rev. Lett.* **111**, 107008 (2013).
- [23] N. Samkharadze, G. Zheng, N. Kalhor, D. Brousse, A. Sammak, U. C. Mendes, A. Blais, G. Scappucci, and L. M. K. Vandersypen, Strong spin-photon coupling in silicon, *Science* **359**, 1123 (2018), <https://www.science.org/doi/pdf/10.1126/science.aar4054>.
- [24] X. Mi, M. Benito, S. Putz, D. M. Zajac, J. M. Taylor, G. Burkard, and J. R. Petta, A coherent spin–photon interface in silicon, *Nature* **555**, 599 (2018).
- [25] S. Maity, L. Shao, S. Bogdanović, S. Meesala, Y.-I. Sohn, N. Sinclair, B. Pingault, M. Chalupnik, C. Chia, L. Zheng, *et al.*, Coherent acoustic control of a single silicon vacancy spin in diamond, *Nature communications* **11**, 193 (2020).

- [26] K. J. Satzinger, Y. P. Zhong, H.-S. Chang, G. A. Peairs, A. Bienfait, M.-H. Chou, A. Y. Cleland, C. R. Conner, E. Dumur, J. Grebel, I. Gutierrez, B. H. November, R. G. Povey, S. J. Whiteley, D. D. Awschalom, D. I. Schuster, and A. N. Cleland, Quantum control of surface acoustic-wave phonons, *Nature* **563**, 661 (2018).
- [27] É. Dumur, K. J. Satzinger, G. A. Peairs, M.-H. Chou, A. Bienfait, H.-S. Chang, C. R. Conner, J. Grebel, R. G. Povey, Y. P. Zhong, and A. N. Cleland, Quantum communication with itinerant surface acoustic wave phonons, *npj Quantum Inf.* **7**, 173 (2021).
- [28] A. Bienfait, K. J. Satzinger, Y. P. Zhong, H.-S. Chang, M.-H. Chou, C. R. Conner, E. Dumur, J. Grebel, G. A. Peairs, R. G. Povey, and A. N. Cleland, Phonon-mediated quantum state transfer and remote qubit entanglement, *Science* **364**, 368 (2019).
- [29] A. Bienfait, Y. P. Zhong, H. S. Chang, M. H. Chou, C. R. Conner, Dumur, J. Grebel, G. A. Peairs, R. G. Povey, K. J. Satzinger, and A. N. Cleland, Quantum Erasure Using Entangled Surface Acoustic Phonons, *Phys. Rev. X* **10**, 21055 (2020).
- [30] M. V. Gustafsson, T. Aref, A. F. Kockum, M. K. Ekström, G. Johansson, and P. Delsing, Propagating phonons coupled to an artificial atom, *Science* **346**, 207 (2014).
- [31] E. A. Wollack, A. Y. Cleland, R. G. Gruenke, Z. Wang, P. Arrangoiz-Arriola, and A. H. Safavi-Naeini, Quantum state preparation and tomography of entangled mechanical resonators, *Nature* **604**, 463 (2022).
- [32] M. Aspelmeyer, T. J. Kippenberg, and F. Marquardt, Cavity optomechanics, *Rev. Mod. Phys.* **86**, 1391 (2014).
- [33] J. Chan, T. P. M. Alegre, A. H. Safavi-Naeini, J. T. Hill, A. Krause, S. Gröblacher, M. Aspelmeyer, and O. Painter, Laser cooling of a nanomechanical oscillator into its quantum ground state, *Nature* **478**, 89 (2011).
- [34] J. Chan, A. H. Safavi-Naeini, J. T. Hill, S. Meenehan, and O. Painter, Optimized optomechanical crystal cavity with acoustic radiation shield, *App. Phys. Lett.* **101**, 081115 (2012).
- [35] I. Marinković, A. Wallucks, R. Riedinger, S. Hong, M. Aspelmeyer, and S. Gröblacher, An optomechanical Bell test, *Phys. Rev. Lett.* **121**, 220404 (2018).
- [36] R. Riedinger, S. Hong, R. A. Norte, J. A. Slater, J. Shang, A. G. Krause, V. Anant, M. Aspelmeyer, and S. Gröblacher, Non-classical correlations between single photons and phonons from a mechanical oscillator, *Nature* **530**, 313 (2016).
- [37] A. Wallucks, I. Marinković, B. Hensen, R. Stockill, and S. Gröblacher, A quantum memory at telecom wavelengths, *Nat. Phys.* **16**, 772 (2020).
- [38] R. Riedinger, A. Wallucks, I. Marinković, C. Löschnauer, M. Aspelmeyer, S. Hong, and S. Gröblacher, Remote quantum entanglement between two micromechanical oscillators, *Nature* **556**, 473 (2018).
- [39] M. V. Wilkes, Computers then and now, *J. ACM* **15**, 1–7 (1968).

- [40] I. Auerbach, J. Eckert, R. Shaw, and C. Sheppard, Mercury delay line memory using a pulse rate of several megacycles, *Proceedings of the IRE* **37**, 855 (1949).
- [41] Y. Chu, P. Kharel, W. H. Renninger, L. D. Burkhardt, L. Frunzio, P. T. Rakich, and R. J. Schoelkopf, Quantum acoustics with superconducting qubits, *Science* **358**, 199 (2017).
- [42] Y. Chu, P. Kharel, T. Yoon, L. Frunzio, P. T. Rakich, and R. J. Schoelkopf, Creation and control of multi-phonon fock states in a bulk acoustic-wave resonator, *Nature* **563**, 666 (2018).
- [43] P. Kharel, Y. Chu, M. Power, W. H. Renninger, R. J. Schoelkopf, and P. T. Rakich, Ultra-high-q phononic resonators on-chip at cryogenic temperatures, *APL Photonics* **3**, 066101 (2018).
- [44] M. K. Ekström, T. Aref, J. Runeson, J. Björck, I. Boström, and P. Delsing, Surface acoustic wave unidirectional transducers for quantum applications, *Appl. Phys. Lett.* **110**, 073105 (2017).
- [45] P. Arrangoiz-Arriola, E. A. Wollack, Z. Wang, M. Pechal, W. Jiang, T. P. McKenna, J. D. Witmer, R. V. Laer, and A. H. Safavi-Naeini, Resolving the energy levels of a nanomechanical oscillator, *Nature* **571**, 537 (2019).
- [46] M. Mirhosseini, A. Sipahigil, M. Kalaei, and O. Painter, Superconducting qubit to optical photon transduction, *Nature* **588**, 599 (2020).
- [47] M. Rossi, D. Mason, J. Chen, Y. Tsaturyan, and A. Schliesser, Measurement-based quantum control of mechanical motion, *Nature* **563**, 53 (2018).
- [48] S. A. Saarinen, N. Kralj, E. C. Langman, Y. Tsaturyan, and A. Schliesser, Laser cooling a membrane-in-the-middle system close to the quantum ground state from room temperature, *Optica* **10**, 364 (2023).
- [49] V. Sudhir, D. J. Wilson, R. Schilling, H. Schütz, S. A. Fedorov, A. H. Ghadimi, A. Nunnenkamp, and T. J. Kippenberg, Appearance and disappearance of quantum correlations in measurement-based feedback control of a mechanical oscillator, *Phys. Rev. X* **7**, 011001 (2017).
- [50] T. Palomaki, J. Teufel, R. Simmonds, and K. Lehnert, Entangling mechanical motion with microwave fields, *Science* **342**, 710 (2013).
- [51] A. P. Reed, K. H. Mayer, J. D. Teufel, L. D. Burkhardt, W. Pfaff, M. Reagor, L. Sletten, X. Ma, R. J. Schoelkopf, E. Knill, and K. W. Lehnert, Faithful conversion of propagating quantum information to mechanical motion, *Nature Phys.* **13**, 1163 (2017).
- [52] J. Teufel, T. Donner, M. Castellanos-Beltran, J. Harlow, and K. Lehnert, Nanomechanical motion measured with an imprecision below that at the standard quantum limit, *Nature nanotechnology* **4**, 820 (2009).

- [53] M. Yuan, M. A. Cohen, and G. Steele, Silicon nitride membrane resonators at millikelvin temperatures with quality factors exceeding 10^8 , *Appl. Phys. Lett.* **107**, 263501 (2015).
- [54] Y. Wang, J. A. Holguín-Lerma, M. Vezzoli, Y. Guo, and H. X. Tang, Photonic-circuit-integrated titanium: sapphire laser, *Nat. Photonics* **17**, 338 (2023).
- [55] X. Liu, A. W. Bruch, and H. X. Tang, Aluminum nitride photonic integrated circuits: from piezo-optomechanics to nonlinear optics, *Adv. Opt. Photonics* **15**, 236 (2023).
- [56] J. Wang, F. Sciarrino, A. Laing, and M. G. Thompson, Integrated photonic quantum technologies, *Nat. Photonics* **14**, 273 (2020).
- [57] N. Alam and M. Alam, The trend of different parameters for designing integrated circuits from 1973 to 2019 and linked to moore's law, *Aust. J. Eng. Innov. Technol* **2**, 16 (2020).
- [58] W. Fu, Z. Shen, Y. Xu, C.-L. Zou, R. Cheng, X. Han, and H. X. Tang, Phononic integrated circuitry and spin-orbit interaction of phonons, *Nature communications* **10**, 2743 (2019).
- [59] Z. Shen, W. Fu, R. Cheng, H. Townley, C.-L. Zou, and H. X. Tang, Polarization mode hybridization and conversion in phononic wire waveguides, *Applied Physics Letters* **115**, 10.1063/1.5120844 (2019).
- [60] G. Madiot, R. C. Ng, G. Arregui, O. Florez, M. Albrechtsen, S. Stobbe, P. D. García, and C. M. Sotomayor-Torres, Optomechanical generation of coherent ghz vibrations in a phononic waveguide, *Phys. Rev. Lett.* **130**, 106903 (2023).
- [61] G. Madiot, M. Albrechtsen, C. M. Sotomayor-Torres, S. Stobbe, and G. Arregui, Multimode optomechanics with a two-dimensional optomechanical crystal, *APL Photonics* **8**, 10.1063/5.0170883 (2023).
- [62] A. K. Sivan, B. Abad, T. Albrigi, O. Arif, J. Trautvetter, A. Ruiz Caridad, C. Arya, V. Zannier, L. Sorba, R. Rurali, *et al.*, Gaas/gap superlattice nanowires for tailoring phononic properties at the nanoscale: Implications for thermal engineering, *ACS Applied Nano Materials* 10.1021/acsnm.3c04245 (2023).
- [63] A. Zivari, R. Stockill, N. Fiaschi, and S. Gröblacher, Non-classical mechanical states guided in a phononic waveguide, *Nature Phys.* **18**, 789 (2022).
- [64] A. Zivari, N. Fiaschi, R. Burgwal, E. Verhagen, R. Stockill, and S. Gröblacher, On-chip distribution of quantum information using traveling phonons, *Science Advances* **8**, eadd2811 (2022).

2

NON-CLASSICAL MECHANICAL STATES GUIDED IN A PHONONIC WAVEGUIDE

"Life's biggest battles often are fought alone"

[Dream Theater - Breaking all illusions]

**Amirparsa ZIVARI, Robert STOCKILL, Niccolò FIASCHI,
Simon GRÖBLACHER**

The ability to create, manipulate and detect non-classical states of light has been key for many recent achievements in quantum physics and for developing quantum technologies. Achieving the same level of control over phonons, the quanta of vibrations, could have a similar impact, in particular on the fields of quantum sensing and quantum information processing. Here we present a crucial step towards this level of control and realize a single-mode waveguide for individual phonons in a suspended silicon micro-structure. We use a cavity-waveguide architecture, where the cavity is used as a source and detector for the mechanical excitations, while the waveguide has a free standing end in order to reflect the phonons. This enables us to observe multiple round-trips of the phonons between the source and the reflector. The long mechanical lifetime of almost 100 μs demonstrates the possibility of nearly lossless transmission of single phonons over, in principle,

This work is published in Nature Physics: Amirparsa Zivari, Robert Stockill, Niccolò Fiaschi and Simon Gröblacher, *Non-classical mechanical states guided in a phononic waveguide*, Nat. Phys. 18, 789–793 (2022).

tens of centimeters. Our experiment demonstrates full on-chip control over traveling single phonons strongly confined in the directions transverse to the propagation axis, potentially enabling a time-encoded multimode quantum memory at telecom wavelength and advanced quantum acoustics experiments.

2.1. INTRODUCTION

CREATING and detecting quantum states of mechanical motion open up new possibilities for quantum information processing, quantum sensing and probing the foundations of quantum physics [1]. In particular within the field of quantum optomechanics many remarkable milestones have been reached over the past years: from showing the ability to realize the quantum ground state of a mechanical oscillator and single phonon control [2], unambiguous demonstration of the quantum nature of phonons through the creation of entangled states [3–5] and a Bell test [6], to realizing a long coherence-time quantum memory [7]. Furthermore, the field has shown the potential to enable crucial applications in connecting quantum computers, and transfer information between them [8–11]. While these applications usually rely on highly confined phononic states (with a typical mode volume on the order of the wavelength), the use of traveling phonons promises the ability to create on-chip architectures for classical and quantum information [12], with the potential to add completely new capabilities compared to their optical counterparts. The exciting prospects in this new field of quantum acoustics are enabled by the orders of magnitude slower propagation speed compared to photons, the inherently low loss, their extremely low energy and the small mode volume compared to GHz-frequency photons. These features make phonons ideally suited for direct manipulation on a chip with wavelength sized components, while the ability to realize significant time-delays in a short distance makes this type of system an ideal platform for on-chip operations [13]. Furthermore, phonons have also demonstrated their unique capability to efficiently couple and even mediate the interaction between various quantum systems [14], such as superconducting qubits [15], defect centers in solids [16], and quantum dots [17, 18]. Using mechanical excitations as low-loss carriers of quantum information will allow for the construction of two-dimensional architectures and large-scale phononic quantum networks [19].

While the creation of non-classical mechanical states have been demonstrated in multiple physical systems [20], only a very limited number of experiments have been able to realize propagating modes in the quantum regime, all based on surface acoustic waves [15, 21, 22]. This approach comes with its own limitations and challenges, such as relatively short lifetimes, losses due to beam steering and diffraction, typically only bi-directional emission and no full confinement of the mode except in resonators. In the classical domain on the other hand, several proof-of-concept experiments have realized the creation, transport and detection of mechanical states at cryogenic temperatures [23] over millimeter ranges, as well as at room temperature and atmospheric pressure [24]. The possibility of guiding a mechanical quantum state in a waveguide that confines the excitation in all directions transverse to its propagation, similar to optical fibers and waveguides, remains an open challenge.

2.2. METHODS

Here we demonstrate a single-mode phononic waveguide directly coupled to an on-chip source and detector for non-classical mechanical states. We verify the non-classicality of the launched mechanical states by measuring their quantum correlations with an optical read-out field. In particular, we use the optomechanical interaction to herald the

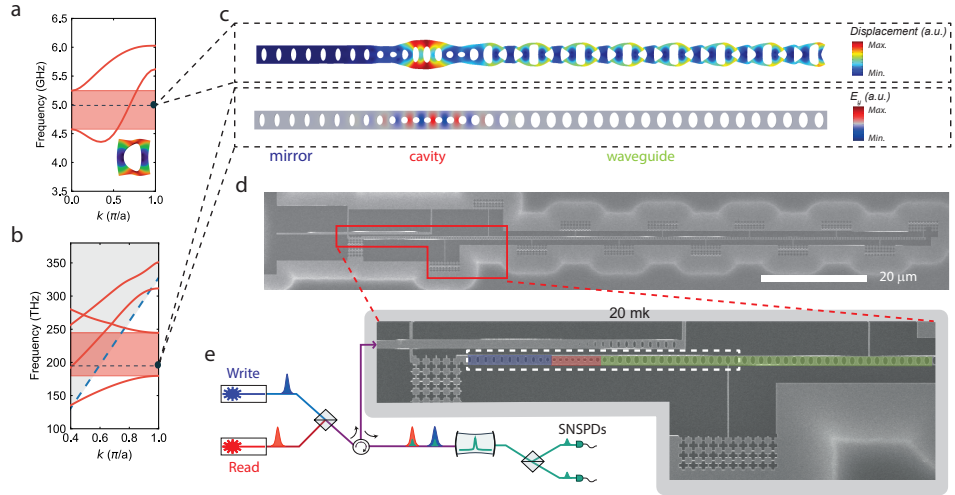


Figure 2.1: Device and experimental setup. a) Band diagram for the modes with symmetric displacement field with respect to the propagation direction along the waveguide. These modes are expected to couple efficiently to the resonant optomechanical cavity mode. The highlighted region (red) shows a single mode waveguide for the symmetric breathing mode with linear dispersion. The dashed line represent the frequency of the modes of the optomechanical structure. Inset: mode shape of the unit cell from this simulation for the band of interested. b) Band diagram for the optical TE mode of the phononic waveguide, exhibiting a band gap at telecom wavelengths, allowing for a confined optical mode inside the optomechanical resonator. The dashed blue line is the light cone, with the non guided modes in the gray shaded area. c) Mechanical (top) and optical (bottom) eigenfrequency simulation of the full cavity and waveguide structure. Clearly visible are the resonant breathing mode of the optomechanical crystal (left) and the waveguide mode (right). As the mechanical mode leaks through the waveguide, the optical mode stays confined inside the optomechanical resonator. d) A scanning electron microscope image of the device used in the experiment, showing the full device with mirror, cavity and the $92 \mu\text{m}$ long waveguide, as well as the optical coupling waveguide (top left). e) Schematic of the setup together with a zoomed-in section of (d) (indicated by the red box). The blue, red and green shaded regions show mirror, cavity and waveguide, respectively. The white dashed rectangle is the area of the simulation in (c). See the text and SI 2.5 for a more details.

creation of a single phonon, which then leaks into the phononic waveguide. Since the waveguide has a free standing end that acts as a mirror for the phonons, the excitations bounce, i.e. reflect, back and forth with a certain characteristic time that is determined by the group velocity and the length of the waveguide. Moreover, we observe non-classical correlations between time-bin encoded phonons [25], by creating and detecting a phonon in either an early or late time window. The long mechanical lifetime of the device will also allow the creation of an on-chip network for quantum acoustic experiments. With the on-chip source, detector and waveguide presented in this work, only a phononic beam splitter and phase modulator need to be developed in order to obtain full coherent control over phonons on a chip.

We design our phononic crystal waveguide in thin-film silicon, which is single-mode for the symmetric breathing mode of the structure, in the frequency range of interest (at around 5 GHz with a single mode range of 750 MHz) and has an approximately linear dispersion, in order to maintain the spatial mode shape of the traveling phonons. This

waveguide is connected to an optomechanical resonator acting as the single-phonon source and detector. For the waveguide design, only the symmetric breathing mode is considered, in order to enable a good mode overlap with the mode of the optomechanical cavity, as these resonant modes have large optomechanical coupling, and can easily be created and detected optically. At the same time, in order to realize a high-finesse optical cavity, we design our phononic waveguide to act as a mirror for photons, therefore confining the optical field in the optomechanical resonator.

The details of our design are shown in Fig. 2.1a and 2.1b, where we plot the band structure with the right mechanical symmetry, as well as the transverse electric (TE) polarized optical mode. An eigenvalue simulation of the full structure, cavity and waveguide, is shown in Fig. 2.1c. The mechanical mode extends into the waveguide, while the optical mode is strongly confined to the cavity region with a similar mode volume to previous works [4, 26–28]. The different sizes of the holes in the structure create the mirror, defect and waveguide. The hole dimensions and periodicity in the waveguide part are adjusted to tune the group velocity. We design the waveguide to have a small group velocity while still having a linear band inside the frequency range of interest (see SI for more details). From the simulated group velocity, the time duration of the mechanical packet (set by the optical pulse length of 40 ns), and the time of the mechanical excitation to leak from the cavity to the waveguide, we determine a minimum length of about $40\ \mu\text{m}$ for the waveguide for the excitation to completely leave the cavity before it comes back again, which is why we choose a length of $92\ \mu\text{m}$. In order to support the long waveguide after suspension, we use narrow (50 nm wide) tethers to connect it to the surrounding silicon. Moreover, to prevent any mechanical dissipation through the tethers, they are directly connected to a phononic shield, as can be seen in the zoomed-in image of the device in Fig. 2.1e. The phononic shield features a bandgap from 4 GHz to 6 GHz, and by increasing the number of periods in the shields we can increase the mechanical lifetime (see SI). The same phononic shields are used at the left end of the device, to further increase the mechanical lifetime.

A picture of the device and sketch of the experimental setup can be found in Figure 2.1d-e. To excite and detect non-classical phonons we use laser pulses detuned from the optical resonance to address the optomechanical Stokes and anti-Stokes sidebands in order to create (write) the mechanical excitation and to map it onto the optical mode (read), respectively [29]. After being combined on a 50:50 beam splitter (BS), the light is routed via an optical circulator to the device. The reflected light from the device is then filtered using free space Fabry-Pérot cavities to block the pump laser pulses and, after another BS, is sent to the superconducting nanowire single photon detectors (SNSPDs). The device itself is cooled to 20 mK in order to initialize the mechanical mode of interest deep in the ground state.

2.3. RESULTS

2.3.1. BASIC AND CLASSICAL CHARACTERIZATIONS

For the initial characterization of the device, we use a tunable continuous-wave (CW) laser to determine the optical resonance in reflection. As shown in Fig. 2.2a, the fundamental optical resonance has a central wavelength around 1541 nm and a linewidth of

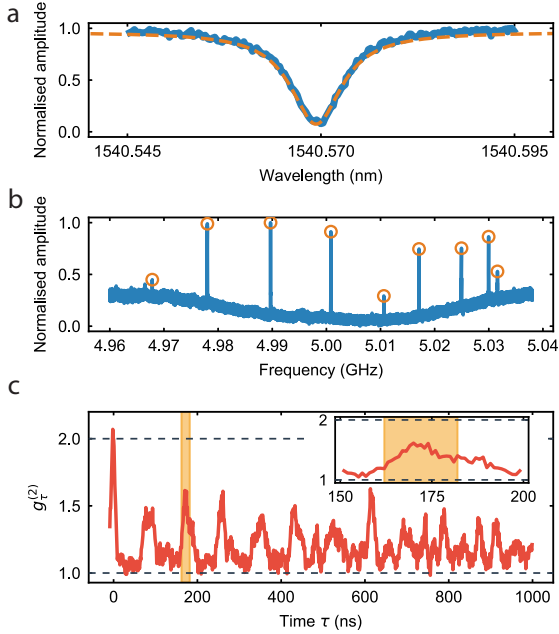


Figure 2.2: **Initial characterization.** a) Characterization of the optical resonance of the device in reflection. b) Mechanical spectrum measured using the OMIT technique at 20 mK. The series of peaks is given by the hybridization of the cavity mode and the modes of the waveguide (approximately equally spaced). c) $g_{\tau}^{(2)}$ of a waveguide-coupled thermal state for different delays between two detection events (τ). Note the series of peaks indicating the traveling back and forth of the phonons in the waveguide. The reduced maxima for these peaks is attributed to the non constant FSR. The area highlighted is the chosen round trip peak for the pulsed experiment with single phonon states. Inset: zoom-in around the highlighted area.

$\kappa_{\tau} = 1021$ MHz (with extrinsic and intrinsic loss rates of $\kappa_e = 364$ MHz and $\kappa_i = 656$ MHz). We measure the mechanical spectrum using the optomechanical induced transparency (OMIT) technique [30] (see SI for details). The resulting renormalized amplitude of the reflected probe field ($|S_{21}|$) is plotted in Fig 2.2b, where a series of (almost) equally spaced peaks shows the hybridization of the single mode of the cavity with the series of modes of the free-ended waveguide. We choose the first prominent mechanical resonance (around 4.98 GHz) as the frequency to which we detune the laser with respect to the optical resonance wavelength for addressing the Stokes and anti-Stokes interaction. We further measure the equivalent single photon optomechanical coupling rate from the Stokes scattering probability using a short optical pulse of full width at half maximum (FWHM) ≈ 40 ns, obtaining a collective $g_0/2\pi \approx 460$ kHz (for a detailed explanation see the SI). This is the joint coupling rate of all mechanical eigenmodes within the detection filter bandwidth.

In order to determine the time dynamics of the phononic wave packet, we measure the second order correlation function $g_{\tau}^{(2)}$ of the light scattered from the cavity with a CW read-out tone detuned to the anti-Stokes sideband. Due to non-negligible optical absorption in silicon, the continuous laser creates thermal mechanical population

in the device [31]. In this experiment, the continuous red-detuned laser field excites thermal phonons in a broad frequency range. These phonons are read out by the same red-detuned field, which allows us to only measure the anti-Stokes scattered photons on resonance with the optical cavity. The phononic state is therefore mapped onto the photonic state, and the photons are finally detected using our SNSPDs. As a result the photon statistics of the optical field corresponds to the phonon statistics of the thermal mechanical mode. We obtain the $g_{\tau}^{(2)}$ between emitted photons from the device, by measuring two photon coincidences on two different SNSPDs and normalizing them to the single photon counts of the SNSPDs. Owing to the optomechanical interaction, this is equivalent to measuring the $g_{\tau}^{(2)}$ of the mechanical thermal states, for different delays between the SNSPDs clicks τ . The results are plotted in Fig 2.2c, showing an (almost) equally spaced series of peaks. As expected for a thermal state, at $\tau = 0$, we observe $g_{\tau}^{(2)} = 2$, which is then modulated as the state leaks into the waveguide. We attribute the reduced maxima for the round trip peaks ($g_{\tau}^{(2)} \approx 1.5$ instead of 2) to coupling to undesirable asymmetric mechanical modes (which have relatively low optomechanical coupling rate, and thus cannot be detected optically), as well as the non-constant FSR between mechanical modes of the device, which could be caused by the dispersion of the phononic waveguide. The exact effect will require a more detailed theoretical and experimental analysis in the future.

We use three 150-MHz broad filter cavities in series to filter out the strong optical driving pumps, which also filter the Stokes and anti-Stokes scattered photons within a frequency range of 80 MHz around the setpoint (4.98 GHz). In this way, any signal from the mechanical modes greater than 5.02 GHz is strongly suppressed and hence, only the part of the spectrum with the evenly spaced mechanical modes will contribute considerably to the correlation. These modes build a frequency comb with a free spectral range (FSR) of around 11 MHz, which corresponds to a rephasing time of $1/\text{FSR} = 91$ ns. This is consistent with the round trip time that can be inferred from the measurement, which is around 85 ns.

2.3.2. ROUTING NON-CLASSICAL MECHANICAL STATES

In order to verify that we can guide a non-classical mechanical state, we employ a scheme in which we herald the creation of a quantum excitation in the optomechanical cavity, which we confirm by swapping out the mechanical excitation to an optical photon after some time and correlating the photon statistics from the two processes [29]. We obtain these correlations by measuring the coincidences between the events on the SNSPDs. We realize this scheme by first addressing the Stokes process with a 119 fJ blue-detuned 40 ns laser pulse creating a two-mode squeezed opto-mechanical state with scattering probability of $p_{s,\text{write}} \approx 1.4\%$. Similarly, to readout the mechanical state from the optomechanical cavity, a red-detuned laser pulse with the same energy, duration and scattering probability of $p_{s,\text{read}} \approx 1.4\%$, is sent to the device addressing the anti-Stokes process. These low values are chosen to avoid excess heating of the optomechanical device from the remaining optical absorption in the silicon. Note however that it has been shown that these can be increased up to around 30% [27]. These scattering probabilities set the thermal occupation of the mode of interest to $n_{\text{th}} \approx 0.27$ (see SI).

The scheme of the pulses can be seen in Fig. 2.3a and the delay between the red-

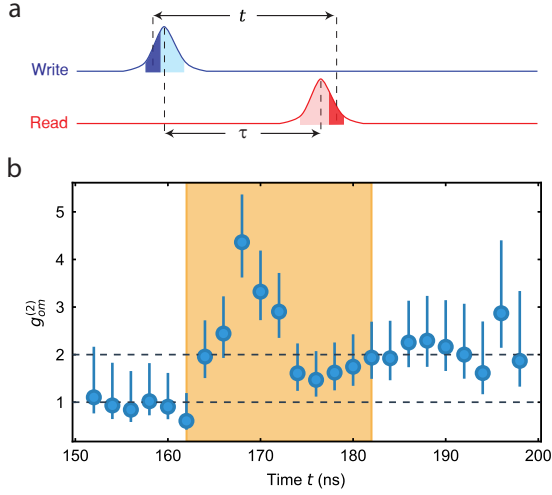


Figure 2.3: **Non-classical correlation.** a) Pulse scheme used for the cross correlation measurement. We fix the time between the pulses to $\tau \approx 170$ ns, as calibrated from the measurement of Fig 2.2c. In post-processing, we scan a narrow time window of 6 ns with an adjustable delay of t represented by the dark blue and red shaded areas over all of the acquired data (light shaded areas). This approach allows us to calculate the $g_{\text{om}}^{(2)}$ of each point with an adjustable moving window. b) Cross correlation between the optical and the mechanical state for the pulsed experiment $g_{\text{om}}^{(2)}(t)$. The correlation is higher than the classical threshold of 2, with a maxima of $g_{\text{om}}^{(2)} = 4.4^{+1.0}_{-0.7}$, clearly demonstrating the non-classical character of the traveling phonons. For more details on the error calculation see the SI 2.5. The highlighted area in the figure has the same position as the one in Fig 2.2c.

detuned and blue-detuned pulses is set to approximately the second round trip time ($\tau \approx 170$ ns). The detection of a single photon in one of the detectors from the blue-detuned pulse heralds the mechanical state of the defect to a single-phonon Fock state [27]. This phonon leaks through the attached phononic waveguide after a short time T_c and travels back and forth between the defect part and the end of the waveguide. In Figure 2.2c the highlighted area shows the chosen peak, that has a delay of $\tau \approx 170$ ns, which is much smaller than the measured lifetime $T_1 \approx 78 \mu\text{s}$ for this particular device (see the SI for more details). We choose to perform the measurement after two round trips of the phonons to avoid any overlap between the optical write and read pulses. Another reason for this is to overcome the SNSPDs' dead time of around 100 ns and hence be able to measure coincidences on the same SNSPD as well as from different SNSPDs. We would like to note that the expected cross-correlation between phonons and photons on multiple round trips is expected to be similar or slightly lower as a result of optical absorption and delayed heating [27, 29]. From this measurement, we can also infer the coupling between the cavity and the waveguide from the width of the chosen peak, obtaining a decay time of $T_c \approx 10$ ns, corresponding to a coupling rate of around $2\pi \times 16$ MHz.

In order to measure the coincidences required to determine the correlations, two 6-ns wide time windows, with a varying delay t between them, are scanned through the

whole area of pulses in a post processing step (see Fig. 2.3a). Note that we also use the measurement shown in Fig. 2.2c to calibrate these filtering windows. By summing all the coincidences with each click happening in the same trial ($\Delta n = 0$, for n indicating each trial), we gather all the correlated coincidences for each delay. In order to obtain the average uncorrelated coincidences, we perform a similar post processing step, but finding coincidences in different trials ($\Delta n \neq 0$) where the clicks can be assumed to be uncorrelated. Averaging this value over different $\Delta n \neq 0$, gives the average number of uncorrelated coincidences. We use these two values to calculate $g_{\text{om}}^{(2)}(t)$. The time window is chosen to be less than the coupling time between the cavity and the waveguide (T_c) in order to select only the correlated photons that have indeed traveled in the waveguide (see SI for more details). The result is shown in Fig. 2.3b. In order to gather more statistics, two separate measurements with identical thermal occupation have been used for the data shown here, one with the sequence of red and blue pulses repeated every $200\mu\text{s}$, the other every $300\mu\text{s}$. After merging all the coincidences, a maximum cross-correlation of $g_{\text{om}}^{(2)} = 4.4^{+1.0}_{-0.7}$ is obtained from the reflected phonons at a time of $t = 168\text{ns}$, which is more than 3 standard deviations above the classical threshold of 2, unambiguously showing the non-classical behavior of the guided single phonon state [29]. Furthermore, no non-classical correlations between the photons can be observed at times where the phonon is not spatially located inside the defect (i.e. outside a window of width T_c centered at $t \approx \tau \approx 170\text{ns}$). We suspect the slightly increased correlations at longer times to be a result of the waveguide dispersion. This effect is also clearly visible in the envelope of the peak shape corresponding to the second round trip in the inset of Fig. 2.2c, with both patterns closely resembling one another.

We further explore the potential of creating a time-bin encoded phononic state by extending our scheme to using two optical excitation (write) and two detection pulses (read), effectively realizing a phononic FIFO quantum memory [32]. The identical blue-detuned optical pulses (FWHM 40ns) have a scattering probability of $p_{\text{s,write}} \approx 2.7\%$ with $\Delta\tau = 45\text{ns}$ delay. The red-detuned detection pulses (FWHM 40ns) have a scattering probability of $p_{\text{s,read}} \approx 1.5\%$ and with the same time delay. The first blue- and red-detuned pulses are spaced by $\tau = 170\text{ns}$ from each other and we repeat this sequence every $800\mu\text{s}$. We then measure the maximum cross correlation in time between all four combinations of write and read pulses, using the same technique for delay-filtering used to extract the data shown in Fig. 2.3. We choose 40-ns-long non-overlapping time windows to separate "early" write and read pulses from "late" ones, as depicted in Fig. 2.4a. As shown in Fig. 2.4b, we can clearly see strong non-classical correlation between the "early-early" and "late-late" combination of excitation and detection pulse, while observing only classical correlations (due to absorption-induced heating) between the other combinations of "early-late" and "late-early".

2.4. CONCLUSION AND DISCUSSION

Our results clearly demonstrate the potential for creating, guiding, and detecting a non-classical mechanical state inside a phononic crystal, using optomechanical techniques. Thanks to the long mechanical lifetime (up to 5.5ms for similar devices on the same chip) and the full lateral confinement, this type of device paves the way towards on-chip quantum acoustic experiments. The current efficiency of the device is limited by

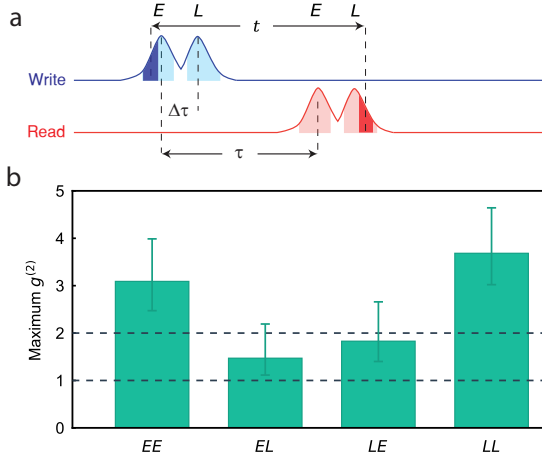


Figure 2.4: **Double pulse non-classical correlation.** a) Pulse scheme for the generation of time-bin encoded phonon states with $\Delta\tau = 45$ ns and $\tau = 170$ ns. The area used to gather coincidences is depicted by the light blue (red) shaded area for the write (read) pulses, respectively. In the post-processing step a similar technique as before is used, in order to achieve high timing resolution. An example of 6 ns wide coincidence-filtering windows are sketched by dark blue (red) areas for write (read) pulses for the "early-late" combination. *E* (*L*) stands for early (late). b) As expected, the maximum cross correlations for the various settings clearly shows non-classical correlations for the "early-early" and "late-late" combinations, whereas in the other two we only observe classically correlated phonons.

residual optical absorption in the silicon, which can be reduced through improved fabrication [27] and surface passivation [33]. While some of the motivation for these experiments stems from the similarity to quantum optics, phonons are crucially different, due to the 5 orders of magnitude smaller propagation speed and the ease of coupling them to other quantum systems. The realization of phononic beamsplitters and phase modulators will complete the toolbox required for full control over traveling single phonons and more complex quantum experiments on a chip. Furthermore, the possibility of retrieving the state after several round-trips and with having time-bin encoded phononic states, together with the full engineerability of the bandstructure, will allow for the creation of time-bin encoded phononic qubits and an optomechanical multimode quantum memory working natively at telecom wavelengths. We also expect guided phonon modes to play a crucial role in the low-energy transmission of quantum information on a chip and for next generation filtering.

Acknowledgments We would like to thank Ewold Verhagen and Roel Burgwal for valuable discussions, as well as Moritz Forsch for experimental support. We further acknowledge assistance from the Kavli Nanolab Delft. This work is financially supported by the European Research Council (ERC CoG Q-ECHOS, 101001005), and by the Netherlands Organization for Scientific Research (NWO/OCW), as part of the Frontiers of Nanoscience program, as well as through Vidi (680-47-541/994) and Vrij Programma (680-92-18-04) grants. R.S. also acknowledges funding from the European Union under a Marie Skłodowska-Curie COFUND fellowship.

Author Contributions: A.Z., R.S. and S.G. devised and planned the experiment. A.Z. simulated, designed and fabricated the sample. A.Z., R.S. and N.F. built the setup and performed the measurements. All authors analysed the data and wrote the manuscript. S.G. supervised the project.

Competing Interests: The authors declare no competing interests.

Data Availability: Source data for the plots are available on [Zenodo](#).

2.5. SUPPLEMENTARY INFORMATION

FABRICATION

The device is fabricated from a silicon-on-insulator chip with a device layer of 250 nm. We first pattern the structure using electron-beam lithography into the resist (CSAR) and then transfer it to the silicon layer with a SF_6/O_2 reactive-ion etch. The structure is then cleaned with a piranha solution and suspended by undercutting the sacrificial oxide layer using hydrofluoric acid (HF). A last cleaning step with piranha and diluted HF (1%) is performed just before mounting the sample in the dilution refrigerator.

EXPERIMENTAL SETUP

A complete overview of the experimental setup is shown in Fig. 2.5. The optical control pulses are created from two separate tunable CW external-cavity diode lasers. They are stabilized over time using a wavelength meter (not shown) and are filtered with fiber based filter cavities (50 MHz linewidth) to suppress the classical laser noise at GHz frequencies. We create the pulses using two 110 MHz acousto-optic modulators (AOMs) gated via a pulse generator. The optical paths are combined through a fiber beamsplitter. The pulses are routed to the device in the dilution refrigerator via an optical circulator, and then to the device's optical waveguide using a lensed fiber. The optical signal coming from the device is filtered with three 150 MHz broad free-space Fabry-Pérot cavities in series, that results into an equivalent series bandwidth of about 80 MHz. The average suppression ratio is 114 dB for the blue detuned pulse and 119 dB for the red detuned pulse (the small difference is due to small misalignment and mode mismatch of the cavities). Every ~ 10 s the experiment is paused and continuous light is sent to the filter cavities to lock them at the optical resonance of the device using optical switches. For this, the red-detuned laser is used after passing through a 50:50 beam splitter, and the detuning is compensated via an electro-optics modulator to match the optical resonance. It takes around 6 s to lock the cavities each time.

The effect of dark counts, mostly unwanted photons from stray light which couple into the fiber and leakage of pump photons through the filter chain, are negligibly small compared to the photon rate that is obtained via the Stokes and anti-Stokes scatterings. During the cross-correlation measurement shown in Fig. 2.3, we get total photon rates of approximately 8×10^{-4} and 1.7×10^{-4} per trial from the Stokes and anti-Stokes scatterings, respectively, from the full area of optical pulses. At the same time, the average total dark count rate, which is constant in time, is only 1×10^{-5} per trial.

COHERENT EXCITATION MEASUREMENT

Here we study the routing of a coherent mechanical wavepacket, as a verification to the round-trip time of the measurement of Fig. 2.2c of the main text. We excite the mechanical wave packet with a 40 ns long pulse of laser light, blue-detuned by 7 GHz with respect to optical resonance of the cavity. Importantly, as the Stokes scattered photons are more than two linewidths away from the optical resonance, the Stokes process will be highly attenuated. We pass this laser pulse through an electro-optical modulator (EOM) which produces two side bands at around 4.978 GHz (the frequency of the mechanical mode which we use to detune our lasers and also lock our free space filter cavities in front of the

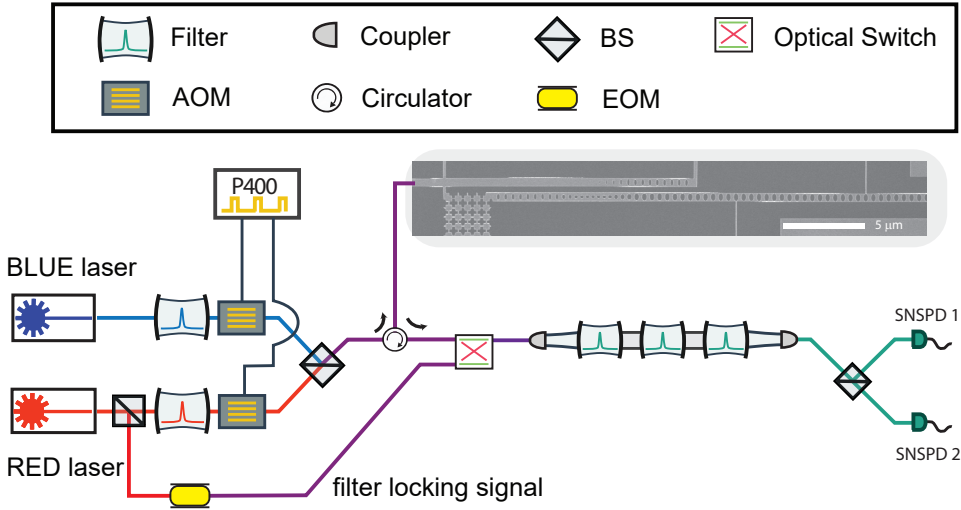


Figure 2.5: The experimental setup, with BS the beam splitter and SNSPD the superconducting nanowire single-photon detectors. See text for more details.

SNSPDs). The beating signal between these optical sidebands and the main carrier frequency now results in a coherent driving of the mechanical modes in a broad frequency range, which excites a mechanical packet inside the cavity. Following this excitation, we use a continuous red-detuned laser tone to continuously read the mechanical population. The resulting count rate from this read tone is shown in Fig. 2.6a. We can clearly see the propagating behavior of the packet, first leaving the cavity resulting in a reduction of the population, followed by the reflection back to the cavity.

In order to verify that the reflection is indeed a result of the phonon leaving the cavity, we perform the same measurement on an identical device, with a 2.5 times longer waveguide attached to it. As expected, the longer waveguide should result in a 2.5 times longer traveling time of the packet, which is fully consistent with the time difference between the peaks in Fig. 2.6b. Note that the two experiments are performed with different power settings of the coherent drive and the readout compared to the experiments in the main text, which is the reason of not seeing a full decay of the click rates in Fig. 2.6a. This results in an increased thermal background introduced by the high power readout laser, as well as the pulse length of 40 ns that is comparable with the round trip time of that device. Additionally, the peak widths are broader, since in this experiment only the modes within the bandwidth of the laser pulse will be excited. Therefore, the time domain behavior is limited by the bandwidth of the laser pulse as it is much narrower than the cavity-waveguide coupling and the bandwidth of the filter cavities.

SCATTERING PROBABILITIES

The Stokes and anti-Stokes scattering probabilities are determined from the click rates (Γ_r , Γ_b) on the SNSPDs and by measuring the detection efficiency of the experimental

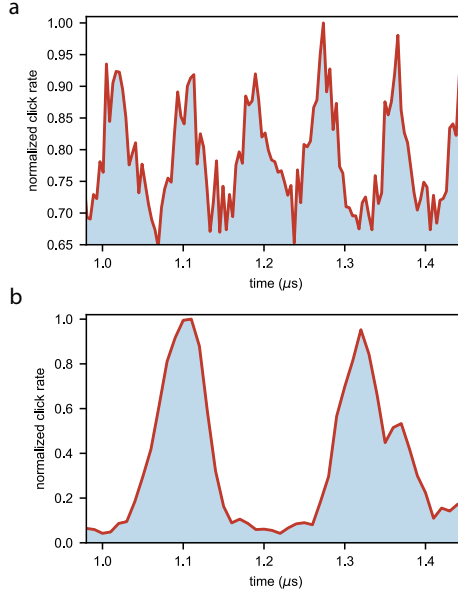


Figure 2.6: Coherent mechanical population of the cavity versus time for different waveguide lengths of a) $92 \mu\text{m}$ and b) $230 \mu\text{m}$. The time difference between the two peaks in the bottom figure is around $\tau \approx 210 \text{ ns}$ compared to $\tau \approx 85 \text{ ns}$ for the shorter waveguide, which is fully consistent with the difference in waveguide length.

setup (η_{det})

$$\Gamma_{\text{r}} = p_{\text{s,read}} \cdot n_{\text{th}} \cdot \eta_{\text{det}} \quad (2.1)$$

$$\Gamma_{\text{b}} = p_{\text{s,write}} \cdot (1 + n_{\text{th}}) \cdot \eta_{\text{det}} \quad (2.2)$$

where the $p_{\text{s,read}}$ and $p_{\text{s,write}}$ are the scattering probabilities from the red detuned (anti-Stokes) and blue detuned (Stokes) laser pulses, respectively, and n_{th} is the mechanical mode thermal phonon occupancy. The measurement of the detection efficiency gives $\eta_{\text{det}} \approx 3.8\%$. This includes the coupling between the optical cavity and the optical coupler waveguide η_{dev} , the coupling from fiber to the optical coupler waveguide η_{c} , the filter setup efficiency η_{F} , the SNSPDs detection efficiency η_{SNSPD} , as well as all other losses in the optical path η_{loss} . Hence, the overall detection efficiency can be written as $\eta_{\text{det}} = \eta_{\text{c}} \cdot \eta_{\text{dev}} \cdot \eta_{\text{F}} \cdot \eta_{\text{SNSPD}} \cdot \eta_{\text{loss}}$. By shining a continuous off-resonance laser to the device and measuring the power at each point of the setup, we obtain $\eta_{\text{c}} = 37\%$, $\eta_{\text{F}} = 38\%$, $\eta_{\text{SNSPD}} \approx 90\%$ and $\eta_{\text{loss}} \approx 80\%$. Furthermore, the device efficiency $\eta_{\text{dev}} = \frac{\kappa_{\text{e}}}{\kappa_{\text{t}}}$ and is measured using a similar method to [34].

In the weak coupling regime ($g \ll \kappa$), the scattering probabilities are given by the efficiency ($\eta_{\text{dev}} = \frac{\kappa_{\text{e}}}{\kappa_{\text{t}}}$) and the incident laser pulse energy E_{p} [27]:

$$p_{s,\text{read}} = 1 - \exp\left(\frac{-4\eta_{\text{dev}}g_0^2E_p}{\hbar\omega_c(\omega_m^2 + (\kappa_t/2)^2)}\right) \quad (2.3)$$

$$p_{s,\text{write}} = \exp\left(\frac{4\eta_{\text{dev}}g_0^2E_p}{\hbar\omega_c(\omega_m^2 + (\kappa_t/2)^2)}\right) - 1 \quad (2.4)$$

where ω_c is the optical resonance frequency and ω_m the mechanical frequency.

BAND STRUCTURE

The band structure of the waveguide can be engineered by changing the hole dimensions and the periodicity of unit cells, while keeping the width and thickness of the beam fixed. In Fig. 2.7 three designs of a waveguide with different mechanical band structure and group velocity are shown. All these designs act as optical mirrors for the cavity, as can be seen from the optical band diagrams.

LIFETIME

One of the fundamental properties of the device is the extremely long lifetime T_1 of the mechanical excitation. In order to measure T_1 we use a red detuned strong optical pulse to heat the device, creating a thermal population in the mode. We then send another, much weaker, red detuned pulse, to probe the thermal population as a function of time, which is directly proportional to the clickrates. The result of the measurement is shown in Fig. 2.8. Note that, as previously seen [7], the clickrates have a double exponential trend, with a rise time T_{rise} and a decay time T_1 . For our measurement we choose one of the shorter lifetime devices (to allow for higher repetition rates), while several structures with up to 5.5 ms are also fabricated on the same chip, as shown in the plot.

THERMAL OCCUPANCY OF THE MECHANICAL MODE

The mechanical modes, having a frequency of around 5 GHz, have a thermal occupation of $< 10^{-5}$ at 20 mK. Due to absorption of the optical pulses used to create and read the state, the thermal occupation during the experiment is however significantly higher. We measure the mode temperature via the sideband asymmetry as shown in figure Fig. 2.9a. In more detail, we send a blue-detuned and red-detuned optical pulse with exactly equal energies (and thus equal scattering probabilities) and a long delay between (few times of the mechanical lifetime in order to reinitialize to the ground state at the starting of each pulse) and measure the click rates from each pulse (Γ_r, Γ_b). Using Eq. 2.1 and 2.2, we extract the thermal occupancy for different scattering probabilities. This measurement allows us calibrate the mode heating that occurs during the optical red-detuned (anti-Stokes) pulse, the instantaneous heating. To mimic the real experimental conditions with two pulses (as used for Fig. 2.3a), we send an additional red detuned pulse to the device 170 ns before the pulses used to measure the thermal occupation, which effectively heats the mechanical mode. The results are shown in Fig. 2.9b, where the x-axis is the inferred scattering probability of the heating pulse.

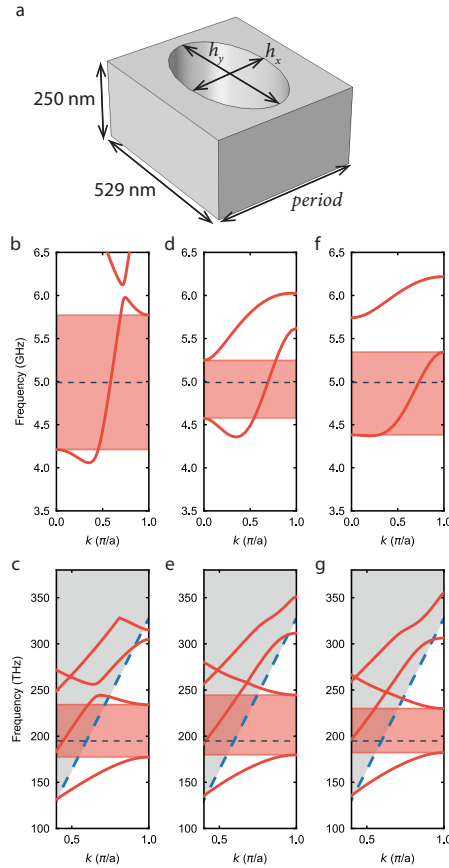


Figure 2.7: Engineering the band structure and phonon group velocity by adjusting the hole dimensions: h_x diameter along the waveguide orientation, h_y , diameter perpendicular to the waveguide orientation, and the size of the unit cell (period). A sketch of the unit cell is shown in a. b,c) Mechanical and optical band diagram for a waveguide with parameters of $h_y = 187$ nm, $h_x = 320$ nm, $period = 436$ nm resulting in a mechanical group velocity of $v_g = 6298$ m/s. d,e) Parameters of $h_y = 430$ nm, $h_x = 272$ nm, $period = 458$ nm, with $v_g = 2766$ m/s. f,g) Parameters of $h_y = 468$ nm, $h_x = 240$ nm, $period = 458$ nm, with $v_g = 1946$ m/s. In our experiment, we use the second set of parameters (shown in d) and e)) in order to have a small group velocity, while simultaneously maintaining a linear region of the mechanical band to minimize dispersion.

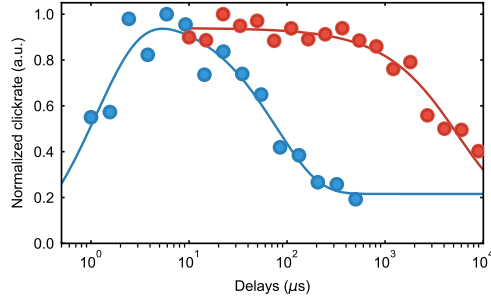


Figure 2.8: Normalized clickrates (directly proportional to the thermal population) from a thermally excited mechanical mode as a function of time. The population exhibits a double exponential behavior, which corresponds to the initial heating and subsequent decay. For the device used in the measurements the rise and decay times are $T_{\text{rise}} \approx 1 \mu\text{s}$ and $T_1 \approx 78 \mu\text{s}$ (data in blue), respectively. An exemplary second device, with increased number of phononic shield periods connected to the tethers, resulting in a much longer decay time $T_1 \approx 5.5 \text{ ms}$ is also shown (data in red). The solid lines are exponential fits to the data.

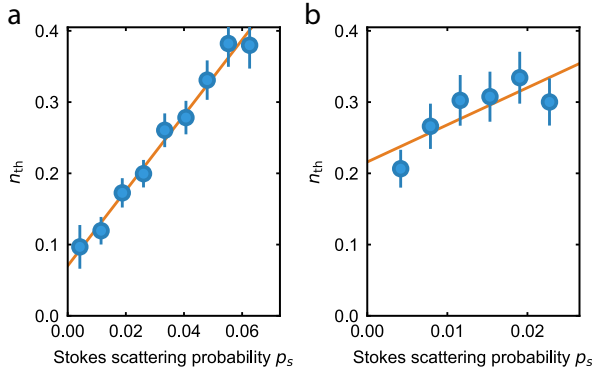


Figure 2.9: a) Thermal occupation of the mode of interest as a function of the scattering probability of the Stokes and anti-Stokes process $p_{\text{s,write}} = p_{\text{s,read}} = p_{\text{s}}$. n_{th} is measured from the asymmetry of Stokes/anti-Stokes scattering rates. The fit follows $n_{\text{th}} = (0.070 \pm 0.0095) + (5.29 \pm 0.25) \times p_{\text{s}}$. We choose to work at $p_{\text{s,read}} = 1.4\%$. b) Thermal occupation with the pulse scheme of the experiment as a function of the inferred scattering probability of the anti-Stokes process for the heating pulse. Here a heating pulse is sent to the device 170 ns before the pulses used to measure the thermal occupation. Since the heating dynamics is similar for both Stokes and anti-Stokes processes, we can send either a red-detuned or a blue-detuned pulse as heating pulse. The fitting of the resulting data follows $n_{\text{th}} = (0.216 \pm 0.028) + (5.21 \pm 1.88) \times p_{\text{s}}$. Choosing a scattering probability of $p_{\text{s,write}} = 1.4\%$ results in a total thermal occupation of $n_{\text{th}} \approx 0.27$. In both figures the fits are linear and the errors are one standard deviation.

ERROR ON THE $g_{\text{OM}}^{(2)}$

As discussed in the main text, we record the coincidences from the same trial ($N_{\Delta n=0}$, where n is an indicator for each experimental round), and the average number of coincidences from different trials ($\bar{N}_{\Delta n \neq 0}$), which is expected to be uncorrelated. In order to calculate the $g_{\text{om}}^{(2)}$ we divide these two quantities, such that $g_{\text{om}}^{(2)}(t) = N_{\Delta n=0}(t) / \bar{N}_{\Delta n \neq 0}(t)$.

Using $\Delta n \gg 1$, one can gather enough statistics to estimate $\overline{N}_{\Delta n \neq 0}$ with a negligible error. For the estimation of the error on $N_{\Delta n=0}$, which dominates the statistical uncertainty, a binomial distribution function is considered for the number of coincidences on each trial. Therefore, from this distribution, the probability of getting different numbers of coincidences can be calculated and thus, the error of the number of coincidences will be estimated. This is similar to the method used in [29].

EFFECT OF TIME FILTERING WINDOW ON $g_{\text{OM}}^{(2)}$

Due the strong coupling between the optomechanical defect and the mechanical waveguide, the phononic packet has a narrow length of around $T_c \approx 10$ ns. Therefore, in order to study the non-classical properties of the phononic packet, we have to filter the coincidences happening with a certain delay in time, with a narrow time window around that delay. In Fig. 2.3 the width of the time filtering window is 6 ns and the delay of the window is scanned through the write and read pulses for each delay. The cross-correlation is calculated by dividing the number of coincidences happening in the same trial ($\Delta n = 0$), by the number of coincidences happening in different trials ($\Delta n \neq 0$), which are uncorrelated. By changing the filtering window, the number of uncorrelated coincidences resulting from the thermal background noise of mechanical motion is changed, reducing the cross correlations resulting from the heralded mechanical state. To further study this effect, we plot the cross correlations in Fig. 2.10, where we increase the filtering window from 3 ns to 30 ns. As can be seen, with a shorter filtering window the number of coincidences gathered for each delay is a reduced and thus, despite having a higher cross correlation, the error bars of the measurement is also larger. For window widths smaller than the packet lifetime we recover strong correlations, however for widths shorter than 5 ns we only obtain a small number of coincidences, resulting in an increased uncertainty in the correlation parameter. For windows longer than the packet length, the increased contribution of uncorrelated coincidences reduces the measured correlations. Please note that the cross-correlations of classical state can never exceed 2.

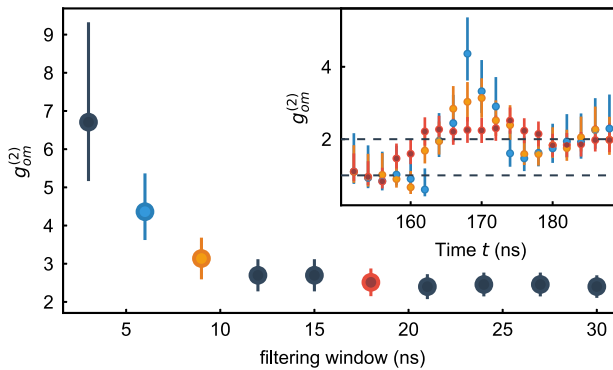


Figure 2.10: Maximum cross correlations obtained with varying filtering window width, using similar time delays as in Fig. 2.3. Inset: full cross correlations as a function of time for 3 selected data points.

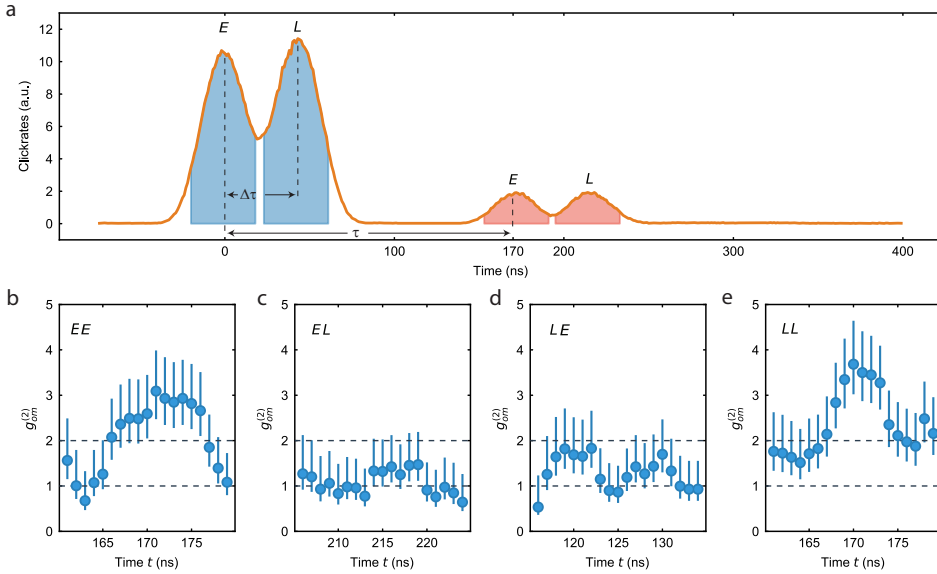


Figure 2.11: a) Double-pulse click rate versus time. The two slightly overlapping write pulses preceding the read pulses are clearly distinguishable into earlier and later time. The delay between pulses is $\tau = 170$ ns for both "early-early" and "late-late" combinations, $\tau + \Delta\tau = 215$ ns for "early-late", and $\tau - \Delta\tau = 125$ ns for "late-early". b) Cross correlation between coincidences having a delay not more than 10 ns deviation from the delay between pulses, for different combinations. In all figures here "E" ("L") stands for "early" ("late").

DOUBLE PULSE $g_{\text{OM}}^{(2)}(t)$

In this experiment we use two write and two read pulses. In Fig. 2.11a, the click rates are shown in time. The two pairs of pulses are clearly overlapping, since the delay between them is close to their FWHM. We gather coincidences from the shaded area of the pulses, choosing them to not overlap to not double count coincidences. We use a similar technique to the one use for Fig. 2.3, with filtering the coincidences in a 6 ns time window with varying delays, in order to obtain finer time resolution. In Fig. 2.11b, the cross correlation between these fine-filtered coincidences is shown as a function of delay between them for different combinations of write and read pulse. The maximum cross correlation of these plots is depicted in Fig. 2.4b. Note that the maximum cross correlation for "early-early" and "late-late" combinations happen at $t \approx 170$ ns which matches the second round trip of phonons, as expected.

THEORY OF OPTOMECHANICAL INDUCED TRANSPARENCY

We assume to have an optomechanical cavity which is coupled to a truncated waveguide, acting as a Fabry-Pérot interferometer, and can write the total Hamiltonian ($\hbar = 1$) as

$$\begin{aligned}
 H = & \omega_c a^\dagger a + \omega_m b^\dagger b + \sum_l \omega_l c_l^\dagger c_l + \sum_l \gamma_{e,l} c_l^\dagger b + h.c. \\
 & + g_0 a^\dagger a (b^\dagger + b)
 \end{aligned} \tag{2.5}$$

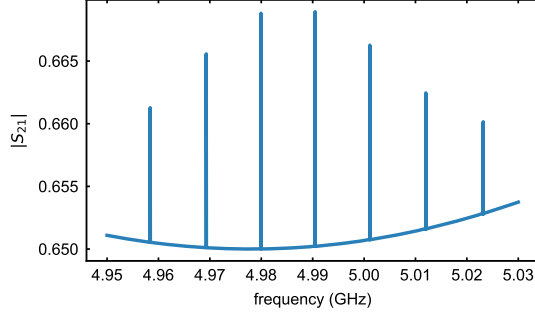


Figure 2.12: Numerically calculated S_{21} signal, using the parameters given in the main text.

where a and b are the annihilation operators for the optical and mechanical modes of the optomechanical cavity and g_0 represents the single photon optomechanical coupling rate. Additionally, $\gamma_{e,l}$ represents the coupling between the mechanical mode of the cavity and the l -th mode of the Fabry-Pérot interferometer with annihilation operator c_l and frequency ω_l .

The linearized Hamiltonian in the rotating frame of the laser field after applying the perturbation over the optical field is then given by [1]

$$H = \Delta a^\dagger a + \omega_m b^\dagger b + g_0 \alpha (a^\dagger + a)(b^\dagger + b) + \sum_l \Omega_l c_l^\dagger c_l + \sum_l \gamma_{e,l} c_l^\dagger b + h.c. \quad (2.6)$$

where $\Delta = \omega_c - \omega_l$ is the detuning of the cavity with respect to the laser frequency. Here, a is now the annihilation operator for the optical field fluctuation inside the cavity with the steady state field of α . The equivalent optomechanical coupling to the field fluctuation is defined by $g = g_0 \alpha$.

The Langevin equations after applying the rotating wave approximation, by assuming having the pump field at the red sideband and neglecting the counter rotating terms, follow as

$$\frac{da}{dt} = -i\Delta a - igb - \frac{\kappa}{2}a + \sqrt{\kappa_e} a_{in} \quad (2.7)$$

$$\frac{db}{dt} = -i\omega_m b - ig a - \frac{\Gamma_m}{2}b - i \sum_l \gamma_{e,l} c_l \quad (2.8)$$

$$\frac{dc_l}{dt} = -i\omega_l c_l - i\gamma_{e,l} b - \frac{\Gamma_l}{2}c_l \quad (2.9)$$

Here κ is the optical decay which includes both external and internal cavity loss $\kappa = \kappa_e + \kappa_i$. Similarly, Γ_m and Γ_l are the mechanical decay rate for the cavity mechanical mode and l -th mechanical mode of the Fabry-Pérot interferometer, respectively. Also, a_{in} are the cavity input field fluctuations.

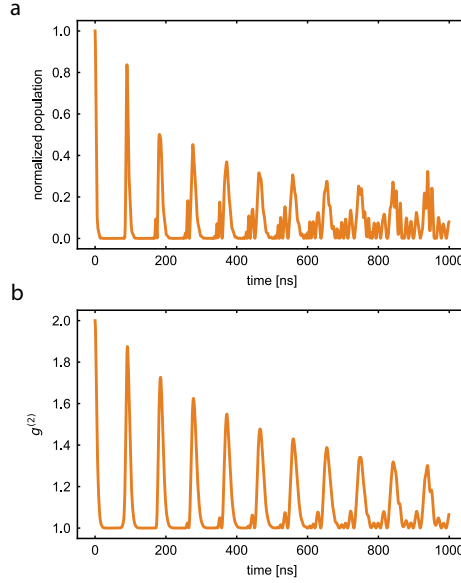


Figure 2.13: a) Simulated normalized cavity population as a function of time, detected after passing through the filter cavities. b) Second order correlation function of the cavity mechanical field, calculated using the Siegert relation.

For an OMIT measurement we pass the pump laser field through an amplitude EOM which produces sidebands at frequency ω , thus the input field to the system can be written as $E_0 + E_+ e^{-i\omega t} + E_- e^{i\omega t}$. We are now interested in calculating the reflection coefficients of each component and eventually calculate the output field as $a_{out} = r_0 E_0 + r_+ E_+ e^{-i\omega t} + r_- E_- e^{i\omega t}$. Without loss of generality, we can assume that the two sidebands are equal and produced in-phase ($E_+ = E_- = E_1$) by the amplitude EOM. Moreover, by operating in the resolved sideband regime ($\kappa < \omega_m, \Delta$), the fields at frequencies far detuned from the cavity frequency reflect identically and we can assume $r_0 \approx r_- \approx 1$. We therefore have to only calculate the reflection coefficient of the component close to the cavity resonance r_+ . By considering only this input field in Eq. 2.7 and assuming $a = a_+ e^{-i\omega t}$, $b = b_+ e^{-i\omega t}$ and $c_l = c_{+,l} e^{-i\omega t}$, we have

$$b_+ = \frac{g}{\omega - \omega_m + i\frac{\Gamma_m}{2} - \sum_l \frac{\gamma_{e,l}^2}{\omega - \omega_l + i\frac{\Gamma_l}{2}}} a_+ \quad (2.10)$$

$$a_+ = \frac{i\kappa_e}{\omega - \Delta + i\frac{\kappa}{2} - \chi(\omega)} E_1 \quad (2.11)$$

$$\chi(\omega) = \frac{g^2}{\omega - \omega_m + i\frac{\Gamma_m}{2} - \sum_l \frac{\gamma_{e,l}^2}{\omega - \omega_l + i\frac{\Gamma_l}{2}}} \quad (2.12)$$

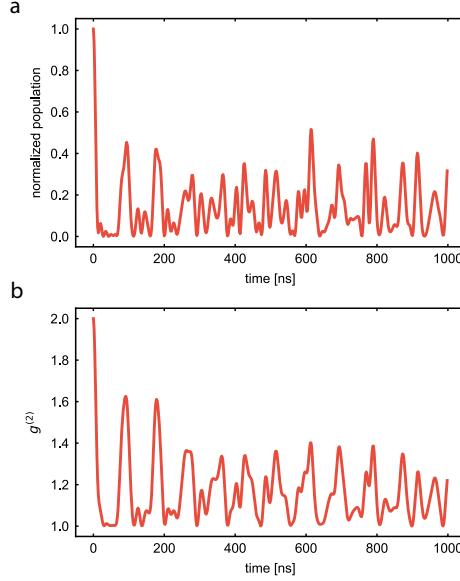


Figure 2.14: We apply the same model to the OMIT spectrum measured for the real device in the main text, obtaining the cavity population and $g^{(2)}$ of a thermal state as a function of time.

with $\chi(\omega)$ being the mechanical susceptibility to the optical field. After that, by using the input-output relation of $a_{out} = a_{in} - \sqrt{\kappa_e}a$, we can extract the reflection coefficient as

$$r_+ = 1 - \frac{i\kappa_e}{\omega - \Delta + i\frac{\kappa}{2} - \chi(\omega)} \quad (2.13)$$

A fast photodiode detects the power of the output field as

$$P = |E_0|^2 + |E_1|^2 + |r_+E_1|^2 + E_0E_1e^{-i\omega t} + r_+E_0E_1e^{-i\omega t} + r_+|E_1|^2e^{-i2\omega t} + c.c. \quad (2.14)$$

The voltage produced by the fast photodiode is connected to channel 2 of a vector network analyzer (VNA) which measures the quadratures of the signal, and thus measures S_{21} with magnitude of $|S_{21}| = \frac{1 + \text{Re}\{r_+\}}{2}$. For simplicity, we assume all the Fabry-Pérot interferometer modes to have a similar coupling rate to the cavity. We now numerically calculate and plot this signal in Fig. 2.12 given the parameters of the system, which are reported in the main text. The resulting graph is very similar to the measurement shown in Fig. 2.2b. Note that the peaks in the transparency window at each mechanical mode are a direct result of the optomechanical coupling in the denominator of Eq. 2.13.

MECHANICAL RESPONSE OF THE CAVITY-WAVEGUIDE STRUCTURE

In order to develop a simple theoretical model describing the measurements in Fig. 2.2c in the main text we first look at the time domain behavior of the mechanical system and then calculate its $g^{(2)}$ function. The state-swap interaction performed with the red-detuned optical drive is such that the optical $g^{(2)}$ we recover reproduces the mechanical state [27]. For the time domain response we use Eq. 2.8 and Eq. 2.9, where we set the optomechanical interaction term to zero ($g \approx 0$). We solve them using a Python module that solves a system of linearly coupled differential equations (Scipy.integrate.odeint module), with the initial conditions of having a unity population in the cavity ($b(0) = 1$) and all the Fabry-Pérot interferometer modes in the vacuum state ($c_l(0) = 0$). For simplicity, we solve the time dynamics for scalar classical fields. We then use the solution of $b(t)$ to further obtain the cavity population and the first order correlation function $g^{(1)}$

$$g_{\tau}^{(1)} = \frac{\int \langle b^{\dagger}(t)b(t+\tau) \rangle dt}{\int \langle |b(t)|^2 \rangle dt} \quad (2.15)$$

We then proceed by using the Siegert relation [35] to calculate the second order correlation $g_{\tau}^{(2)}$ of a thermal chaotic field

$$g_{\tau}^{(2)} = 1 + |g_{\tau}^{(1)}|^2 \quad (2.16)$$

The general results for our simple model including the time domain response of the cavity population, as well as the intensity correlation $g_{\tau}^{(2)}$ are shown in Fig. 2.13. The model clearly shows that having the adjacent waveguide results in a leakage of the phonon population, followed by a subsequent revival after each round-trip with the reflection from the free-standing end. A similar behavior is observed for the intensity correlation, where $g_{\tau}^{(2)}$ decays as the thermal field leaves the cavity and then rises again as the mechanical field reflects back into the cavity.

We can now use the same method in combination with the measured OMIT data as the input and simulate the expected time domain response, as well as the mechanical $g_{\tau}^{(2)}$ as a function of time, using the same assumptions as above (see Fig. 2.14). This simple model allows us to qualitatively model our measured data from Fig. 2.2c very well.

2.6. APPENDIX

In this appendix we report some facts and some *a posteriori* consideration on the experiment reported in this chapter. The idea is to give insights on the challenges encountered on the path to acquire the final dataset.

- Since a cooldown and a warm up of a dilution refrigerator takes 3 days, having a reliable metric to characterize the devices at room temperature was a fundamental part of this work. As shown in SI section 2.5, we found that the mechanical spectrum is a reliable metric to determine the bouncing pattern of the phononic packet. The band structure engineering is a very crucial part in order to design a linear and single mode phononic waveguide that is also robust enough against fabrication disorders and imperfections.

- Having low thermal occupancy is a crucial part for creating and detecting non-classical mechanical states with high purity. Optical absorption of the material is the main factor that creates thermal occupation in our optomechanical devices. In this regard, the silicon etching step in the fabrication recipe has a great importance in order to have devices with high surface qualities, which eventually reduces the optical heating. Additionally, surface treatment techniques can be used in order to further improve the surface quality and prevent oxidation of silicon devices.
- Having a constant FSR in the mechanical spectrum - i.e. linear dispersion in the phononic waveguide - is fundamental to have high $g_{\text{om}}^{(2)}$ on the bounced phonons, which is of great importance for on-chip quantum information transfer. However having also a short lifetime is important to reduce the integration time. We suggest to have most of the devices with short lifetime on chip and only a few, as proof of principle, with long lifetime.

REFERENCES

- [1] M. Aspelmeyer, T. J. Kippenberg, and F. Marquardt, Cavity optomechanics, *Rev. Mod. Phys.* **86**, 1391 (2014).
- [2] A. D. O’Connell, M. Hofheinz, M. Ansmann, R. C. Bialczak, M. Lenander, E. Lucero, M. Neeley, D. Sank, H. Wang, M. Weides, J. Wenner, J. M. Martinis, and A. N. Cleland, Quantum ground state and single-phonon control of a mechanical resonator, *Nature* **464**, 697 (2010).
- [3] T. Palomaki, J. Teufel, R. Simmonds, and K. Lehnert, Entangling mechanical motion with microwave fields, *Science* **342**, 710 (2013).
- [4] R. Riedinger, A. Wallucks, I. Marinković, C. Löschnauer, M. Aspelmeyer, S. Hong, and S. Gröblacher, Remote quantum entanglement between two micromechanical oscillators, *Nature* **556**, 473 (2018).
- [5] C. F. Ockeloen-Korppi, E. Damskägg, J.-M. Pirkkalainen, M. Asjad, A. A. Clerk, F. Massel, M. J. Woolley, and M. A. Sillanpää, Stabilized entanglement of massive mechanical oscillators, *Nature* **556**, 478 (2018).
- [6] I. Marinković, A. Wallucks, R. Riedinger, S. Hong, M. Aspelmeyer, and S. Gröblacher, An optomechanical Bell test, *Phys. Rev. Lett.* **121**, 220404 (2018).
- [7] A. Wallucks, I. Marinković, B. Hensen, R. Stockill, and S. Gröblacher, A quantum memory at telecom wavelengths, *Nat. Phys.* **16**, 772 (2020).
- [8] R. W. Andrews, R. W. Peterson, T. P. Purdy, K. Cicak, R. W. Simmonds, C. A. Regal, and K. W. Lehnert, Bidirectional and efficient conversion between microwave and optical light, *Nature Phys.* **10**, 321 (2014).
- [9] A. Vainsencher, K. J. Satzinger, G. A. Peairs, and A. N. Cleland, Bi-directional conversion between microwave and optical frequencies in a piezoelectric optomechanical device, *Appl. Phys. Lett.* **109**, 033107 (2016).
- [10] M. Forsch, R. Stockill, A. Wallucks, I. Marinković, C. Gärtner, R. A. Norte, F. van Otten, A. Fiore, K. Srinivasan, and S. Gröblacher, Microwave-to-optics conversion using a mechanical oscillator in its quantum groundstate, *Nature Phys.* **16**, 69 (2020).
- [11] M. Mirhosseini, A. Sipahigil, M. Kalaei, and O. Painter, Superconducting qubit to optical photon transduction, *Nature* **588**, 599 (2020).
- [12] S. J. M. Habraken, K. Stannigel, M. D. Lukin, P. Zoller, and P. Rabl, Continuous mode cooling and phonon routers for phononic quantum networks, *New J. Phys.* **14**, 115004 (2012).
- [13] P. Delsing *et al.*, The 2019 surface acoustic waves roadmap, *J. Phys. D: Appl. Phys.* **52**, 353001 (2019).

- [14] M. J. A. Schuetz, E. M. Kessler, G. Giedke, L. M. K. Vandersypen, M. D. Lukin, and J. I. Cirac, Universal Quantum Transducers Based on Surface Acoustic Waves, *Phys. Rev. X* **5**, 031031 (2015).
- [15] A. Bienfait, K. J. Satzinger, Y. P. Zhong, H.-S. Chang, M.-H. Chou, C. R. Conner, E. Dumur, J. Grebel, G. A. Peairs, R. G. Povey, and A. N. Cleland, Phonon-mediated quantum state transfer and remote qubit entanglement, *Science* **364**, 368 (2019).
- [16] D. A. Golter, T. Oo, M. Amezcua, I. Lekavicius, K. A. Stewart, and H. Wang, Coupling a surface acoustic wave to an electron spin in diamond via a dark state, *Phys. Rev. X* **6**, 041060 (2016).
- [17] S. Hermelin, S. Takada, M. Yamamoto, S. Tarucha, A. D. Wieck, L. Saminadayar, C. Bäuerle, and T. Meunier, Electrons surfing on a sound wave as a platform for quantum optics with flying electrons, *Nature* **477**, 435 (2011).
- [18] R. P. G. McNeil, M. Kataoka, C. J. B. Ford, C. H. W. Barnes, D. Anderson, G. A. C. Jones, I. Farrer, and D. A. Ritchie, On-demand single-electron transfer between distant quantum dots, *Nature* **477**, 439 (2011).
- [19] M. C. Kuzyk and H. Wang, Scaling phononic quantum networks of solid-state spins with closed mechanical subsystems, *Phys. Rev. X* **8**, 041027 (2018).
- [20] Y. Chu and S. Gröblacher, A perspective on hybrid quantum opto- and electromechanical systems, *Appl. Phys. Lett.* **117**, 150503 (2020).
- [21] M. V. Gustafsson, P. V. Santos, G. Johansson, and P. Delsing, Local probing of propagating acoustic waves in a gigahertz echo chamber, *Nature Phys.* **8**, 338 (2012).
- [22] M. V. Gustafsson, T. Aref, A. F. Kockum, M. K. Ekström, G. Johansson, and P. Delsing, Propagating phonons coupled to an artificial atom, *Science* **346**, 207 (2014).
- [23] R. N. Patel, Z. Wang, W. Jiang, C. J. Sarabalis, J. T. Hill, and A. H. Safavi-Naeini, Single-mode phononic wire, *Phys. Rev. Lett.* **121**, 040501 (2018).
- [24] K. Fang, M. H. Matheny, X. Luan, and O. Painter, Optical transduction and routing of microwave phonons in cavity-optomechanical circuits, *Nature Photon.* **10**, 489 (2016).
- [25] P. Farrera, G. Heinze, and H. De Riedmatten, Entanglement between a Photonic Time-Bin Qubit and a Collective Atomic Spin Excitation, *Phys. Rev. Lett.* **120**, 100501 (2018).
- [26] J. Chan, A. H. Safavi-Naeini, J. T. Hill, S. Meenehan, and O. Painter, Optimized optomechanical crystal cavity with acoustic radiation shield, *Appl. Phys. Lett.* **101**, 081115 (2012).
- [27] S. Hong, R. Riedinger, I. Marinković, A. Wallucks, S. G. Hofer, R. A. Norte, M. Aspelmeyer, and S. Gröblacher, Hanbury Brown and Twiss interferometry of single phonons from an optomechanical resonator, *Science* **358**, 203 (2017).

- [28] L. Qiu, I. Shomroni, P. Seidler, and T. J. Kippenberg, Laser cooling of a nanomechanical oscillator to its zero-point energy, *Phys. Rev. Lett.* **124**, 173601 (2020).
- [29] R. Riedinger, S. Hong, R. A. Norte, J. A. Slater, J. Shang, A. G. Krause, V. Anant, M. Aspelmeyer, and S. Gröblacher, Non-classical correlations between single photons and phonons from a mechanical oscillator, *Nature* **530**, 313 (2016).
- [30] S. Weis, R. Rivière, S. Deléglise, E. Gavartin, O. Arcizet, A. Schliesser, and T. J. Kippenberg, Optomechanically Induced Transparency, *Science* **330**, 1520 (2010).
- [31] S. M. Meenehan, J. D. Cohen, S. Gröblacher, J. T. Hill, A. H. Safavi-Naeini, M. Aspelmeyer, and O. Painter, Silicon optomechanical crystal resonator at millikelvin temperatures, *Phys. Rev. A* **90**, 011803 (2014).
- [32] X.-L. Pang, A.-L. Yang, J.-P. Dou, H. Li, C.-N. Zhang, E. Poem, D. J. Saunders, H. Tang, J. Nunn, I. A. Walmsley, and X.-M. Jin, A hybrid quantum memory-enabled network at room temperature, *Sci. Adv.* **6**, eaax1425 (2020).
- [33] M. Borselli, T. J. Johnson, and O. Painter, Measuring the role of surface chemistry in silicon microphotronics, *Appl. Phys. Lett.* **88**, 131114 (2006).
- [34] S. Gröblacher, J. T. Hill, A. H. Safavi-Naeini, J. Chan, and O. Painter, Highly efficient coupling from an optical fiber to a nanoscale silicon optomechanical cavity, *Appl. Phys. Lett.*, **103**, 181104 (2013).
- [35] A. Lebreton, I. Abram, N. Takemura, M. Kuwata-Gonokami, I. Robert-Philip, and A. Beveratos, Stochastically sustained population oscillations in high- β nanolasers, *New J. Phys.* **15**, 033039 (2013).

Non-Classical Mechanical States Guided in a Phononic Crystal

Amirparsa Zivari, Robert Stockill, Niccolò Fiaschi, Simon Gröblacher
 Kavli Institute of Nanoscience, Department of Quantum Nanoscience, TU Delft

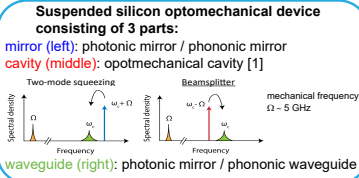


our group
 *GLAB



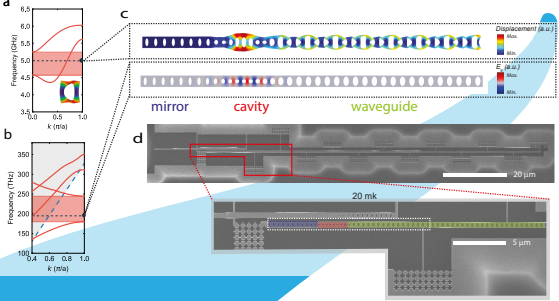
2

Here we demonstrate the first step towards quantum-level control of mechanical excitations and realize a single-mode waveguide for individual phonons in a suspended silicon micro-structure. We use a cavity-waveguide architecture, where the cavity is used as a source and detector for the mechanical excitations, while the waveguide has a free standing end in order to reflect the phonons. This enables us to observe multiple round-trips of the phonons between the source and the reflector. The long mechanical lifetime of almost 100 μ s demonstrates the possibility of nearly lossless transmission of single phonons over, in principle, tens of centimeters.

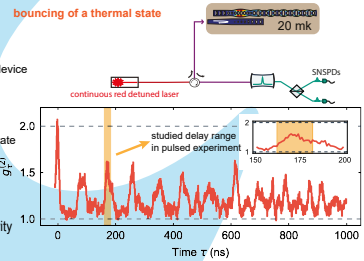
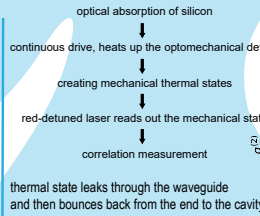
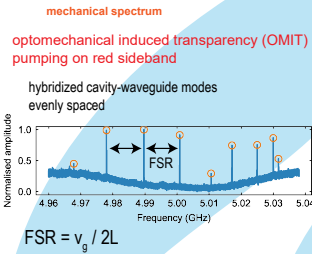


- a) mechanical band structure of the waveguide
- b) optical band structure of the waveguide
- c) mechanical (up) and optical (bottom) simulation - mechanical mode extends over the waveguide
- d) SEM of the device

waveguide has a free-standing end, which acts as mirror for phonons. Phonons reflect back from the end of the waveguide and **BOUNCE** back and forth to the cavity.

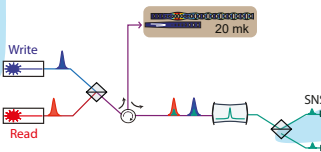


Mechanical Characterization

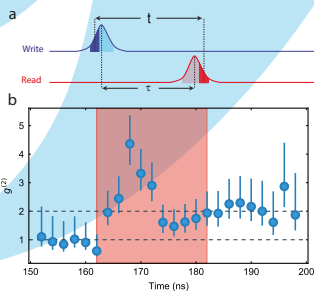


Pulsed experiment:

- blue pulse excites a single phonon - detecting a photon on the blue pulse, heralds the mechanical state to a single phonon
- red pulse reads the mechanical state after a delay - the delay is set around the second bounce
- correlate different parts of the pulses in time (varying delay)



Non-Classicality



Cross correlation of more than 2 is a signature of **non-classicality** [2]

1. Wallucks, Andreas, et al. "A quantum memory at telecom wavelengths." Nature Physics 16.7 (2020): 772-777.

2. Riedinger, Ralf, et al. "Non-classical correlations between single photons and phonons from a mechanical oscillator." Nature 530.7590 (2016): 313-316.



Poster for the paper Amirparsa Zivari, Robert Stockill, Niccolò Fiaschi, and Simon Gröblacher, *Non-classical mechanical states guided in a phononic waveguide*, Nature Physics Vol 18, 789–793 (2022).

3

ON-CHIP DISTRIBUTION OF QUANTUM INFORMATION USING TRAVELING PHONONS

"Over thinking, over analyzing separates the body from the mind"

[Tool - Lateralus]

Amirparsa ZIVARI*, **Niccolò FIASCHI***, **Roel BURGWAL**,
Ewold VERHAGEN, **Robert STOCKILL**, **Simon GRÖBLACHER**

Distributing quantum entanglement on a chip is a crucial step towards realizing scalable quantum processors. Traveling phonons – quantized guided mechanical wavepackets – can be used as a medium to transmit quantum states, due to their small size and low propagation speed compared to other carriers, such as electrons or photons. Moreover, phonons are highly promising candidates to connect heterogeneous quantum systems on a chip, such as microwave and optical photons for long-distance transmission of quantum states via optical fibers. Here, we experimentally demonstrate the distribution of quantum information using phonons, entangling two traveling phonons and creating a time-bin encoded traveling phononic qubit. The mechanical quantum state is generated in an optomechanical cavity and propagates into a phononic waveguide for around 200 micrometers. We further prove that the entangled phonon-photon pair can be used to violate a Bell-type inequality.

This work is published in Science Advances: Amirparsa Zivari*, Niccolò Fiaschi*, Roel Burgwal, Ewold Verhagen, Robert Stockill, and Simon Gröblacher, *On-chip distribution of quantum information using traveling phonons*, Science Advances Vol 8, Issue 46 (2022).

* indicates equal contribution

3.1. INTRODUCTION

OVER the past decades, quantum technologies have evolved from scientific proof-of-principle experiments to a nascent and thriving industry. With recent demonstrations of quantum advantage over classical computation in multiple systems [1, 2], the need for connecting such resources is becoming ever more urgent. Distributing quantum entanglement between distant parties is a crucial step towards implementing quantum repeaters and networks [3, 4]. Distributing it on-chip is needed for sparse qubit array architectures, which require on-chip long-range qubit couplers [5]. Additionally, having entanglement between a stationary quantum memory and a flying qubit plays a central role in low-loss quantum information transfer over long distances [3].

One of the key challenges of building a quantum network is forming interfaces between heterogeneous quantum devices. A highly versatile system for this task has been identified in phonons, which can act as efficient intermediaries between different resources [6]. In particular, phonons have been shown to be highly useful in converting states between different optical wavelengths [7], as well as for microwave to optics frequency conversion [8–14]. Most recently, such a mechanical transducer has been used to transfer signals from a superconducting qubit to an optical fiber [15], a key step for quantum information transfer. Moreover, the potential for quantum gate operations using phonons has been shown [16–18], owing to long coherence times and high transfer fidelities of phonons. The interest in traveling phonons in fact goes well beyond enabling long-distance quantum networks. Several of the most exciting prospects are arising from their many orders of magnitude slower propagation speed compared to light, low loss transmission and their small mode volume compared to traveling GHz photons. These unique features could have the potential to enable the on-chip distribution and processing of quantum information in a highly compact fashion [19], allow for coherent interactions with a large variety of quantum systems such as defect centers [20], superconducting qubits [21] and quantum dots [22, 23], in both homogeneous or heterogeneous implementations [24]. Demonstrating the basic building blocks, such as marking the distribution of quantum information using highly confined phonons, remains an open challenge to date.

Quantum optomechanics has proven to be a versatile toolbox for controlling stationary, strongly confined phonons [25, 26]. Previously, bulk and surface acoustic waves (BAWs and SAWs, respectively) have been shown to be able to operate in the quantum regime [17, 19], for example, by coupling to superconducting qubits for transducer and quantum information applications [27, 28], as well as entangling acoustic phonons [29]. These systems benefit from deterministic quantum operations with high fidelities, enabled by the non-linearity of the superconducting qubit and strong coupling between the qubit and the phononic channel. However, the confinement of the phonons in optomechanical devices results in several advantages, such as stronger field coupling [30], higher coherence and longer lifetime [31], and long distance routing capability on chip [32, 33]. In this work, building on these recent developments, we experimentally distribute quantum information using phonons in a waveguide. Our device is composed of an optomechanical cavity, which acts as the single phonon source and detector, that is connected to a single-mode phononic waveguide. Using this device we then create a time-bin entangled state of a pair of traveling phonons. Furthermore, we unambigu-

ously show the non-classical correlations between an optical and the traveling phononic qubit, by violating a Bell-type inequality [34–36].

3.2. METHODS

3.2.1. DEVICE DESIGN

Our device consists of a single mode optomechanical cavity connected to a phononic waveguide (cf. Fig. 3.1a), similar to a previous design [33]. The cavity is used as a source and detector for mechanical excitations, controlled with telecom-wavelength optical pulses (via Stokes and anti-Stokes scattering [37]). We engineer the photonic and phononic band structure of the different parts of the device such that the mechanical mode extends into the waveguide while the optical mode remains fully confined in the cavity (see the Supplementary Information (SI) for more details on the device design). The waveguide has a free standing end, which acts as mirror for the traveling phonons and effectively forms a Fabry-Pérot cavity. The coupling between the single mode cavity and this Fabry-Pérot cavity results in a hybridization of the cavity and waveguide modes into (almost) evenly spaced modes separated by the free spectral range (FSR) of the Fabry-Pérot cavity. The FSR is determined by the length of the waveguide and by the group velocity of the phonons. We design the waveguide to be single mode for the symmetry of the mechanical mode used in this work (the band structure is shown in Fig. 3.1b).

3.2.2. THEORETICAL STUDIES OF TIME-BIN ENTANGLEMENT PROTOCOL

In order to create a propagating mechanical excitation we use a blue-detuned write (Stokes) control pulse, which via a two-mode squeezing interaction, creates entangled photon-phonon pairs. The phononic excitation created in the cavity then leaks into the waveguide, is reflected by the end mirror and returns back periodically to the cavity after a round-trip time τ . Finally, to retrieve the mechanical state, a red-detuned read (anti-Stokes) control pulse enables the optomechanical beam-splitter interaction which maps the mechanical into a photonic excitation (see Fig. 3.1c for details on the scheme). To create a time-bin encoded mechanical qubit using this scheme, we first place the device in a dilution refrigerator at 10 mK, initializing the mechanical mode in its quantum ground state. We then send two blue-detuned write pulses separated by $\tau/2$ to the device in the cryostat, as shown in Fig. 3.1d, and send the resulting scattered photons into an optical interferometer. One arm is delayed with respect to the other one by $\tau/2$ to overlap the scattered photons in time. The reflected control pulses are suppressed using optical filters (see SI) and the resulting interferometer output signals are detected on two superconducting nanowire single-photon detectors (SNSPDs). By operating in the low pulse energy regime (low optomechanical scattering probabilities, p_w), the two identical write pulses create the optomechanical state

$$|\psi_0\rangle \propto |0000\rangle + \sqrt{p_w}(|1010\rangle_{E_o L_o E_m L_m} + e^{i\phi_w} |0101\rangle_{E_o L_o E_m L_m}) + \mathcal{O}(p_w), \quad (3.1)$$

where E_m (L_m) and E_o (L_o) indicate the “Early” (“Late”) mechanical and optical state, and ϕ_w is the phase difference between the two “Early” and “Late” write pulses, set with an electro-optical modulator (EOM) (see SI section 4 for more details). By overlapping

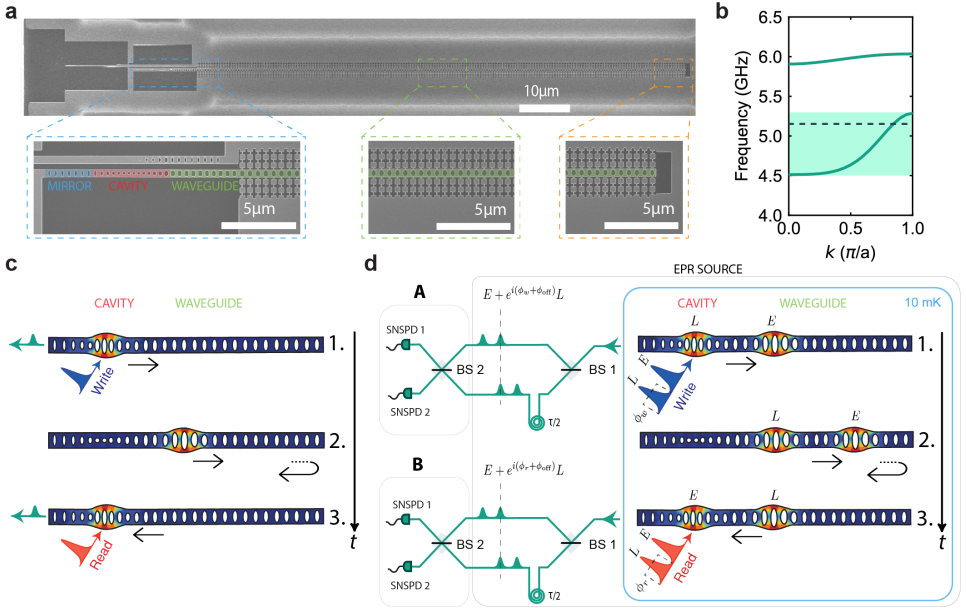


Figure 3.1: Device and experimental setup. a) Scanning electron microscope (SEM) image of the device. Bottom left: photonic and phononic mirror (highlighted in blue), optomechanical cavity (red) and initial part of the phononic waveguide, which also acts as a photonic mirror (green). Bottom center: section of the phononic waveguide. Bottom right: free standing end of the waveguide, which acts as a mirror for the phonons. b) Band diagram of a unit cell of the waveguide showing its single mode design for the symmetric mode, with the frequency of interest depicted by the black dashed line (see the SI section 1). c) The control pulses (write and read) are sent to the cavity to create 1. and retrieve 3. the mechanical excitation. The green pulses depict the scattered Stokes and anti-Stokes photons. In 2. the mechanical excitation travels in the waveguide (round-trip time of τ). d) Simplified schematics of the time-bin entangling protocol. 1. Creation of the entangled state between the Early (E) and Late (L) Stokes-scattered photons and the traveling phononic excitation in the waveguide. The pulses have a time delay of $\tau/2$ and are depicted here in shorter succession than in the experiment for clarity of the drawing. 2. Propagation of the mechanical qubit in the waveguide, with the reflection at the end. 3. Mapping of the phononic onto a photonic state in order to verify the entanglement. The boxes conceptually divide Einstein–Podolsky–Rosen (EPR) source, and measurements setups A and B (which are the same experimental setup at different times t), used to create and detect the entangled state. SNSPDs are superconducting nanowire single-photon detectors. The arrows in c) and d) represent the direction of propagation of the mechanical excitations and the time axis is shown by the vertical black arrow.

these “Early” and “Late” photons on a beamsplitter, after passing through the unbalanced interferometer, we erase any “which path” information. Consequently, by detecting a Stokes-scattered photon from the overlapped “Early” and “Late” pulses on one of the detectors, we perform an entanglement swapping operation resulting in an heralded entangled state between the “Early” and “Late” traveling mechanical excitations

$$|\psi_m\rangle \propto |10\rangle_{E_m L_m} \pm e^{i(\phi_w + \phi_{\text{off}})} |01\rangle_{E_m L_m}, \quad (3.2)$$

with the plus (minus) sign resulting from a detection event in either detector. The phase ϕ_{off} is a fixed phase difference between the two arms of the unbalanced interferometer (SI sections 5 and 6). Note how the state is maximally entangled in the Fock-basis, which

at the same time serves as a mechanical qubit.

The entangled phonon state travels through the waveguide and after re-entering the cavity can be mapped onto an optical state with the red-detuned anti-Stokes control pulses. The entire 4-mode optical state of write and read scattered photons can be expressed as:

$$|\psi_{AB}\rangle \propto [(1 + e^{i(\phi_w + \phi_r + 2\phi_{\text{off}})})(\hat{a}_{w,1}^\dagger \hat{a}_{r,1}^\dagger - \hat{a}_{w,2}^\dagger \hat{a}_{r,2}^\dagger) + i(1 - e^{i(\phi_w + \phi_r + 2\phi_{\text{off}})})(\hat{a}_{w,2}^\dagger \hat{a}_{r,1}^\dagger + \hat{a}_{w,1}^\dagger \hat{a}_{r,2}^\dagger)] |0000\rangle \quad (3.3)$$

where $\hat{a}_{w,1}^\dagger$ ($\hat{a}_{w,2}^\dagger$) and $\hat{a}_{r,1}^\dagger$ ($\hat{a}_{r,2}^\dagger$) are the creation operators of the photon coming from the write pulse and read pulse, on detector 1 (2). An additional phase ϕ_r is applied only on the "Late" read pulse, which is used to rotate the readout basis. Here the read pulses map the mechanical state onto the optical mode and hence this state is a direct result of the entanglement between the photonic and the traveling phononic qubit. For verifying the mechanical entanglement of Eq. 3.2 we use $\phi_r = 0$.

In order for our protocol to work, we need to fulfill several basic requirements. For both the phononic and photonic qubits, for example, we have to create orthogonal states (the basis), and thus for the time-bin encoding we have to be able to unambiguously distinguish the "Early" and "Late" states. Experimentally we implement this by realizing a $\sim 100 \mu\text{m}$ long phononic waveguide and by choosing the control pulse length as 30 ns, given a simulated group velocity in the waveguide of approx. 2000 m/s. Moreover the thermal occupation of the mechanical mode, mainly given by a small absorption of the control pulses in the optomechanical cavity, has to be $\ll 1$ in order to realize a high-fidelity entangled state. This limits the maximum scattering probability of the write and read control pulses (see SI section 3).

3.3. RESULTS

3.3.1. BASIC AND CLASSICAL CHARACTERIZATIONS

To characterize the device we first measure its optical properties at 10 mK and observe a resonance at $\lambda \approx 1556.06 \text{ nm}$ with FWHM of $\kappa/2\pi \approx 1.05 \text{ GHz}$ (intrinsic loss rate $\kappa_i/2\pi = 250 \text{ MHz}$, see Fig. 3.2a). We use the optomechanically induced transparency (OMIT) technique to measure the mechanical spectrum of the device [33, 38]. As can be seen in Fig. 3.2b, the hybridized modes exhibit a clean, evenly spaced spectrum with FSR $\approx 8 \text{ MHz}$. We choose the most prominent mechanical resonance in Fig. 3.2b (around 5.154 GHz) as the frequency to which we detune the lasers with respect to the optical resonance in order to address Stokes and anti-Stokes interactions. We further use the rate of Stokes-scattered photons from a 30 ns long pulse to determine the equivalent single photon optomechanical coupling rate [39] of the ensemble of optomechanically coupled modes at $g_0/2\pi \approx 380 \text{ kHz}$.

In order to measure the round-trip time and coupling between the cavity and waveguide we pump our device with a continuous red-detuned laser. Due to the non-zero optical absorption in the device, the continuous laser creates a thermal mechanical population inside the optomechanical device that leaks into the phononic waveguide and reflects from the free standing end before returning back into the optomechanical cavity. The same red-detuned laser then maps the mechanical state onto a photonic state

and we measure the two-photon detection coincidence with varying delays between two events. This measurement allows us to obtain the intensity correlation $g_{\tau}^{(2)}$ of the mechanical thermal state in the optomechanical cavity, as can be seen in Fig. 3.2c. The coincidence rate is normalized to the single photon click rates. For zero time delay we find a $g_{\tau=0}^{(2)} \approx 2$, as expected for a thermal state. The correlation drops down to 1, as the thermal state leaves the optomechanical cavity into the waveguide resulting in uncorrelated clicks, and then periodically increases again when the thermal population returns back to the cavity [33]. We use this measurement to determine the round-trip time for an excitation in the waveguide, $\tau = 126$ ns.

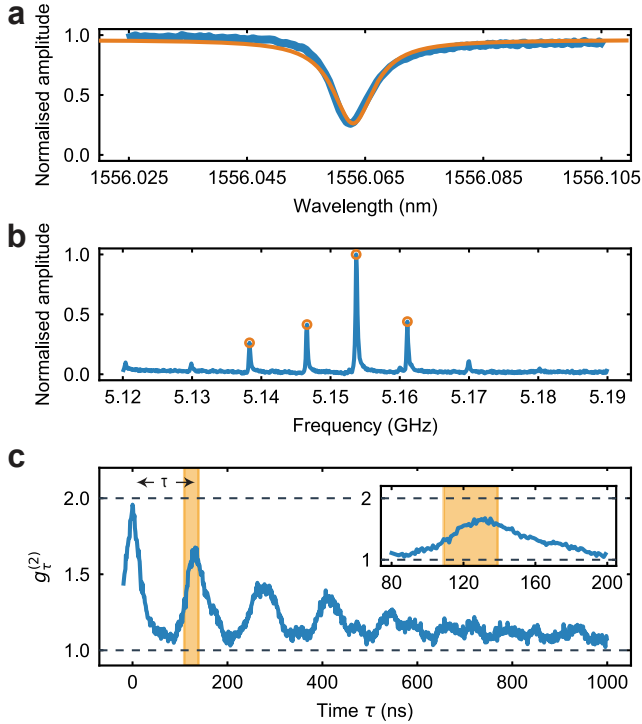


Figure 3.2: **Initial characterization.** a) Optical spectrum of the device measured in reflection. b) Mechanical spectrum measured using optomechanically induced transparency (OMIT). c) Second order correlations of a thermal state for different time delays between the SNSPDs click events τ . The series of equally spaced peaks shows that when the thermal mechanical excitations leave the optomechanical cavity, they are reflected from the end of the waveguide and then return back into the cavity. The inset is a close-up of the area around the first peak. The shaded regions show the delay and control pulse area chosen for all the subsequent experiments in this work ($\tau = 126$ ns, with a time length of 30 ns).

Note that the decay in the peak values is mainly due to the small difference in FSR between the mechanical modes [33], as well as the short mechanical lifetime $T_1 \approx 2.2 \mu\text{s}$ (see section 7 in the SI for more details). From the FWHM of the peak centered around zero time delay in Fig. 3.2c we can extract the packet time duration of ≈ 30 ns. To match

the packet time length, we then choose to use 30 ns-long Gaussian write and read pulses in all experiments.

3.3.2. TIME-BIN PHONONIC ENTANGLEMENT

As a next step we verify our ability to distinguish between multiple phonon wavepackets. To do this, we measure the photon cross-correlations in a double write / read pulse sequence, in which we create and measure the second wavepacket after half of the round trip time $\tau/2 \approx 63$ ns. In this experiment, the delay arm of the interferometer is disconnected, such that the pulses do not interfere. Two write and two read pulses are sent to the device with a relative delay between them of $\tau/2$, as shown in Fig. 3.3a. In all the pulsed measurement we set a waiting time between trials of $\sim 7 T_1$ (15 μ s) to let the mechanical modes thermalize to the ground state (see SI section 3). The energy of each pulse is 26 fJ (112 fJ) for the write (read), probabilistically scattering photons through the Stokes (anti-Stokes) process, with a probability of $p_w = 0.2\%$ ($p_r = 0.7\%$). The measured thermal phonon number of the mechanical resonator after applying the four pulses are 0.022 ± 0.002 , 0.040 ± 0.003 , 0.066 ± 0.003 and 0.095 ± 0.004 (cf. SI section 3). We measure the second order cross-correlation between the four combinations of “Early” and “Late” write and read pulses, $g_{cc}^{(2)}$ as shown in Fig. 3.3b. We observe strong non-classical correlations of $g_{cc}^{(2)} = 9.4 \pm 1.3$ between “Early”-“Early” and $g_{cc}^{(2)} = 5.0 \pm 0.8$ between “Late”-“Late” combinations, while the other two combinations show only classical correlations of $g_{cc}^{(2)} = 1.5 \pm 0.5$ [40]. Note that the lower value for the “Late”-“Late” combination, with respect to “Early”-“Early”, is caused by the small accumulated thermal population induced by the pulses (see SI section 3 for more information).

We now proceed to verify that we have created a traveling mechanical qubit encoded in a superposition of “Early” and “Late” time bins, by sending the same pulse sequence to the device, with the delay arm of the interferometer connected. This way the part of the “Early” scattered photons that pass through the delay line and the part of the “Late” scattered photons that pass through the direct arm are overlapped in time, such that a single photon detection event after BS2 projects the mechanical state in Eq. 3.2. The pulse sequence at the detectors is shown in Fig. 3.3c, where the highlighted peaks are the overlapped and interfered “Early” and “Late” pulses, from which we detect the photons. We sweep the excitation phase ϕ_w and measure the second order correlation $g^{(2)}$ between the write and read photon detection events occurring at the same (green) or different (orange) output of BS2, displayed in Fig. 3.3d. The periodic dependence on the phase demonstrates the coherence of the generated entangled state. To show that the state shown in Eq. 3.2 is indeed entangled, we use an entanglement witness, denoted by R , designed for optomechanical systems [41], as previously used in [42]. After sufficient integration we gather more than 500 coincidence events and we obtain $R = 0.72 \pm 0.06$, violating the classical threshold of 1 by almost 5 standard deviations.

3.3.3. OPTOMECHANICAL BELL TEST WITH TIME-BIN ENTANGLED PHONONS

To unambiguously demonstrate the non-classical character of the traveling phononic qubit and the photon state in Eq. 3.3, we perform a Bell-type test using the CHSH in-

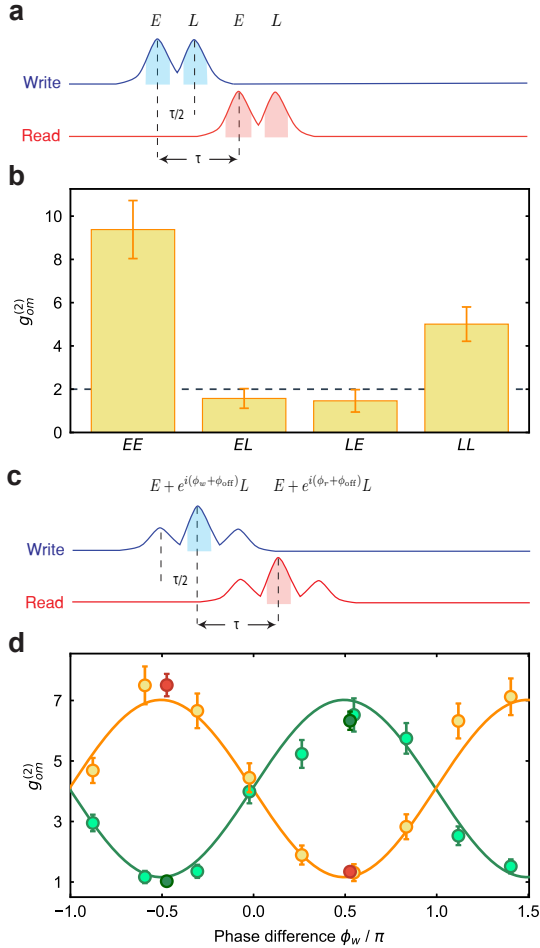


Figure 3.3: **Time-bin phononic entanglement.** a) Pulse scheme for a double write / read pulse cross-correlation measurement. In this experiment the delayed arm of the interferometer is open. The two write and two read pulses are called “Early” (*E*) and “Late” (*L*) and are delayed by $\tau/2$. The shaded areas are the regions from which the coincidences are gathered (time length of 30 ns). b) Extracted values of the cross-correlation $g_{om}^{(2)}$ measured for the four combinations of write / read pulses. The correlations for *EE* and *LL* are significantly exceeding the classical threshold of 2 (dashed line), while the other two combinations of *EL* and *LE* only exhibit classical correlations. c) Control pulse scheme to create and detect time-bin phononic entanglement at the interferometer. The “Early” pulse passing through the delay arm of the interferometer and the “late” pulse passing through the direct arm of the interferometer overlap in time. d) Second-order correlations of the Stokes and anti-Stokes photons as a function of the relative phase difference ϕ_w between the “Early” and “Late” write pulses. The events for same detector coincidences are shown in green, while different detectors coincidences are orange. Two additional measurements, red and dark green points, are performed at two phase settings to obtain more statistics for verifying the phononic entanglement. The maximum violation is $R = 0.72 \pm 0.06$, almost 5 SDs below the classical threshold of 1. All error bars are one SD. The solid curves are the joint fit of the data and serve as guide to the eye.

equality [34]. We define the correlation coefficients

$$E(\phi_w, \phi_r) = \frac{n_{11} + n_{22} - n_{12} - n_{21}}{n_{11} + n_{22} + n_{12} + n_{21}}, \quad (3.4)$$

where n_{kl} are the events where detector k clicked after a write pulse (station A in Fig. 3.1d) and detector l after a read pulse (station B in Fig. 3.1d). The inequality then states that

$$S = |E(\phi_w^0, \phi_r^0) - E(\phi_w^1, \phi_r^0) + E(\phi_w^0, \phi_r^1) + E(\phi_w^1, \phi_r^1)| \leq 2. \quad (3.5)$$

The maximum violation is expected to occur for $(\phi_w^i = \phi_0 + (-1)^{i+j}\pi/4, \phi_r^j = (\pi/2)^j)$, with $i, j = \{0, 1\}$, and where $\phi_0 = 2\phi_{\text{off}} + \pi/2 \approx 1.0\pi$ is the phase for which the correlation coefficient is zero (with negative slope). We choose phase settings with a small offset compared to these values to have the highest possible value of S for our setup (see SI section 6 for more details). To violate the CHSH inequality we lower the energy of the write pulses slightly, such that we use 15 fJ (112 fJ) for the write (read) pulse, with a scattering probability of $p_w = 0.13\%$, ($p_r = 0.7\%$). The measured thermal populations for the four pulses are then 0.027 ± 0.003 , 0.038 ± 0.004 , 0.055 ± 0.002 and 0.090 ± 0.004 (see SI section 3).

From the correlation coefficient we define the visibility as $V = \max(|E|)$. We first perform an additional measurement at the phase of maximum visibility obtaining $V = 0.82 \pm 0.04$, which is considerably higher than the threshold of $V > 1/\sqrt{2} \approx 0.7$ required for violating the CHSH inequality. We then measure at the four optimal phase settings for the Bell test (see Fig. 3.4) obtaining a value of $S = 2.32 \pm 0.08$, which corresponds to a violation of the CHSH inequality by 4 standard deviations. The rate of events for this measurements is around 30 per hour of integration, allowing us to measure the full data set for the violation within 56 hours.

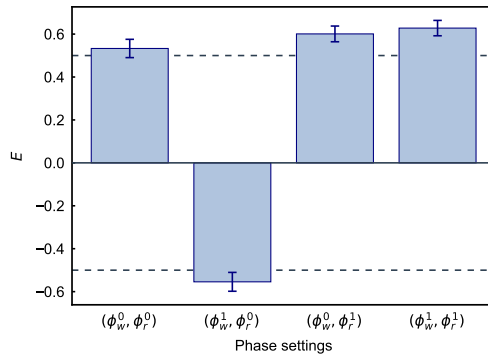


Figure 3.4: **Bell test.** The values of the correlation coefficients E grouped for the four ideal phase settings of the CHSH inequality, which are $(\phi_w^0, \phi_r^0) = (\phi_0 - \pi/4, 0)$, $(\phi_w^1, \phi_r^0) = (\phi_0 + \pi/4, 0)$, $(\phi_w^0, \phi_r^1) = (\phi_0 - \pi/4, \pi/2)$ and $(\phi_w^1, \phi_r^1) = (\phi_0 + \pi/4, \pi/2)$. The total number of events for each phase setting is ~ 400 . The dashed lines are the threshold for each correlation coefficient to violate the inequality. From these values we obtain $S = 2.32 \pm 0.08$, which violates the inequality by 4 SD. All errors are one SD.

3.4. CONCLUSION AND DISCUSSION

We have unambiguously demonstrated a traveling phononic qubit in the form of a time-bin entangled state, which can be used to distribute quantum information on a chip. The routing process is shown to be fully coherent, which is of fundamental importance for routing quantum information and interconnecting quantum devices. While we limit ourselves to show two-mode entanglement, the same device can be used with up to four modes, given the round-trip time and mechanical packet length, or more by using a longer waveguide. Additionally, the quantum state can be retrieved at arbitrary multiples of the round trip time, allowing for long storage and controlled emission of the state. Moreover, as the phononic entangled state travels down the waveguide, a straightforward extension using our device will allow to distribute quantum entanglement to different points on a chip. We have chosen to use a waveguide design with a lifetime of only $T_1 \approx 2.2 \mu\text{s}$, limiting the maximal phonon traveling length for this devices to around 3 mm. By adding additional phononic shielding, this can however easily be extended to meter scales as the device's lifetime increases to several milliseconds [31].

The demonstrated time-bin entanglement between a photonic and a traveling phononic qubit, verifying their non-classical correlations by violating a CHSH inequality, underlines the suitability of the phononic system as a DLCZ unit cell [43]. In this work, the fidelity of the entangled state is limited by residual optical absorption, which can be further reduced by up to an order of magnitude through optimized fabrication, allowing for state retrieval efficiencies of up to 30 % [40].

The ability to excite, guide, and detect traveling phonons is the basic toolbox for phonon manipulation on-chip, enabling a completely new field using traveling mechanical modes in the quantum regime. Together with a phononic phase modulator [44] and beamsplitter, this work will lead to full coherent control of guided phonons and paves the way to novel quantum acoustic experiments. Moreover, our measurements highlight the potential of phonons as ideal candidates for realizing quantum networks and repeaters, as well as for on-chip distribution of quantum information in hybrid quantum devices, for example for interfacing microwave superconducting circuits with spin quantum memories [24] or to couple on-chip qubits using electron-phonon interaction in solids [22].

Acknowledgments We would like to thank Matteo Lodde, Andrea Fiore and Bas Hensen for valuable discussions. We further acknowledge assistance from the Kavli Nanolab Delft. This work is financially supported by the European Research Council (ERC CoG Q-ECHOS, 101001005) and is part of the research program of the Netherlands Organization for Scientific Research (NWO), supported by the NWO Frontiers of Nanoscience program, as well as through Vidi (680-47-541/994) and Vrij Programma (680-92-18-04) grants. R.S. acknowledges funding from the European Union under a Marie Skłodowska-Curie COFUND fellowship.

Conflict of interests: The authors declare no competing interests.

Author contributions: A.Z., R.S. and S.G. devised and planned the experiment. A.Z., N.F, R.B. simulated and designed the device. N.F fabricated the sample, A.Z. and N.F. built the setup and performed the measurements. A.Z., N.F, R.S. and S.G. analyzed the data and wrote the manuscript with input from all authors. E.V. and S.G. supervised the project.

Data Availability: Source data for the plots are available on [Zenodo](#).

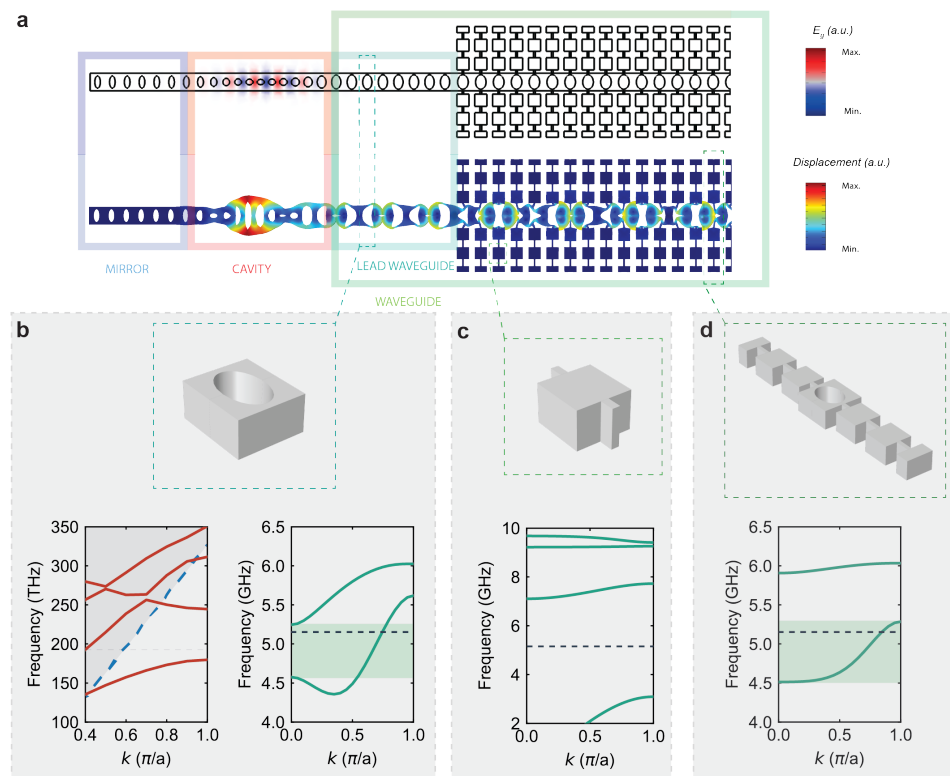


Figure 3.5: a) Optical (top) and mechanical (bottom) eigenmode simulations of the full structure. The mechanical mode shown is a cavity-waveguide supermode. Note how the optical mode is confined in the cavity, while the mechanical mode is extended into the waveguide. b) Lead waveguide unit cell, with its optical (left) and mechanical (right) band diagram shown below. The gray area for the optical part depicts the light cone, delimited by the blue dashed line. c) Shield unit cell, used in the clamps to connect the waveguide to the substrate and its mechanical band diagram below. d) Unit cell of the shield-clamped waveguide, with its band structure shown underneath. In all plots the horizontal black dashed lines are the working optical and mechanical frequencies, while the highlighted areas are the single mode regions of the waveguides.

3.5. SUPPLEMENTARY INFORMATION

DESIGN

Our device, which is shown in Fig. 3.1a, is composed of three distinct parts: a mirror, a cavity and a waveguide. To design the device we use finite element simulations (COMSOL) and engineer a suspended silicon nanobeam (width 529 nm and thickness of 250 nm) with elliptical holes patterned into it. The hole dimensions are varied along the beam in order to realize the different parts of our device. The finite element simulation of the full structure is shown in Fig. 3.5a. The left part (blue) is a phononic and photonic mirror, with the respective bandgaps at the resonance frequencies of the cavity. The optomechanical cavity, acting as the source and detector for phonons, has a co-localized single optical mode in the telecom band and a single mechanical mode around 5 GHz, similar

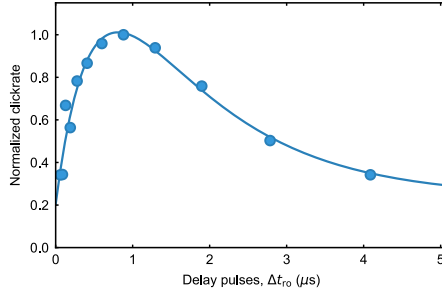


Figure 3.6: Normalized clickrates from the probe pulse that gives an uncalibrated measure of the thermal population in time. The delay between pump and probe pulse is Δt_{ro} . We extract $T_1 \approx 2.2\mu\text{s}$, by fitting the data (solid curve).

to [37, 45]. The phononic waveguide (green) is a single mode phononic waveguide for the symmetric mechanical breathing mode in the frequency range of interest (around 5 GHz). Only this mode is considered, as it matches the mechanical mode shape of the cavity, enabling large mechanical coupling between the cavity and the waveguide. The first part of the waveguide, referred to as the “lead waveguide” in the figure, acts as a photonic mirror having a bandgap in the telecom range. The unit cell of this part, together with its optical and mechanical band structure, are shown in Fig. 3.5b and c, respectively. As a result of our design, the optical mode stays confined inside the optomechanical cavity, while the mechanical mode is guided with very little loss through the waveguide, as shown in Fig. 3.5a. The second part of the waveguide is connected to the substrate via phononic shield clamps for structural support. The band diagram of the phononic shield together with the unit cell are shown in Fig. 3.5d and e. The shield minimizes the mechanical loss from the waveguide to the substrate, fully confining the mechanical mode in the waveguide. The design of the waveguide with clamping differs from the lead waveguide to avoid perturbations of its band structure. The unit cell shape of this waveguide and the band structure are shown in Fig. 3.5f and g. Note how the mode in the waveguide has an approximately linear dispersion in the range of interest.

MECHANICAL LIFETIME

To measure the mechanical lifetime of the device (T_1) we send a series of red-detuned double pulses with the interferometer delay arm open. The strong first pulse creates, via optical absorption, a relatively large thermal population that is probed by the second pulse, and which is delayed by time Δt_{ro} . With this pump-probe experiment we can access the uncalibrated thermal population of the device in time [40] (see Fig. 3.6). From the exponential decay we measure $T_1 \approx 2.2\mu\text{s}$, much longer than the 126 ns delay used in the experiments. We set the time between trials in all experiments equal to $15\mu\text{s}$, to let the population fully decay. Note that while the device is intentionally designed to have a short lifetime in order to allow for a high repetition rate of the experiment, previous work with similar structures has reported lifetime up to 5.5 ms [33]. We would also like to note that an additional phononic shield period at the mirror side (blue part in Fig. 3.1a) does

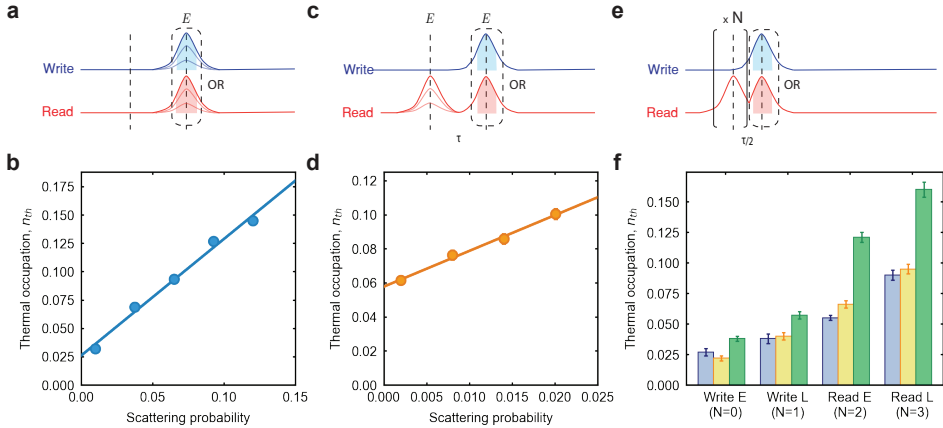


Figure 3.7: a) Pulse scheme for the thermal occupation measurement. We send trains of pulses alternating between write and read to measure the asymmetry in their scattering probabilities. The opaque pulses represents the sweep in energy of the pulse, while the shaded area is the integration region. b) Thermal occupation as a function of the measured scattering probability for a single pulse (equivalent to the read “Early” situation in the experiments). The solid line is a linear fit to the data. c) Same as a) for the two pulse calibration of the thermal occupation. Note how the read pre-pulse is only for heating the mechanical mode and its energy is swept. The alternating pulses used to measure the n_{th} are in the black dashed box and have fixed energy. d) Thermal occupation of the second pulse (read “Early” in the experiment) as a function of the measured scattering probability of the first pulse (write “Early” in the experiment). Note how the offset in this measurement strongly depends on the energy of the second pulse, which in this case is 225 fJ (twice the energy of the single read pulses used in the phononic entanglement experiment of Fig. 3.3 in the main text). The solid line is a linear fit to the data. e) Same as a) but for multiple pre-pulses. We send N pre-pulses (with $N = (0, 1, 2, 3)$ for write E, write L, read E and read L, respectively) and use the alternating pulses in the dashed black box to measure the thermal population. Each pulse has the energy used in the experiments. f) Measured thermal occupation for the four pulses used in the experiments. In blue for the scattering probabilities used in the measurements for the additional phononic entanglement data and Bell test (Fig. 3.4 in the main text), in orange for the double pulse cross correlation and the phononic entanglement with the sweep in ϕ_w (Fig. 3.3 in the main text) and in green for the phase calibration (section 3.5). All error bars are one standard deviation.

not increase the lifetime any further. The increase in thermal population for short delays ($\Delta t_{ro} < 1 \mu\text{s}$) is given by the delayed absorption [37].

THERMAL OCCUPANCY OF THE MECHANICAL MODE

In order to determine the thermal occupation of the mode of interest we send trains of alternating write and read pulses to the device, as shown in Fig. 3.7a. From the asymmetry in clickrates of these pulses we can calculate the thermal mechanical population n_{th} . We adjust the scattering probability by sweeping the energy of the pulses and measure the resulting thermal occupation, see Fig. 3.7b. To further mimic the same heating conditions as in the experiment, without the optomechanically excited coherent population created from the write pulses, we use heating pre-pulses from the read laser. The alternating pulses, used to measure n_{th} , are sent at a delay given by the round-trip time τ and have a fixed energy, while the energy of the pre-pulse is swept. In Fig. 3.7 we show the pulse scheme for these measurements, as well as the thermal occupation at the second pulse (in the experiment the read pulse) as a function of the scattering probability of the

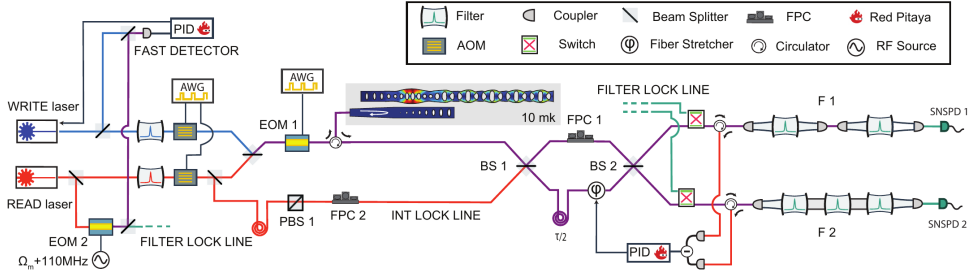


Figure 3.8: Detailed scheme of the setup (see text for more details). AOM are the acousto-optic modulators, AWG the arbitrary waveform generators, EOM the electro-optic modulator, VOA the variable optical attenuator, BS the beamsplitters, and PBS the polarizing BS, FPC the fiber polarization controller and SNSPD the superconducting nanowire single-photon detectors. Ω_m the mechanical frequency. All the components (apart from the free-space filters F 1 and F 2) are fiber based.

first pulse (in the experiment the write pulse). We use the two asymmetry measurements (Fig. 3.7b and d) to choose the single write/read scattering probabilities that will give a total thermal population below 0.1, with a third of this thermal occupation given by the first pulse and the rest by the second (to minimize the effects of delayed heating).

We then measure the values of n_{th} for the pulses used in the experiments. We send heating pre-pulses and use the alternating pulses to measure the thermal population, as drawn in Fig. 3.7e. Each of these pulses has the corresponding energy used in the experiments and all are delayed by $\tau/2$ with respect to each other. In Fig. 3.7f we report the measured thermal occupation for the four pulses of the experiments, for the three sets of scattering probabilities used: in blue the one for the additional phononic entanglement data and the Bell test (Fig. 3.4 in the main text), in orange for the double pulse cross correlation and the phononic entanglement with the sweep in ϕ_w (Fig. 3.3 in the main text) and in green for the phase calibration (section 3.5). Note how the thermal population increases non-linearly with increasing number of pulses due to delayed heating, as is clearly visible in Fig. 3.7.

EXPERIMENTAL SETUP

A sketch of the experimental setup is shown in Fig. 3.8. Two continuous-wave (CW) lasers (write and read) are frequency-locked to one another by detecting the interference between their light on a fast detector (in particular: the light from the write laser and the second order sideband of the read laser generated by EOM 2, which have a frequency difference of 2×110 MHz). The laser light from the CW lasers is filtered to remove GHz noise using fiber filters. The pulses are created by gating the CW light with 110 MHz AOMs, which are driven by an arbitrary waveform generator and the laser pulses are combined on a beam splitter. A phase EOM, driven by another AWG, is used to add a phase offset to the "Late" pulses (to set ϕ_r and ϕ_w). The pulses are then routed to a circulator and to the cryostat, where a lensed fiber allows the coupling to the device's optical waveguide, with efficiency of $\eta_c \approx 50\%$. The light from the device is fed to an unbalanced Mach-Zehnder interferometer, defined by BS 1 and BS 2, where the time delay between the arms is $\tau/2 = 63$ ns. These two BSs have a relative difference in the splitting ratio

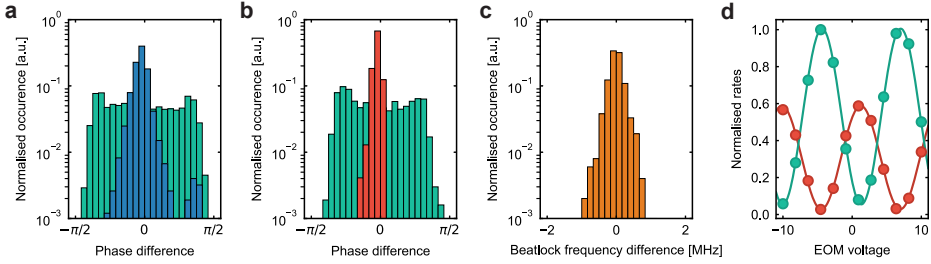


Figure 3.9: a) Occurrence histogram of the phase difference acquired by the write pulses when the interferometer is locked (in blue) and unlocked (in green). The FWHM is $\approx \pi/7$. b) Same as a) for the read pulses, for the case of a locked interferometer (in red) and unlocked (in green). The FWHM here is $\approx \pi/20$. c) Occurrence histogram of the frequency difference of the write and read lasers as from the beatlock. Here the FWHM is ≈ 0.5 MHz. This relative frequency jitter causes a bigger phase difference spread for the write pulses compared to the read ones. d) Normalized count rates of SNSPD1 (red) and SNSPD2 (green) for weak coherent pulses on resonance with the filter cavities. Sweeping the EOM voltage results in the observed interference pattern, which we use to calibrate the phase given by the EOM. In this case the interferometer visibility is $V_{\text{int}} \approx 94\%$. Error bars are one standard deviation and are too small to be seen.

of the two output ports smaller than 0.5%, while the losses in both lines are negligible. The interferometer is actively stabilized using a home-built fiber stretcher controlled by a PID loop that uses the signal from pulses coming from the INT LOCK LINE (see section 3.5 for more details). The polarization of the two arms are matched at BS 3 using the fiber polarization controller 1 (FPC 1). The light from the interferometer is filtered by two sets of free space optical Fabry-Pérot cavities (F 1 and F 2) with suppression ratios of the strong control pulses of about 115 dB (F 1) and 112 dB (F 2). This gives a pump pulse leakage rate of 2×10^{-7} and 4×10^{-7} photons per repetition from the write pulse and 1.4×10^{-6} and 2.6×10^{-6} from the read pulse, for F 1 and F 2, respectively. Note that the two sets of filters have a CW efficiency of transmission at resonance of $\sim 65\%$. Due to the different total bandwidth of 40 MHz (80 MHz) for F 1 (F 2), the relative transmission efficiency of the pulses is about 40% lower for F 1 using 30 ns long pulses. The experiment is paused and the filters are locked on resonance with the cavity every 8 s, flipping the switches to use the CW signal from the FILTER LOCK LINE (detectors not shown). The average time needed to lock the two filter setups is about 1 s. The signal photons are detected using superconducting nanowire single photon detectors (SNSPD).

PHASE STABILITY

A fundamental part of the experiment is the phase difference acquired by the pulses in the unbalanced Mach-Zehnder interferometer, which has to be actively locked. In order to do so, the two strong control pulses from the read laser line are routed via a 90:10 BS to a long delay line ($\approx 1 \mu\text{s}$ of delay) to have them temporally spaced from the signal. A PBS is inserted in the line to minimize polarization drifts. After passing through the unbalanced interferometer, the pulses are reflected by the first cavity of both filter setups and are routed by circulators to a balanced detector. A sample&hold board (not shown in Fig 3.8) is used to select the correct pulse and feed it as the input voltage to a Red Pitaya board. The output of the board is amplified (not shown) and sent to the fiber stretcher.

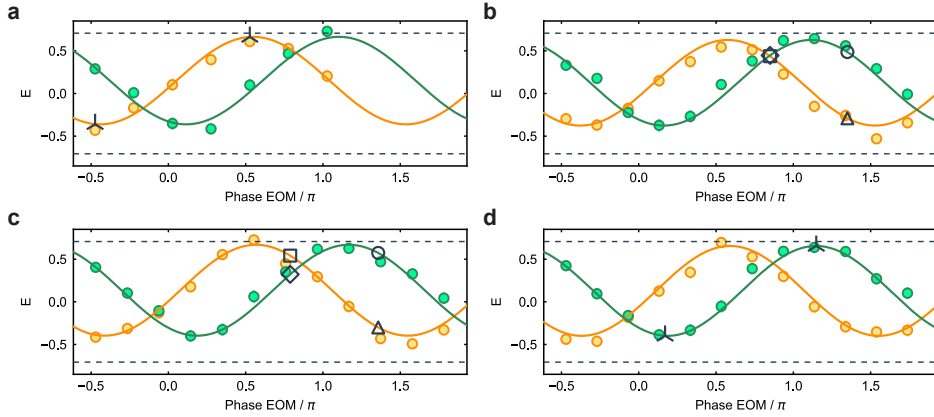


Figure 3.10: a) Correlation coefficients E , sweeping ϕ_w and for $\phi_r = 0$ (in orange) and $\phi_r = \pi/2$ (in green), for higher pulse energies with respect to the main text. The black markers (tri) are at the chosen phases for the additional measure of R . b), c) Same as a) for the calibration of the phases for the Bell test. The chosen points differ from the optimal theoretical points of $\phi_0 \pm \pi/4$ by no more than $\approx \pi/20$. The black markers are square, triangle, diamond and circle for the CHSH point (ϕ_w^0, ϕ_r^0) , (ϕ_w^1, ϕ_r^0) , (ϕ_w^0, ϕ_r^1) and (ϕ_w^1, ϕ_r^1) respectively. d) As reported in a) for the additional measurement of R with $\phi_r = \pi/2$. All errors are one standard deviation and are too small to be seen. The small asymmetry in the value of E around zero is a result of the different filter setup efficiencies (see section 3.5).

The Red Pitaya runs a PID program [46] and the feedback loop is ultimately limited by the bandwidth of the fiber stretcher (approx. 20 kHz).

The phase stability can be measured by tracking the voltage of the locking pulse on the balanced detector. In Fig. 3.9a (b) we plot the occurrence histogram of the phase difference acquired passing the interferometer for the write (read) pulses, in the case the interferometer is locked (in blue (red)), or unlocked (in green). The FWHM are $\approx \pi/7$ for the write and $\approx \pi/20$ for the read pulses. This phase spread is the same for the Stokes (anti-Stokes) scattered photons. Note that the FWHM of phase difference for write and read pulses are different, since the phase acquired by the write laser pulse also depends on the relative frequency jitter of the two lasers. This will only affect the pulses from the write laser since the lock pulses are generated from the read laser. This frequency jitter is reported in Fig. 3.9c, where the occurrence histogram of the frequency difference from the beatlock is shown. Here the FWHM is around 0.5 MHz.

We use FPC 2 to balance the lock signal from the INT LOCK LINE at the balanced detector. We then lock the interferometer and use the first order interference from very weak pulses from the write laser, on resonance with the filter cavities, to measure the interferometer visibility. We set the EOM voltage to the maximum visibility point and maximize it using FPC 1 (i.e. we align the polarization of the signal) while compensating with FPC 2 for the lock pulses. A typical interference pattern is shown in Fig. 3.9d. We report an average interferometer visibility of $V_{\text{int}} \approx 94\%$ during the whole experiment.

PHASE CALIBRATION

To perform the measurements in the main text we need to first accurately calibrate the phase setting. This is done by performing a measurement of E while sweeping ϕ_w and for two settings of ϕ_r . Here we use higher pulse energies with respect to the actual measurement reported in the main text, such that the scattering probability increases at the expense of having a lower value of E . We use 90 fj (225 fj) for the write (read) pulses, which gives $p_w = 0.6\%$, $p_r = 1.4\%$. With these settings we obtain more than 200 events per point in about 30 minutes. Fig. 3.10 shows several such calibration measurements for:

- the additional measurement of the R value (Fig. 3.10a),
- the two runs of integration for the Bell test (Fig. 3.10b, c)
- and for a final measure of R with $\phi_r = \pi/2$ (and to check that the phase difference during the second run of integration for the Bell test is small, Fig. 3.10d).

The values in orange are for $\phi_r = 0$, while $\phi_r \approx \pi/2$ is shown in green. A small deviation from the desired $\pi/2$ phase difference between the orange and green curves can be seen and the exact values are $\phi_r = \pi/1.8, \pi/1.9, \pi/1.7, \pi/1.8$, for Fig. 3.10a,b,c,d respectively. For the fits of the two datasets we use a sinusoidal function, which serves as a guide to the eye and to numerically calculate the optimal phase points. For the additional measure of R we simply use the phases where E is maximum and minimum (tri markers, Fig. 3.10a and d). For the Bell test, instead, we use the fit to numerically calculate the expected S value and choose the phases where the expected S is maximum (square, triangle, diamond and circle markers for the CHSH point (ϕ_w^0, ϕ_r^0) , (ϕ_w^1, ϕ_r^0) , (ϕ_w^0, ϕ_r^1) and (ϕ_w^1, ϕ_r^1) respectively). In doing so, the experimentally obtained values differ slightly from the theoretical optimal point of $\phi_0 - \pi/4$ and $\phi_0 + \pi/4$ by a small margin ε . The value for ε for the data in Fig. 3.10b (c) is $\approx \pi/30$ and $\approx \pi/20$ ($\approx -\pi/40$ and $\approx \pi/20$), respectively. The phase offset ϕ_{off} is calibrated using the maximum and minimum point of E . We choose this particular calibration method to compensate for eventual drifts in the phase offset (ϕ_{off}), as well as small inaccuracies of phase difference for two sets of measurements with different ϕ_r . Using light to lock the interferometer at a different frequency and from a different path from that of the signal, gives rise to a (fixed) phase offset ϕ_{off} in the entangled state (see section 3.5). Note that without an external reference PBS a relative change in the polarization between lock pulses and signal pulses will cause a change in the phase shift ϕ_{off} . However, in our case, the relative change in ϕ_0 (equivalently for ϕ_{off}) is less than $\pi/50$ in all four measurements.

To further avoid that phase drifts affect only parts of the datasets, we integrate for one hour at each phase point at a time. We then cycle the chosen phases 4 times for phononic entanglement data (and 12 for the longer integration points), and 16 times for the Bell test.

EFFECT OF NON-CONSTANT FSR

The small dispersion in the waveguide causes a non-constant FSR between the mechanical peaks (see Fig. 3.2b). In Fig. 3.11a we report the histogram of the FSR between the mechanical modes. By using the frequency and amplitude of each mechanical peak in

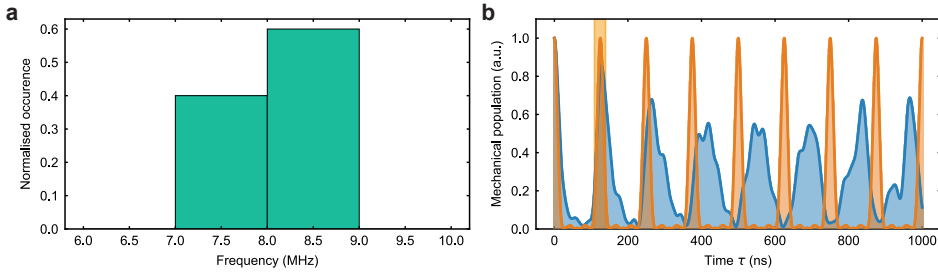


Figure 3.11: a) Normalized histogram of the FSR between the mechanical peaks shown in Fig. 3.2c of the main text with mean value of 8.3 MHz and standard deviation 0.8 MHz. b) The numerically calculated time-domain mechanical population (normalized) for the device spectrum (blue) and ideal spectrum with constant FSR (orange). The shaded area is the same as in Fig. 3.2c.

the spectrum, we numerically simulate the time-domain behavior of the mechanical system and compare it with the simulation of the ideal case (i.e. with perfectly constant FSR) [33]. As can be seen in Fig. 3.11b (blue graph), the mechanical packet is broadened and dimmer after several round-trips due to dispersion of the waveguide compared to the ideal case (orange graph). In this calculation the energy decay of the phonons has not been considered, tracing out any mechanical dissipation, and thus only taking the effect of the dispersion and non-constant FSR into account.

3.6. APPENDIX

In this appendix we report some facts and some *a posteriori* consideration on the experiment reported in this chapter. The idea is to give insights on the challenges encountered on the path to acquire the final dataset.

- In order to have a clean mechanical spectrum with a constant FSR it is very important to not have abrupt changes in the structure. Abrupt changes may cause reflection from the boundaries and create additional unwanted mechanical modes in the structure. Therefore, phononic crystal architectures are suitable for this manner, since the changes can be made to be adiabatic.
- Even in simulation the FSR is not perfectly constant. This is caused by some residual (little) dispersion of the waveguide and some disturbance mechanical mode as a result of strong coupling of the single mode cavity to the waveguide. A longer waveguide with higher group velocity can help to minimize the first contribution, and it will also have the advantage of a larger bandwidth of linear group velocity to be more robust on fabrication imperfection (so that relative shifts in the cavity and the center of the single mode band of the waveguide have less effect on the FSR distribution).
- In order to have a good bouncing pattern it is important to not have many mechanical modes involved. By adding more modes, the deviation of each mode (caused by dispersion and fabrication disorders) from the "perfectly even" FSR

would count more, resulting into less efficiency of retrieving the phononic wavepacket. This can be understood in the limit of 2 modes, where the FSR is always "perfect". In this regard, reducing the coupling between the cavity and waveguide would help to have fewer mechanical modes involved in the time dynamics. We use the code of Fig. 3.11 to simulate this effect and we report the result in Fig. 3.12. It is clear that for longer waveguides - so larger number of modes for a certain coupling bandwidth - the bouncing efficiency (the ratio between the height of the first round-trip to the height of the excitation peak at $t = 0$) decreases. Too short waveguides (normalized length < 0.75) are not possible since the traveling time is too short compared to the packet width. Decreasing the coupling from cavity to waveguide is not trivial since also the cavity parameters need to be changed to keep the mechanical and optical mode at the desired frequencies.

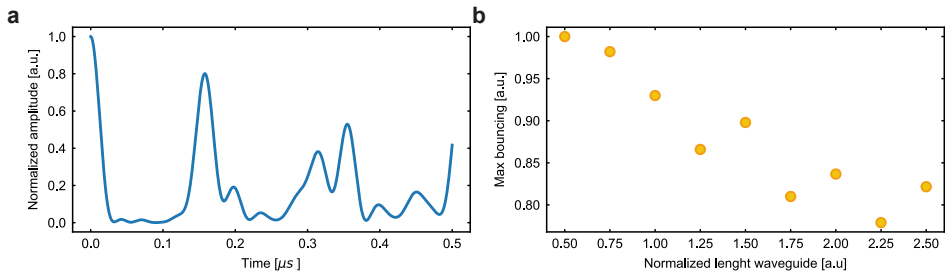


Figure 3.12: a) Bouncing pattern as calculated in Fig. 3.11, for a waveguide with 4 modes centered at 5 GHz each with amplitude from a gaussian distribution with sigma=20 MHz (that gives a nominal packet length of 50 ns). We add to the nominal FSR=8 MHz (that gives a nominal bouncing time $\tau = 120$ ns) a random small shift in the frequency for each mode (gaussian, with sigma=FSR/10). These numbers are close to the one of the device reported. b) Average of the maximum of the bouncing pattern in function of the normalized length of the waveguide. Each average is 20 repetition of the random gaussian shift. Length of 1 is for 4 modes waveguide as the device reported in the main text. The length is changed in the simulation modifying the FSR.

- Despite the precision in the nanofabrication, the devices fabricated will most likely have a bigger spread of the distribution of the FSR. We report that having the hole and beam sizes exactly as the simulated ones (within the precision of measurement of the SEM) is fundamental to have more devices with good bouncing pattern.
- We characterize 58 devices measuring the one-way coupling from the lensed fiber to the optical waveguide, the optical and mechanical resonances, the lifetime, the thermal occupancy as a function of the scattering rates and the $g_{\tau}^{(2)}$ behavior of thermal phononic wavepackets. We then select devices with one-way coupling higher than 55% (20 devices), lifetime longer than $1 \mu\text{s}$ (12 devices with both condition) and thermal occupancy lower than 0.1 for a fixed 5% scattering probability (5 devices with all 3 conditions). The last selecting criteria was having the maximum of the bounced $g_{\tau}^{(2)}$ higher than 1.6 (2 devices with all four conditions). We then selected the one with lower thermal occupancy for the experiment reported.

- Here we report another version of Fig. 3.1d, which, despite the less intuitive representation, is closer to the standard figure of a Bell test.

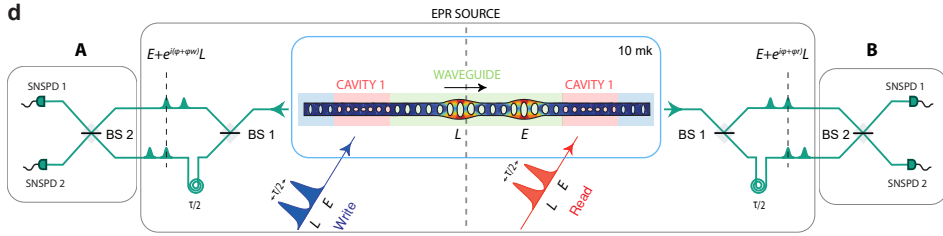


Figure 3.13: Different version of Fig. 3.1d. The vertical dashed line represent a "mirroring" of the device and setup. despite being less accurate and intuitive, it gives a very clear and immediate idea of the EPR pair (Stokes scattered photons and the phonons that traveled in the waveguide once converted in anti-Stokes scattered photons) and of the station A and B.

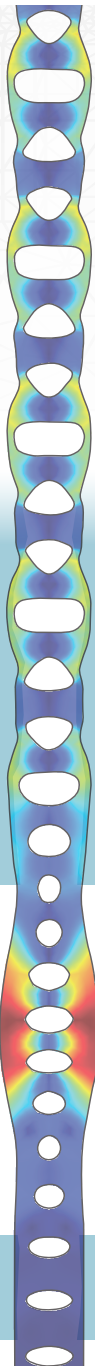
REFERENCES

- [1] F. Arute et al., Quantum supremacy using a programmable superconducting processor, *Nature* **574**, 505 (2019).
- [2] C. Zhong, Z. Wang, C. Zou, M. Zhang, X. Han, W. Fu, M. Xu, S. Shankar, M. H. Devoret, H. X. Tang, and L. Jiang, Proposal for Heralded Generation and Detection of Entangled Microwave-Optical-Photon Pairs, *Phys. Rev. Lett.* **124**, 10511 (2020).
- [3] H. J. Kimble, The quantum internet, *Nature* **453**, 1023 (2008).
- [4] N. Sangouard, C. Simon, H. de Riedmatten, and N. Gisin, Quantum repeaters based on atomic ensembles and linear optics, *Rev. Mod. Phys.* **83**, 33 (2011).
- [5] L. M. K. Vandersypen, H. Bluhm, J. S. Clarke, A. S. Dzurak, R. Ishihara, A. Morello, D. J. Reilly, L. R. Schreiber, and M. Veldhorst, Interfacing spin qubits in quantum dots and donors—hot, dense, and coherent, *npj Quantum Inf.* **3**, 1 (2017).
- [6] M. Wallquist, K. Hammerer, P. Rabl, M. Lukin, and P. Zoller, Hybrid quantum devices and quantum engineering, *Phys. Scr.* **T137**, 014001 (2009).
- [7] J. T. Hill, A. H. Safavi-Naeini, J. Chan, and O. Painter, Coherent optical wavelength conversion via cavity optomechanics, *Nature Commun.* **3**, 1196 (2012).
- [8] A. Vainsencher, K. J. Satzinger, G. A. Peairs, and A. N. Cleland, Bi-directional conversion between microwave and optical frequencies in a piezoelectric optomechanical device, *Appl. Phys. Lett.* **109**, 033107 (2016).
- [9] R. W. Andrews, R. W. Peterson, T. P. Purdy, K. Cicak, R. W. Simmonds, C. A. Regal, and K. W. Lehnert, Bidirectional and efficient conversion between microwave and optical light, *Nature Phys.* **10**, 321 (2014).
- [10] X. Han, W. Fu, C. Zhong, C.-L. Zou, Y. Xu, A. A. Sayem, M. Xu, S. Wang, R. Cheng, L. Jiang, and H. X. Tang, Cavity piezo-mechanics for superconducting-nanophotonic quantum interface, *Nature Commun.* **11**, 3237 (2020).
- [11] G. Arnold, M. Wulf, S. Barzanjeh, E. S. Redchenko, A. Rueda, W. J. Hease, F. Hassani, and J. M. Fink, Converting microwave and telecom photons with a silicon photonic nanomechanical interface, *Nature Commun.* **11**, 4460 (2020).
- [12] W. Jiang, C. J. Sarabalis, Y. D. Dahmani, R. N. Patel, F. M. Mayor, T. P. McKenna, R. Van Laer, and A. H. Safavi-Naeini, Efficient bidirectional piezo-optomechanical transduction between microwave and optical frequency, *Nature Commun.* **11**, 1166 (2020).
- [13] M. Forsch, R. Stockill, A. Wallucks, I. Marinković, C. Gärtner, R. A. Norte, F. van Otten, A. Fiore, K. Srinivasan, and S. Gröblacher, Microwave-to-optics conversion using a mechanical oscillator in its quantum groundstate, *Nature Phys.* **16**, 69 (2020).

- [14] R. Stockill, M. Forsch, F. Hijazi, G. Beaudoin, K. Pantzas, I. Sagnes, R. Braive, and S. Gröblacher, Ultra-low-noise Microwave to Optics Conversion in Gallium Phosphide, [Nature Commun.](#) **13**, 6583 (2022).
- [15] M. Mirhosseini, A. Sipahigil, M. Kalaei, and O. Painter, Superconducting qubit to optical photon transduction, [Nature](#) **588**, 599 (2020).
- [16] T. Palomaki, J. Teufel, R. Simmonds, and K. Lehnert, Entangling mechanical motion with microwave fields, [Science](#) **342**, 710 (2013).
- [17] Y. Chu, P. Kharel, W. H. Renninger, L. D. Burkhardt, L. Frunzio, P. T. Rakich, and R. J. Schoelkopf, Quantum acoustics with superconducting qubits, [Science](#) **358**, 199 (2017).
- [18] R. Blatt and D. Wineland, Entangled states of trapped atomic ions, [Nature](#) **453**, 1008 (2008).
- [19] P. Delsing *et al.*, The 2019 surface acoustic waves roadmap, [J. Phys. D: Appl. Phys.](#) **52**, 353001 (2019).
- [20] D. A. Golter, T. Oo, M. Amezcua, I. Lekavicius, K. A. Stewart, and H. Wang, Coupling a surface acoustic wave to an electron spin in diamond via a dark state, [Phys. Rev. X](#) **6**, 041060 (2016).
- [21] A. Bienfait, K. J. Satzinger, Y. P. Zhong, H.-S. Chang, M.-H. Chou, C. R. Conner, E. Dumur, J. Grebel, G. A. Peairs, R. G. Povey, and A. N. Cleland, Phonon-mediated quantum state transfer and remote qubit entanglement, [Science](#) **364**, 368 (2019).
- [22] R. P. G. McNeil, M. Kataoka, C. J. B. Ford, C. H. W. Barnes, D. Anderson, G. A. C. Jones, I. Farrer, and D. A. Ritchie, On-demand single-electron transfer between distant quantum dots, [Nature](#) **477**, 439 (2011).
- [23] S. Hermelin, S. Takada, M. Yamamoto, S. Tarucha, A. D. Wieck, L. Saminadayar, C. Bäuerle, and T. Meunier, Electrons surfing on a sound wave as a platform for quantum optics with flying electrons, [Nature](#) **477**, 435 (2011).
- [24] T. Neuman, M. Eichenfield, M. E. Trusheim, L. Hackett, P. Narang, and D. Englund, A phononic interface between a superconducting quantum processor and quantum networked spin memories, [npj Quantum Inf.](#) **7**, 1 (2021).
- [25] M. Aspelmeyer, T. J. Kippenberg, and F. Marquardt, Cavity optomechanics, [Rev. Mod. Phys.](#) **86**, 1391 (2014).
- [26] S. Barzanjeh, A. Xuereb, S. Gröblacher, M. Paternostro, C. A. Regal, and E. M. Weig, Optomechanics for quantum technologies, [Nature Phys.](#) **18**, 15 (2022).
- [27] M. K. Ekström, T. Aref, J. Runeson, J. Björck, I. Boström, and P. Delsing, Surface acoustic wave unidirectional transducers for quantum applications, [Appl. Phys. Lett.](#) **110**, 073105 (2017).

- [28] É. Dumur, K. J. Satzinger, G. A. Peairs, M.-H. Chou, A. Bienfait, H.-S. Chang, C. R. Conner, J. Grebel, R. G. Povey, Y. P. Zhong, and A. N. Cleland, Quantum communication with itinerant surface acoustic wave phonons, *npj Quantum Inf.* **7**, 173 (2021).
- [29] A. Bienfait, Y. P. Zhong, H. S. Chang, M. H. Chou, C. R. Conner, Dumur, J. Grebel, G. A. Peairs, R. G. Povey, K. J. Satzinger, and A. N. Cleland, Quantum Erasure Using Entangled Surface Acoustic Phonons, *Phys. Rev. X* **10**, 21055 (2020).
- [30] J. Chan, A. H. Safavi-Naeini, J. T. Hill, S. Meenehan, and O. Painter, Optimized optomechanical crystal cavity with acoustic radiation shield, *App. Phys. Lett.* **101**, 081115 (2012).
- [31] A. Wallucks, I. Marinković, B. Hensen, R. Stockill, and S. Gröblacher, A quantum memory at telecom wavelengths, *Nature Phys.* **16**, 772 (2020).
- [32] R. N. Patel, Z. Wang, W. Jiang, C. J. Sarabalis, J. T. Hill, and A. H. Safavi-Naeini, Single-mode phononic wire, *Phys. Rev. Lett.* **121**, 040501 (2018).
- [33] A. Zivari, R. Stockill, N. Fiaschi, and S. Gröblacher, Non-classical mechanical states guided in a phononic waveguide, *Nature Phys.* **18**, 789 (2022).
- [34] J. F. Clauser, M. A. Horne, A. Shimony, and R. A. Holt, Proposed experiment to test local hidden-variable theories, *Phys. Rev. Lett.* **23**, 880 (1969).
- [35] I. Marinković, A. Wallucks, R. Riedinger, S. Hong, M. Aspelmeyer, and S. Gröblacher, An optomechanical Bell test, *Phys. Rev. Lett.* **121**, 220404 (2018).
- [36] S. T. Velez, V. Sudhir, N. Sangouard, and C. Galland, Bell correlations between light and vibration at ambient conditions, *Science Adv.* **6**, eabb0260 (2020).
- [37] R. Riedinger, S. Hong, R. A. Norte, J. A. Slater, J. Shang, A. G. Krause, V. Anant, M. Aspelmeyer, and S. Gröblacher, Non-classical correlations between single photons and phonons from a mechanical oscillator, *Nature* **530**, 313 (2016).
- [38] S. Weis, R. Rivière, S. Deléglise, E. Gavartin, O. Arcizet, A. Schliesser, and T. J. Kippenberg, Optomechanically Induced Transparency, *Science* **330**, 1520 (2010).
- [39] R. Stockill, M. Forsch, G. Beaudoin, K. Pantzas, I. Sagnes, R. Braive, and S. Gröblacher, Gallium phosphide as a piezoelectric platform for quantum optomechanics, *Phys. Rev. Lett.* **123**, 163602 (2019).
- [40] S. Hong, R. Riedinger, I. Marinković, A. Wallucks, S. G. Hofer, R. A. Norte, M. Aspelmeyer, and S. Gröblacher, Hanbury Brown and Twiss interferometry of single phonons from an optomechanical resonator, *Science* **358**, 203 (2017).
- [41] K. Børkje, A. Nunnenkamp, and S. M. Girvin, Proposal for entangling remote micro-mechanical oscillators via optical measurements, *Phys. Rev. Lett.* **107**, 123601 (2011).

- [42] R. Riedinger, A. Wallucks, I. Marinković, C. Löschnauer, M. Aspelmeyer, S. Hong, and S. Gröblacher, Remote quantum entanglement between two micromechanical oscillators, *Nature* **556**, 473 (2018).
- [43] L. M. Duan, M. D. Lukin, J. I. Cirac, and P. Zoller, Long-distance quantum communication with atomic ensembles and linear optics., *Nature* **414**, 413 (2001).
- [44] J. C. Taylor, E. Chatterjee, W. F. Kindel, D. Soh, and M. Eichenfield, Reconfigurable quantum phononic circuits via piezo-acoustomechanical interactions, *npj Quantum Inf.* **8**, 19 (2022).
- [45] J. Chan, T. P. M. Alegre, A. H. Safavi-Naeini, J. T. Hill, A. Krause, S. Gröblacher, M. Aspelmeyer, and O. Painter, Laser cooling of a nanomechanical oscillator into its quantum ground state, *Nature* **478**, 89 (2011).
- [46] M. A. Luda, M. Drechsler, C. T. Schmiegelow, and J. Codnia, Compact embedded device for lock-in measurements and experiment active control, *Rev. Scien. Instr.* **90**, 023106 (2019).
- [47] A. Aspect, J. Dalibard, and G. Roger, Experimental test of bell's inequalities using time-varying analyzers, *Phys. Rev. Lett.* **49**, 1804 (1982).

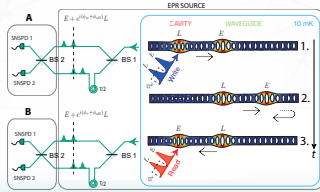


Abstract:

$\nu_1^{1/2}$ Distributing quantum entanglement on a chip is a crucial step towards realizing scalable quantum processors.
 $\nu_2^{1/2}$ Phonons – quantized guided mechanical wavepackets – have small size and low propagation speed and can connect heterogeneous quantum systems on a chip.

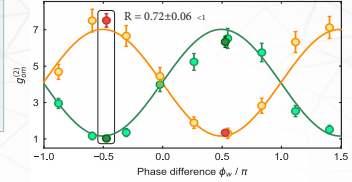
Experimental setup:

$\nu_3^{1/2}$ The mechanical quantum state is created in an optomechanical cavity and then launched into a phononic waveguide in which it propagates for around 200 μm . An unbalanced interferometer overlap in time the Early and Late scattered phonons.



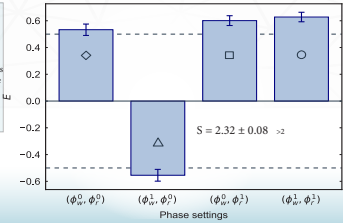
Entangled Phonons:

$\nu_4^{1/2}$ We experimentally demonstrate the feasibility of distributing quantum information using phonons, by realizing quantum entanglement between two traveling phonons (proved via the entanglement witness R [1]). The time dependence on phase shows the coherence of the state.



Bell Test:

$\nu_5^{1/2}$ We further show how the phononic, together with a photonic qubit, can be used to violate a Bell-type inequality (having the S parameter higher than the classical threshold [2]). This underlines the suitability of the phononic system as a DLCZ unit cell for long distance quantum communication.



Using Phonons to Route Quantum information on-chip

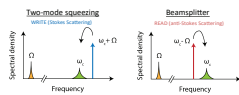
Amirparsa Zivari*, Niccolò Fiaschi*, Roel Burgwal, Ewold Verhagen, Robert Stockill, and Simon Groblacher

The  group

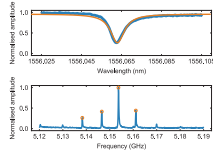


TU Delft

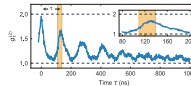
Opto-Mechanical interactions:



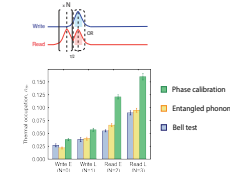
Optics, mechanics:



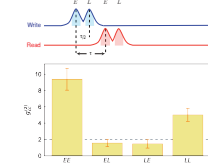
Round trip time:



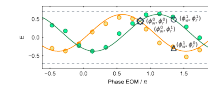
Thermal occupancy:



Double Cross-correlation:



Phases calibration:



The  paper

On-chip distribution of quantum information using traveling phonons

ERC NWO
 KAVI INSTITUTE
 of Nanoscience Delft

4

A SINGLE-PHONON DIRECTIONAL COUPLER

"And if I were a drone
Patrolling foreign skies
With my electronic eyes for guidance
And the element of surprise
I would be afraid
To find someone home"
[Roger Waters - Deja Vu]

**Amirparsa ZIVARI*, Niccolò FIASCHI*, Lorenzo SCARPELLI*,
Menno JANSEN, Roel BURGWAL, Ewold VERHAGEN, Simon
GRÖBLACHER**

Integrated photonics has enabled countless technologies in telecommunications, spectroscopy, metrology, quantum optics, and quantum information processing. Using highly confined guided optical modes is the key that has made integrated circuits possible and has led to scaling of complex designs, benefiting from their small footprint. At the same time, the field of quantum acoustics has recently gained significant attention due to its various potential advantages over its photonic counterparts, including smaller mode volume, lower

This work is under revision and is available on arXiv: Amirparsa Zivari*, Niccolò Fiaschi*, Lorenzo Scarpelli*, Menno Jansen, Roel Burgwal, Ewold Verhagen, and Simon Gröblacher, *A single-phonon directional coupler*, arXiv preprint arXiv:2312.04414 (2023)

* indicates equal contribution

energy, and orders of magnitude slower propagation speeds, as well as the potential for interconnecting distinct quantum systems. Developing analogous integrated phononic technology is critical for realizing the full potential of phonons and could lead to groundbreaking new applications, such as scalable quantum computing and hybrid quantum devices. In this work, we demonstrate for the first time a 4-port directional coupler for quantum mechanical excitations – a crucial component for integrated phononic circuits. Adjusting the length of the coupling region allows to realize phononic beam splitters with varying splitting ratios. By sending a single-phonon Fock state onto one of these phononic splitters, we demonstrate the capability of using the directional coupler directly in the quantum regime. Our work provides an essential step towards an integrated phononic platform for both classical and quantum technologies applications.

4.1. INTRODUCTION

Quantum technologies have seen rapid progress in the past few years, with great promise for testing fundamental science, as well as for commercial applications. The remarkable demonstrations of quantum computational advantage [1, 2] over classical processors and long-distance quantum teleportation using a satellite [3] have highlighted the fundamental need to create heterogeneous quantum systems [4] in order to realize advanced quantum technologies [5], such as quantum networks [6]. Phonons – quantized mechanical vibrations – are regarded as a critical resource to connect different quantum devices [7, 8], with applications in, for example, quantum transduction [9–11] and sensing [12]. Accordingly, routing and manipulating single mechanical vibrations on a chip is crucial to transfer quantum information between different quantum systems and unlock the potential of hybrid quantum systems.

To date, two main platforms have been developed for this purpose: surface acoustic waves (SAWs) [13–15] and highly confined one-dimensional phononic waveguides based on phononic crystals [16]. In particular, SAWs have been used to couple two qubits to one another over a distance of around 2 mm [13]. The propagation distance of these acoustic waves is however limited by the relatively short phononic lifetime T_1 in the range of tens of microseconds. At the same time, due to the two-dimensional, inherently open nature of SAWs, devices are characterized by a relatively large footprint, making scaling to more complex circuits challenging. Nevertheless, significant progress has recently culminated in a remarkable proof-of-principle demonstration of a phononic beam splitter for SAWs [17]. Highly confined GHz phonons in single-mode waveguides on the other hand are characterized by milliseconds-long lifetimes [18] and feature a relatively small footprint compared to SAWs, making them an ideal platform for on-chip quantum applications [19] and for integrated phononic circuits in general. In these structures, an opto-mechanical resonator is typically used for the generation, manipulation, and detection of highly confined phonons: from realizing single Fock states of phonons [20, 21], remote phonon-phonon quantum entanglement [22], and optomechanical Bell tests [23] to quantum teleportation [24]. More recently, single-phonon waveguides were successfully connected to such opto-mechanical resonators to route single phonon wavepackets on a chip [19].

In photonics, beam splitters form the fundamental cornerstone for a myriad of applications – they provide a classical platform to investigate the wave nature of light, are used as combiners and power distributors, are critical for quantum optics experiments, and are an essential resource for linear optical quantum computing and processing [25], to name a few examples. Importantly, the ability to miniaturize photonic components has been paramount for realizing novel technologies, as it enables photonic integrated circuits with thousands of components while still preserving a millimeter-scale footprint [26–28]. In close analogy, here we experimentally realize the phononic equivalent of this crucial component – an integrated phononic beam splitter – arguably the most critical element to perform advanced on-chip manipulation of mechanical excitations. Drawing inspiration from photonics, we design our beam splitter using a 4-port directional coupler architecture, where two identical single-mode waveguides are coupled together in an interaction region, creating symmetric and anti-symmetric supermodes which are delocalized in both waveguides. The splitting ratio can be adjusted by chang-

ing the length of this interaction region. We demonstrate the beam splitter behavior for both coherent and single-phonon Fock states. With a footprint of only about $200 \times 5 \mu\text{m}$, our device is easily scalable and represents a critical step towards the realization of integrated phononic circuits [29–31].

4.2. DEVICE DESIGN AND CHARACTERIZATION

A conceptual sketch of our device is shown in Fig. 4.1a. The device is formed by two single-phonon sources (the optomechanical cavities), two single-mode waveguides, a beam splitter, and two single-phonon detectors. To realize the phononic beam splitter, we design an integrated directional coupler using a phononic crystal architecture. The corresponding unit cell of length a is shown in the inset of Fig. 4.1b. It consists of two single-mode waveguides [16], connected together via a phononic bridge. This interaction region allows mechanical energy to be exchanged between the waveguides, resembling the evanescent coupling typically used in photonic directional couplers. In contrast to a conventional directional coupler, the two waveguides host both the two incoming, as well as the two outgoing ports, as detailed below.

To verify the analogy to a photonic directional coupler, we perform finite element simulations of the unit cell using COMSOL and calculate the corresponding band structure. The results are shown in Fig. 4.1b, for the breathing mode in the in-plane direction. Within a frequency range of 4.5 – 5.3 GHz, the band structure is dominated by the symmetric and anti-symmetric supermodes, which are the even and odd linear combinations of the uncoupled modes, respectively. A zoom-in around 4.9 GHz shown in Fig. 4.1c reveals that the two supermodes have different propagation constants $\beta_{s,a}$, which relate to the coupling coefficient β per unit length as $\beta = (\beta_s - \beta_a)/2$, with the subscripts $i = \{s, a\}$ indicating the symmetric and anti-symmetric supermodes, respectively. As a result of the coupling, for each wave vector, the supermodes are frequency split by the normal mode splitting $\Delta\nu_{\text{NMS}}$, as expected from two coupled degenerate harmonic oscillators. We use the extracted value of β to estimate the coupling length (i.e. number of beam splitter unit cells) needed for different splitting ratio. To reduce the experimental complexity, we engineer a device with a (phononic) mirror at the center of Fig. 4.1a (represented by the dashed line, and realized by a free-standing end) [16, 19]. In this way the same two cavities can be used as transmitters and receivers. The output arms of the directional coupler are connected to two, uncoupled single-mode, waveguides, each terminated with a (nominally identical) optomechanical cavity. The cavities are used to generate and detect single phonons via the optomechanical interaction. Through finite element simulation of the full structure we can calculate the optomechanical coupling rates for different modes, plotted in Fig. 4.1d. The optomechanical response is dominated by a series of Fabry-Pérot modes, equally spaced by $\Delta\nu_{\text{FRS}}$, which arise from the hybridization of the mechanical cavity mode with the series of modes supported by the free-ending waveguide. Furthermore, each Fabry-Pérot mode is split by $\Delta\nu_{\text{NMS}}$ into a doublet due to the mechanical coupling between the two devices (see SI 4.6 for more details). Scanning electron microscope (SEM) pictures of one of the fabricated devices, made from 250 nm silicon [16, 19], are shown in Fig. 4.1e. For space reasons the waveguides are not fully shown and the total length of the device is about $200 \mu\text{m}$.

To minimize the thermal noise background, we cool our device to 20 mK using a di-

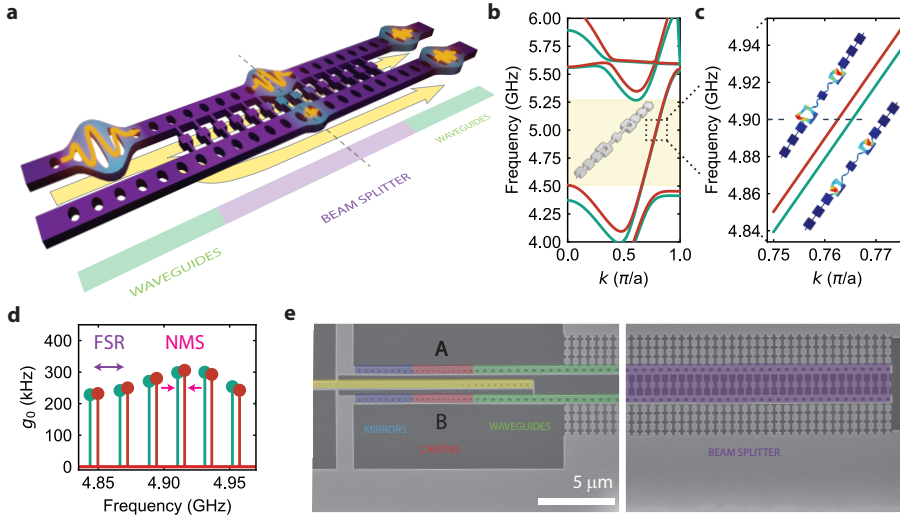


Figure 4.1: a) Sketch of the working principle of the phononic directional coupler device. Beside the central beam splitter (purple), the device also includes two phononic waveguides (green). b) Band structure simulation of the in-plane breathing mode of the unit cell structure (inset) of the directional coupler, showing normal mode splitting of the symmetric (red) and anti-symmetric supermodes due to the coupling. c) The splitting between the two modes is clearly visible in the zoom-in around 4.9 GHz. The oscillating anti-symmetric and symmetric supermodes are shown on the top and bottom, respectively. d) Simulated optomechanical single photon coupling rate of the full structure. The mechanical mode of the optomechanical cavity is hybridized by a series of Fabry-Pérot modes of the waveguide and each mode is split into a doublet of symmetric (green) and anti-symmetric normal modes (more details are given in SI 4.6). e) Scanning electron microscope (SEM) images of the fabricated device with false color highlighting of the different parts – the phononic and photonic mirrors (blue), the optomechanical cavities (red), the phononic waveguide (green), the phononic beam splitter (purple). Note that due to space constraints, only a short section of the waveguides is shown.

lution refrigerator, initializing all mechanical modes of interest in their quantum ground states. We measure the optical characteristics of the two optomechanical cavities by scanning a continuous-wave laser through their resonances and measure the reflected signal on a photodiode. The reflection spectra are shown in Fig. 4.2a and b (for cavity A and B, respectively). Fitting the line shape with a Lorentzian, we determine the optical cavity resonance at $\lambda \approx 1546.81$ nm ($\lambda \approx 1547.98$ nm), and a full-width at half-maximum (FWHM) of $\kappa/2\pi \approx 1.23$ GHz ($\kappa/2\pi \approx 1.34$ GHz), with an intrinsic loss rate of $\kappa_i/2\pi \approx 430$ MHz ($\kappa_i/2\pi \approx 600$ MHz), for device A (B), respectively. The cavities are nominally identical, apart from fabrication imperfections. Since the difference between the optical resonances is much bigger than the linewidths and mechanical frequencies, we can address each cavity individually. This allows us to measure the mechanical spectrum of the structure using optomechanically induced transparency (OMIT) [32]. The results are plotted in Fig. 4.2c and d (for cavity A and B, respectively). Both devices, within a region of ~ 30 MHz (highlighted in green shaded area) show a series of doublets with a normal mode splitting of $\Delta\nu_{\text{NMS}} \approx 2.5$ MHz, spaced almost evenly by $\Delta\nu_{\text{FRS}} \approx 10$ MHz. This clearly shows that, due to the precision in nanofabrication, the mechanical modes of the

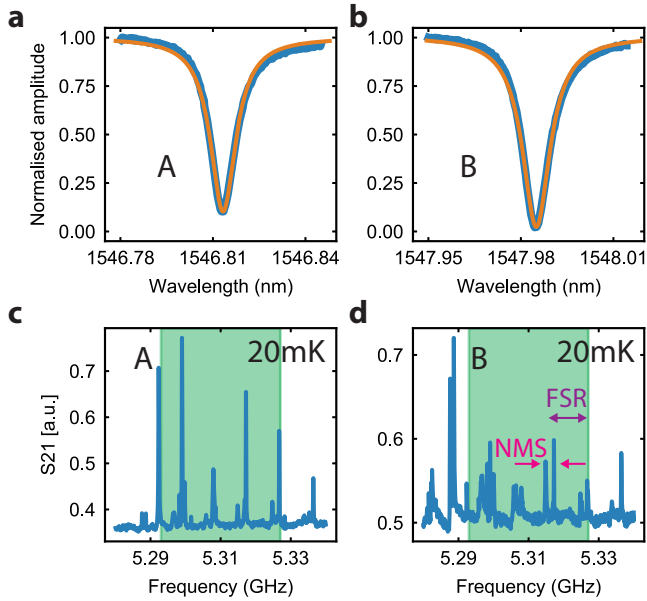


Figure 4.2: a,b) Optical response of device A (left) and B (right). The devices have optical resonances in the C-band at telecom wavelengths. c,d) Mechanical spectrum of device A (left) and B (right) measured using OMIT. We observe a series of Fabry-Pérot modes spaced by $\Delta\nu_{\text{FRS}}$ and split by the normal-mode splitting $\Delta\nu_{\text{NMS}}$ due to the directional coupler. The green shaded area indicates the spectral region used to investigate the dynamics of phononic wavepackets (see text for more details).

cavity-waveguide systems hybridize through the directional coupler. As will be shown later, for this particular device this corresponds to a directional coupler with splitting ratio of approximately 50:50. We further determine the equivalent single photon optomechanical coupling rate from the Stokes scattered photon rate by sending 30 ns optical pulses to the devices. We measure values of $g_{0,A} = 380$ kHz and $g_{0,B} = 530$ kHz for device A and B, respectively, in good agreement with simulations.

4.3. COHERENT DRIVE MEASUREMENT

In order to characterize the time-domain behavior of the beam splitter, we study the propagation of coherent phononic wavepackets. We detune the laser by 6 GHz from the optical cavity we aim to excite. By using this detuning the Stokes (and anti-Stokes) scattering rate are strongly suppressed and can be neglected. We then modulate sidebands at the mechanical frequency $f_m = 5.31$ GHz onto the laser using an electro-optical modulator (EOM). The sidebands create a beating tone at the mechanical frequency, which coherently drives the mechanical motion through radiation pressure. The optical pulses are created using an acousto-optical modulator and are 30 ns long, such that we excite modes only within the spectral region shown in the green shaded area in Fig. 4.2c and d, for cavity A and B, respectively.

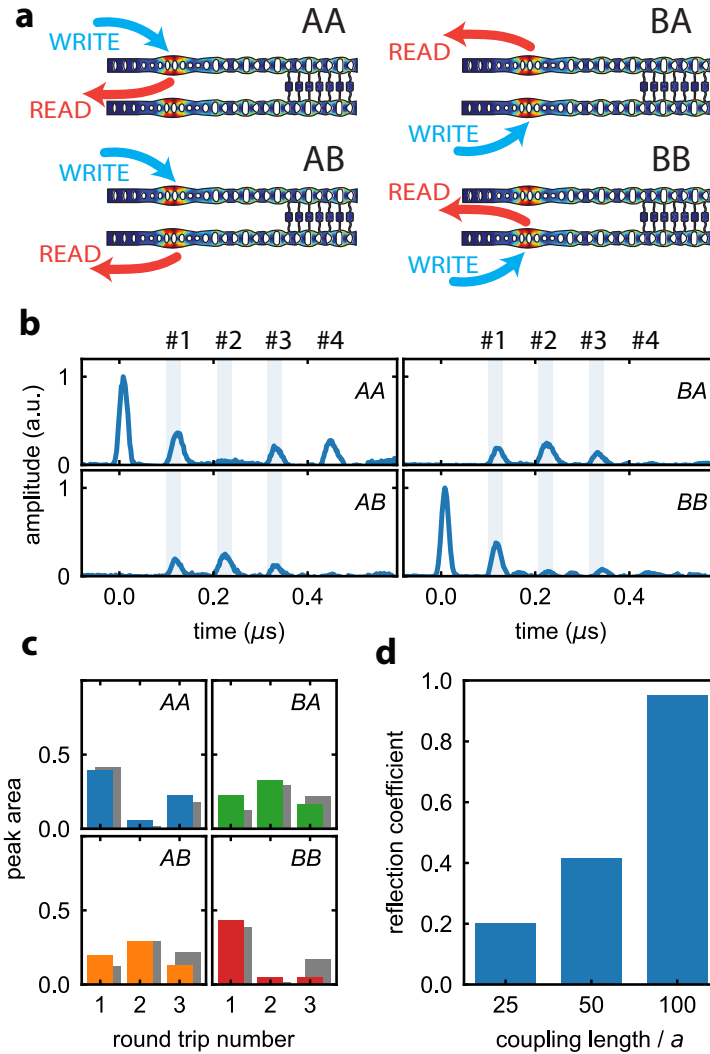


Figure 4.3: a) Different permutations of exciting and reading the two cavities. b) We measure the phononic population of each cavity over time (first letter: excited cavity, second letter: read-out cavity), using a coherent state phononic wavepacket. The number on the top corresponds to the round trip number of the phononic packet with the respective time range highlighted in blue. c) Blue, orange, green, red color bars: integrated counts of phononic population around the first, second and third round-trip time. Grey color bars: result of the global fit described in the main text, from which we extract a reflection coefficient $R = 0.43$. d) The reflection coefficient of the phononic directional coupler as a function of the coupling length, measured on different devices.

To measure the phonon occupancy inside the cavities A and B, we again use a continuous-wave laser, red-detuned by the mechanical frequency from the optical resonances. The results of the calibrated phononic population in the cavities over time are shown in Fig. 4.3b, for different combinations of exciting (first letter on the top right corner of each panel) and reading (second letter on the top right corner of each panel) cavities, as it is depicted in Fig. 4.3a – see SI 4.6 for more details. This device has a coupler length of 50 beam splitter unit cells, which from simulations corresponds to an approx. 50:50 beam splitter. As a result of the directional coupler, the excitation is then split between the two waveguides and reaches the cavities A and B after the first round trip, with a $\pi/2$ phase difference between the arms. Subsequently, at the second recombination on the beam splitter (second round-trip), the excitation travels to the opposite port with respect to the one excited initially. This is due to the fact that the phase difference between our phononic packets in the two arms remains constant while they travel through the waveguides [19]. Due to the slight mismatch of the two waveguide-cavity systems and dispersions in the coupler region caused from the fabrication disorders, the amount of energy populating the opposite cavities is slightly different.

To extract the splitting ratio of the directional coupler, we calculate the (normalized) area under the mechanical wavepacket around the first, second, and third round-trip time, corresponding to the light-blue shaded area in Fig. 4.3b, for the indicated excitation and detection combinations (see SI 4.6 for more details). The corresponding integrated counts are shown in blue, orange, green and red color bars in Fig. 4.3c. To model these data, we use a transfer matrix approach, where the action of the directional coupler is described by a lossless beam splitter matrix U_{BS} , written in terms of a reflection coefficient r and a transmission coefficient $t = \sqrt{1 - r^2}$. Phonon losses are negligible to first order since the phononic lifetime is much longer than the round-trip time (see SI 4.6). The phonon population after N passes through the directional coupler is then proportional to $A_{ij}(U_{BS})^N$, where the factor A_{ij} , with $i, j = \{A, B\}$, takes into account losses and dispersion mismatch. A more accurate description of these terms would require modeling of the time dynamics with a multi-mode coupled-mode theory, which goes beyond the scope of this work. We then perform a global fitting procedure, where we impose $A_{AB} = A_{BA}$ to satisfy the reciprocity condition. The result of the fit is shown in grey color bars in Fig. 4.3c, from which we extract a reflection coefficient $R = |r|^2 = 0.43$. We repeat the same measurements for two different lengths of the coupling region (see SI 4.9) and extract the corresponding reflection coefficient. The results are shown in Fig. 4.3d, which clearly shows an increase of the reflection as the coupling length is increased. Importantly, these results show that our design allows to engineer phononic beam splitters with arbitrary splitting ratios.

4.4. SINGLE PHONON SPLITTING

Testing the response of our directional coupler to quantized excitations with single phonon wavepackets is a critical demonstration of its potential use for quantum applications. In order to create a single phonon, we use 30 ns “write” laser pulses, blue-detuned by the central mechanical frequency (5.31 GHz) from the optical resonances. This process can be described by a two-mode squeezed optomechanical interaction and detecting the Stokes scattered photon with a superconducting nanowire single photon detector

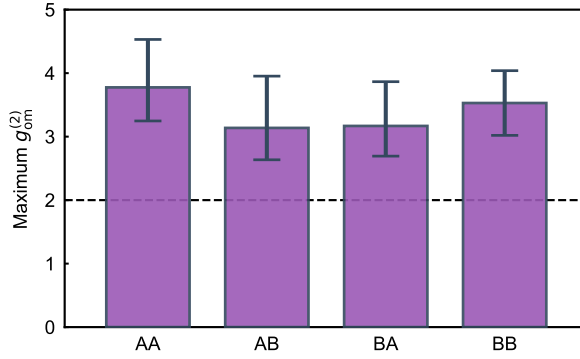


Figure 4.4: The second order cross-correlation $g_{om}^{(2)}$ between the Stokes and anti-Stokes scattered photons from the write and read pulses – we measure $g_{om,AA}^{(2)} = 3.8_{-0.5}^{+0.8}$, $g_{om,AB}^{(2)} = 3.1_{-0.5}^{+0.8}$, $g_{om,BA}^{(2)} = 3.2_{-0.5}^{+0.7}$ and $g_{om,BB}^{(2)} = 3.5_{-0.5}^{+0.5}$ – all values are above the classical threshold of 2 (dashed line) by more than two standard deviations. Error bars indicate one standard deviation.

(SNSPD), allows us to project the mechanical state of the optomechanical cavity onto a single phonon state [20]. This single phonon travels through the waveguide and either returns to the same cavity upon reflection, or goes to the opposite cavity after transmission in the coupling region. We then convert the mechanical state of each cavity to an optical photon, by sending 30 ns “read” laser pulses red-detuned by the same mechanical frequency from the optical cavities. This addresses a state swap optomechanical interaction resulting into anti-Stokes scattered photons. The time delay between the write and read pulses is set around the first round trip of the phononic wavepacket. We calculate the second order cross-correlation $g_{om}^{(2)}$ between the Stokes and anti-Stokes scattered photons for different combinations of exciting and reading cavities A and B, similarly to [20].

We use pulse energies of 220 fJ for write (Stokes) and 280 fJ for read (anti-Stokes) process, corresponding to a Stokes scattering probability of 1 % (1.6 %) and an anti-Stokes scattering probability of 1.2 % (2 %) for cavity A (B). At these low pulse energies, the thermal occupation of the cavities caused by heating of the lasers is negligible ($n_{th} < 0.18$ for all measurements configuration, see SI 4.6). We measure values of $g_{om,AA}^{(2)} = 3.8_{-0.5}^{+0.8}$, $g_{om,AB}^{(2)} = 3.1_{-0.5}^{+0.8}$, $g_{om,BA}^{(2)} = 3.2_{-0.5}^{+0.7}$ and $g_{om,BB}^{(2)} = 3.5_{-0.5}^{+0.5}$ (first index indicating the write cavity and second index the read cavity), which is plotted in Fig. 4.4. For each configuration the value is more than two standard deviations above the classical threshold of 2, unambiguously showing the non-classical behavior of the single phonon states measured in the different cavities after the excitations passed through the phononic beam splitter and either return back to the same cavity or travel to the opposite one. For more details on the experimental setup we refer to SI 4.6 and SI 4.6.

4.5. CONCLUSION

In conclusion, we have demonstrated an integrated directional coupler for GHz phonons – a crucial component for phononic integrated circuits [33]. Our demonstration is based on the development of the first integrated circuit involving single-phonon sources, detectors and single-mode waveguides, and we use it to demonstrate a beam splitter for both classical and quantum mechanical states. Due to the millisecond-long lifetime of phonons in these structures, as well as the ease of scalability, our device can be readily extended to build multi-mode interferometers of large dimensions, suitable for mechanical boson sampling and, more generally, for linear mechanical quantum computing [2, 17].

Through further development, piezo-electric materials can be included in our mechanical structure [11, 34], enabling electro-mechanical integrated devices such as, for example, phononic phase shifters [35]. With this powerful new tool at hand, a new paradigm of phononic devices can be realized, including mechanical Mach-Zender interferometers for sensing, switches for routing, and power multiplexers, to name a few, in addition to other more versatile mechanical counterparts of existing photonic technologies [36].

Additionally, using piezo-electric resonators, strong interactions between highly-confined GHz phonons and superconducting qubits can be engineered [9]. Moreover, the small mode-volume of highly confined phonons achieved with our design, allows engineering interactions with nanometer-scale quantum system, such as quantum dots [37] and color centers. Therefore, our directional coupler opens up exciting perspectives for hybrid quantum networks, enabling direct entanglement generation between distinct quantum systems without requiring entanglement swapping. We envision a platform with several quantum resources linked and combined together through mechanical quantum channels, taking advantage of the best performances of each individual technology. The strong lateral confinement of the propagating modes, allows our devices to establish a direct analogy with photonic integrated circuits, and therefore paves the way towards the new field of integrated quantum phononics.

Acknowledgments We would like to thank the Kavli Nanolab Delft for nanofabrication assistance. This work is financially supported by the European Research Council (ERC CoG Q-ECHOS, 101001005) and is part of the research program of the Netherlands Organization for Scientific Research (NWO), supported by the NWO Frontiers of Nanoscience program, as well as through a Vrij Programma (680-92-18-04) grant.

Conflict of interests: The authors declare no competing interests.

Author contributions: A.Z., L.S., N.F. and S.G. devised and planned the experiment. A.Z., N.F. M.J., R.B. simulated and designed the device. A.Z. and L.S. fabricated the sample, A.Z., L.S. and N.F. built the setup and performed the measurements. A.Z., L.S., and S.G. analyzed the data and wrote the manuscript with input from all authors. E.V. and S.G. supervised the project.

Data Availability: Source data for the plots will be made available on Zenodo.

4.6. SUPPLEMENTARY INFORMATION

SIMULATION

In Fig. 4.5, we show the mechanical simulation of the whole structure and the calculated optomechanical single photon coupling rate g_0 for different symmetric and anti-symmetric supermodes. The mechanical spectrum is a series of Fabry-Pérot modes, equally spaced by $\Delta\nu_{\text{FRS}}$, given by the hybridization of the single mode of the cavity with the series of modes supported by the free-ending waveguide. Each Fabry-Pérot mode is split by $\Delta\nu_{\text{NMS}}$ into a doublet due to the mechanical coupling between the two waveguides. The mode profiles corresponding to one of the doublets are shown in green and red boxes in Fig. 4.5. Note that these simulations use a shorter device length compared to the measured device, for faster computational run-times, which results in different $\Delta\nu_{\text{NMS}}$ and $\Delta\nu_{\text{FRS}}$.

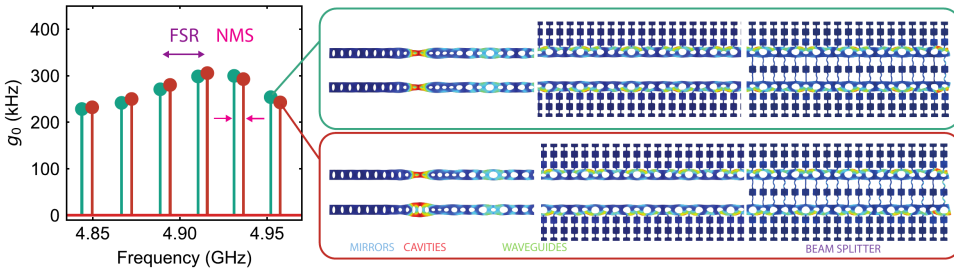


Figure 4.5: Simulation of the whole structure for a device with 50 unit cell of directional coupler and about $80\ \mu\text{m}$ total length (shorter than the measured device in the main text, for a faster simulation time). Left: calculated single photon optomechanical coupling rate for symmetric (green) and anti-symmetric (red) modes - for each Fabry-Pérot mode, the symmetric and anti-symmetric modes form a doublet split by $\Delta\nu_{\text{NMS}}$ due to the phononic coupling between the top and bottom waveguides. Right: mechanical mode profiles corresponding to one of the doublets. The whole structure is reported in segments for space reason.

FABRICATION

The device is fabricated from a silicon-on-insulator (SOI) wafer with a 250 nm thick silicon device layer on top of $3\ \mu\text{m}$ of buried oxide. We use electron beam lithography to pattern the structure and transfer the mask with a dry HBr/Ar plasma etch. After processing, the chip is diced in order to access the device's optical waveguide with a lensed fiber in the dilution refrigerator. We then remove any remaining resist using 80° Dimethylformamide. Finally, the device is cleaned with a piranha solution and released using a 40% hydrofluoric acid (HF) wet etch to remove the buried oxide layer [20]. In order to minimize oxidation, the device is immediately transferred into the dilution refrigerator.

Since we use a wet etch process to undercut the samples, we need to have very robust nanostructure. To achieve this, we use a thin ($<50\ \text{nm}$ wide) tether to connect the central optical waveguide (shared between the two cavities) and the optomechanical resonators. We report that using two sets of clamps on the optical waveguide (spaced by $\sim 10\ \mu\text{m}$) without the tether gives a yield of $\sim 70\%$. We report no significant changes in the mechanical spectrum with or without the thin tether.

LIFETIME

In order to measure the mechanical lifetime T_1 of our devices, we send a sequence of two red-detuned pulses with varying delays Δt_{ro} . The first one is a strong pulse, used to heat our device through residual optical absorption, creating a large thermal population in the mechanical mode. The second pulse is weaker, allowing us to read the mechanical population after a variable delay from the first pulse. The results are shown in Fig. 4.6 for both devices (A in blue and B in orange). As previously studied, the curves follow a double exponential decay [18]. We measure values of $T_1 \approx 3.0 \mu\text{s}$ and $1.2 \mu\text{s}$ for cavity A and B, respectively. These values are much longer than the typical round-trip time of the phononic wavepackets. They can be increased to several ms by adding additional phononic shield periods both at the waveguides' support part and the left end of the mirror side (blue part in Fig. 4.1e), and values up to 5.5 ms have been reported previously [16, 19, 38]. We intentionally design and choose a device with short mechanical lifetime to increase the repetition rate of the experiment. The rise in the thermal population for short delays ($\Delta t_{ro} < 100 \text{ ns}$) is given by the delayed absorption [20].

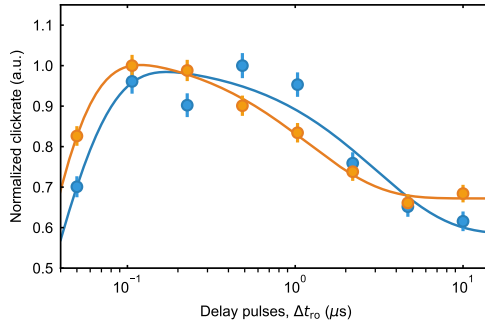


Figure 4.6: Normalized clickrates measured by the second probe pulse given by the thermally excited mechanical mode as a function of delay time Δt_{ro} between pulses, for device A (blue) and B (orange). The population exhibits a double exponential behavior, given by the delayed absorption heating and the population decay. The measured lifetimes of the two cavities are $T_1 \approx 3.0 \mu\text{s}$ and $1.2 \mu\text{s}$ for cavity A and B, respectively.

THERMAL OCCUPATION OF MECHANICAL STATE

The GHz mechanical excitations have in principle a thermal occupation of $< 10^{-5}$ at mK temperatures. However, due to optical absorption of the pump laser in the device, a thermal mechanical population inside the cavity is created, and thus the thermal occupation of the mechanical mode is typically significantly higher. We measure the equivalent thermal occupation of the mechanical mode using the sideband thermometry technique [16, 19, 20]. In particular, we send alternating blue-detuned and red-detuned pulses with equal energies (equal scattering probability), and use the click rates measured from both pulses to obtain the thermal occupation at the mode of interest [20]. We repeat this measurement with different pulse energies (varying the scattering probability). In this way we measure the amount of heating and thermal occupation induced by one single pulse in different cavities. The results are shown in Fig. 4.7a for device A

and Fig. 4.7b for device B. Furthermore, we measure the thermal occupation in a two pulse sequence scheme, as it is used in our final experiment (see Fig. 4.4), using the same technique with an additional red-detuned pre-pulse, 115 ns before the pulses used to measure the thermal occupation. This red-detuned pre-pulse is used to mimic the heating of the blue pulse in the experiment. In this measurement we keep the energy of the sideband asymmetry pulses constant and equal to the value that we use in the actual experiment (280 fJ, scattering probabilities 1.2 % (2 %) for cavity A (B)), and only vary the energy of the pre-pulse. We repeat this measurement in different combinations of sending the pre-pulse to a cavity (A or B) and measure the thermal occupation of one of the cavities (A or B). The results for different combinations are shown in Fig. 4.7c-f. These measurements show that by sending a pulse to one cavity, not only do we heat that cavity, but some of the thermal energy also heats the other cavity through the beam splitter. This is clearly visible from the linear increase of the thermal population with the scattering probability of the pre-pulse and by the higher thermal population compared to the single pulse case (as in Fig. 4.7a and b). Note that, since the cavities have optical resonances spaced by much more than the optical linewidth and the mechanical frequencies of interest, the optical pulses that address one cavity does not interact at all with the other, causing no direct heating. For the pulse energies used in the actual experiment, we measure $n_{th,AA} \approx 0.18$, $n_{th,AB} \approx 0.17$, $n_{th,BA} \approx 0.14$ and $n_{th,BB} \approx 0.17$.

SETUP

A sketch of the experimental setup is depicted in Fig. 4.8. We use two continuous-wave lasers for write and read operations, whose frequencies are locked using feedback from a wavelength meter. We then filter the GHz noise of the lasers using fiber filters. Both lasers are pulsed by gating 110 MHz acousto-optic modulators (AOMs) with a digital pulse generator (P400). The two lines are combined on a polarized beam splitter (PBS1), and we use fiber polarization controllers (FPCs) on each line to maximize transmission through PBS1. After combination, the pulses are sent into a lensed fiber at the mixing chamber of the dilution refrigerator, coupling the optical fields into the device. The coupling efficiency from the fiber to the central optical waveguide (yellow part in Fig. 4.1e) is $\eta_c \approx 40\%$. The reflected light from the device is routed to free-space filter cavities (F1 and F2) using a circulator, in order to filter the write and read pump pulses with suppression ratio of 94 dB for F1 and 96 dB for F2. The efficiency of the filter setup for the Stokes and anti-Stokes scattered photons is $\eta_f \approx 30\%$. When we write on one device and read the same (AA or BB combinations), using one filter cavity (F1) suffices for our detection. However, when we write on one device and read the opposite device (AB or BA combinations), we need to use both filter setups (F1 and F2), since the devices have resonances at different wavelengths. In this scheme, F1 is locked on resonance of one device (A or B) while F2 is locked to the other resonance (B or A). The anti-Stokes optomechanically scattered photon from the read pulse passes through F1, while all the pumps and the Stokes photon are reflected back into fiber. The light is routed to F2 using a circulator which suppresses all pump fields and only allows the Stokes photon to pass. Every 8 s the measurement is paused and locking lasers are sent to the cavities to lock them simultaneously. We use two EOMs to create sidebands at the resonances wavelengths using light from the read laser and from the write laser to lock F1 and F2, respectively. We merge both signals from F1 and F2 on a polarizing beam splitter (PBS), and use FPCs

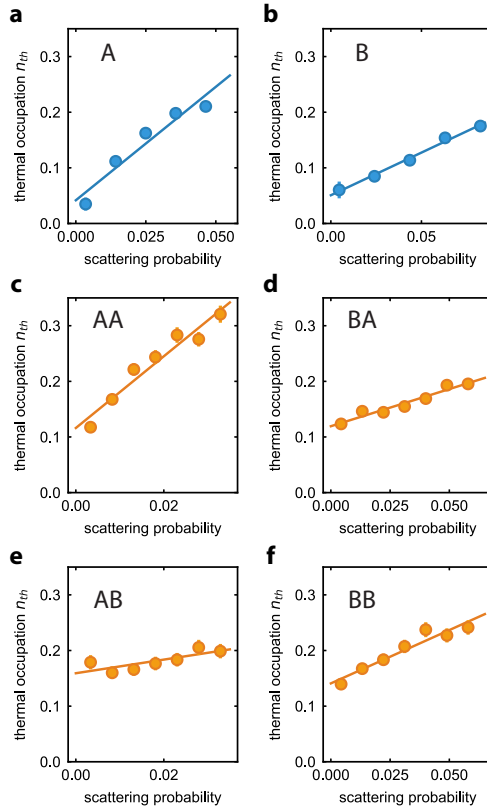


Figure 4.7: a,b) Thermal occupation of device A and B using a single pulse scheme versus the scattering probability of the pulse. c-f) Thermal occupation of device A and B in a two pulse sequence scheme, mimicking the realistic case of the experiment, versus the scattering probability of the pre-pulse. The pre-pulse is sent to one of the cavities, and the thermal occupation of either the same cavity or the opposite cavity is measured. Different combinations are specified with the two letters at the top left corner of each plot, with the first letter indicating the cavity that the pre-pulse is sent to, and the second letter the cavity that is measured.

to maximize transmission of each signal through the PBS. We send the output of PBS to a SNSPD installed on the quasi 1 K stage of our dilution refrigerator. Since the filters are being locked to two different wavelengths, we observe relatively high leakage from the pump lasers of opposite wavelength – the write laser pump leaks through F1 and the read laser pump leaks through F2. This is because the suppression of the filter setup depends heavily on the detuning between the filter resonances and the laser wavelength. Given the (fixed) free spectral range of the filter cavities, the opposite laser can have a smaller detuning and so smaller suppression compared to the laser used to lock the cavity. We found that, for the cavities and wavelengths used in the experiments, the leakage through F1 of the write laser is $\sim 10^{-4}$ clicks on repetition (approximately 3 times higher than the clickrate from the write pulse passing through F2), and the ones from F2 of the read laser are $\sim 10^{-5}$ clicks on repetition (approximately 1/3 of the clickrate from the read

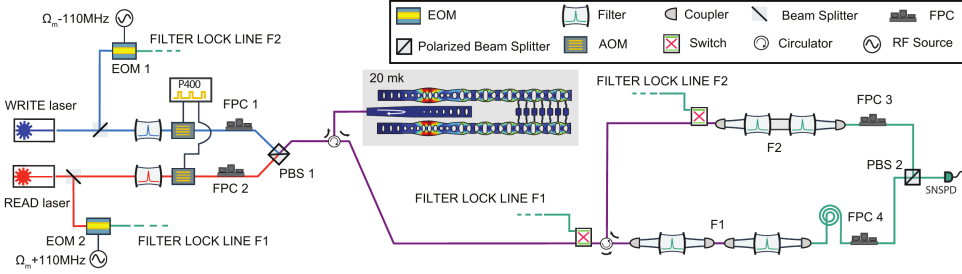


Figure 4.8: Detailed sketch of the experimental setup. P400 is the digital pulse generator to create pulses on the acousto-optic modulators (AOMs). EOMs are electro-optic modulators, BS the beam splitter, PBS the polarized beam splitter, FPC the fiber polarization controller and SNSPD the superconducting nanowire single photon detector. Ω_m is the mechanical central frequency (5.31 GHz). We have two sets of free-space detection filters F1 and F2, in order to distinguish the light from different devices A and B, when we excite and read different cavities (see the text for more details).

pulse passing through F1). In order to temporally distinguish between the leakage of the pump lasers and the actual Stokes and anti-Stokes scattered photons coming out of the filter setup outputs, we delay the signal of F1 (the one we use for reading) by 320 ns. In this way, the leakages are spaced in time from the Stokes and anti-Stokes photons more than the recovery time of the SNSPDs, and they do not affect the measurement results.

COHERENT DRIVE MEASUREMENT

For the coherent drive measurement, we first gather the click rates given by our quasi-continuous red-detuned read laser. Because of the optical absorption of the device, the reading laser creates some thermal occupation in the cavity as well. To independently calibrate this background and measure only the coherent population of our cavities, we run a measurement with the same reading power on both cavities, without the coherent excitation pulse. This gives us the thermal background induced by the reading laser, which we then subtract from the original data. In order to calculate the normalized phononic population, we first normalize the click rates by the maximum click rates we get from the excitation pulse (the peak at zero time delay). We also normalize the click rates with the optomechanical coupling rate g_0 , as well as the extrinsic optical couplings $\kappa_e = \kappa - \kappa_i$ of each cavity. In this way, we normalize the phononic population with the phononic excitation and read-out efficiency.

The measurements for devices with 25 and 100 unit cells in the beam splitter are shown in Fig. 4.9 for different exciting and reading combinations. As can be clearly seen, the 25 unit cell device (green) shows behavior of a 80 % transmissive beam splitter, whereas the 100 unit cell device (orange) of a beam splitter with almost 100 % reflectivity. This behavior follows our simulations very closely. The decay in the overall population is mainly caused by dispersion of the waveguides and beam splitters, coming from fabrication disorders, as well as residual phononic dissipation.

TWO PHOTON CROSS CORRELATION $g_{om}^{(2)}$ VERSUS TIME

In order to measure the two photon cross correlation of the phononic wavepackets, we use a technique similar to [16] to filter out coincidences in time with finer resolution.

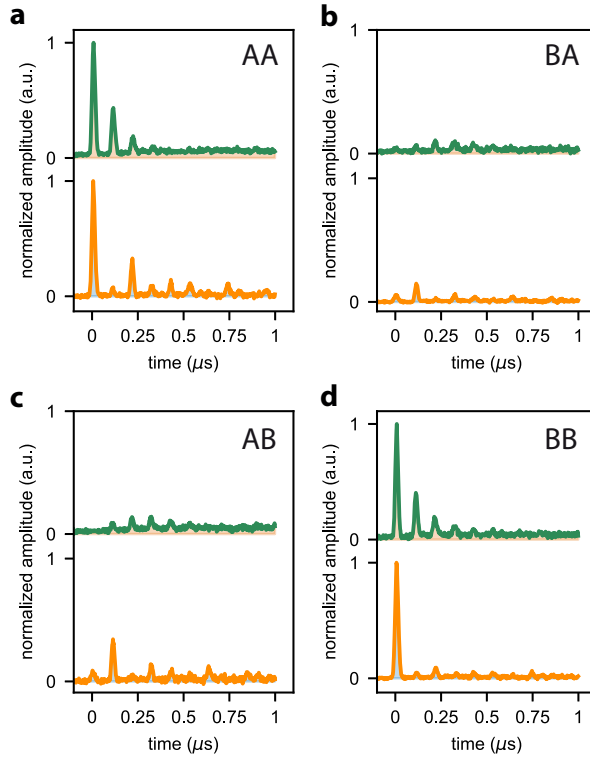


Figure 4.9: Normalized coherent phononic population of each cavity when either the same cavity (a and d) or opposite cavities (b and c) are excited. The green (orange) plot on top (bottom) corresponds to a device consisting of 25 (100) unit cells in the phononic coupler region.

This allows us to obtain the time domain behavior of the phononic packet. The results for different combinations of the excite and read cavities are shown in Fig. 4.10. The correlation value increases from uncorrelated (1) or classical correlation (2) to non-classical (>2) value as the phononic wavepacket returns back to the optomechanical cavity, and again drops down to classical correlation (2) and eventually uncorrelated values as the packet leave the cavity to the phononic waveguide again.

4.7. APPENDIX

In this appendix we report some facts and some *a posteriori* consideration on the experiment reported in this chapter. The idea is to give insights on the challenges encountered on the path to acquire the final dataset.

- In the design of photonic/phononic crystal structures, consisting regions with different parameters, having an adiabatic change between the parameters is an important consideration in order to not have reflections and impedance mismatch at the interfaces. As an example, in the studied device architecture, having similar

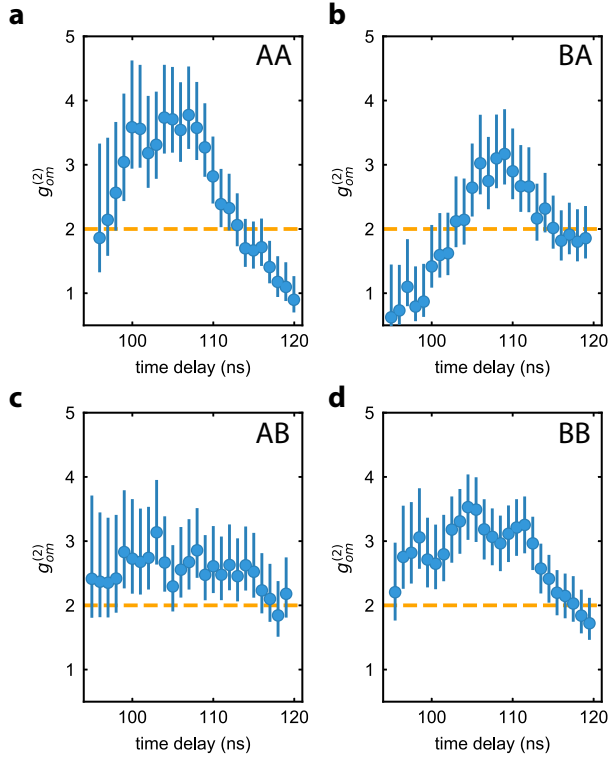


Figure 4.10: The two-photon cross correlation $g_{om}^{(2)}$ behavior in time for the 50:50 beam splitter device. The orange dashed line indicates the classical boundary of 2.

hole size in the phononic waveguide part and the directional coupler is crucial, to minimize the reflection at the interface of the two and obtain a clean mechanical spectrum with constant FSR and NMS.

- Having a broad bandwidth on the unit cell simulations, is important in order to increase the yield of the fabricated devices and overcome the perturbations caused fabrication disorders. We statistically find that the mechanical frequency and features may deviate by ± 150 MHz from the simulations after fabricating devices. This deviation comes from both fabrication uncertainties, as well as other deviations (such as thickness) in the silicon wafers that we use.
- Simulating a device more than $100 \mu\text{m}$ requires a strong hardware in order to not have too long simulation time. For all the simulations, we simulate devices shorter than $90 \mu\text{m}$ in order to have a sensible simulation time. However, the simulated device should be long enough to have the waveguide length much longer than the optomechanical cavity part and the lead waveguide part (for more details see 3.5).
- Before the cooldown, we first perform simple characterization of our fabricated

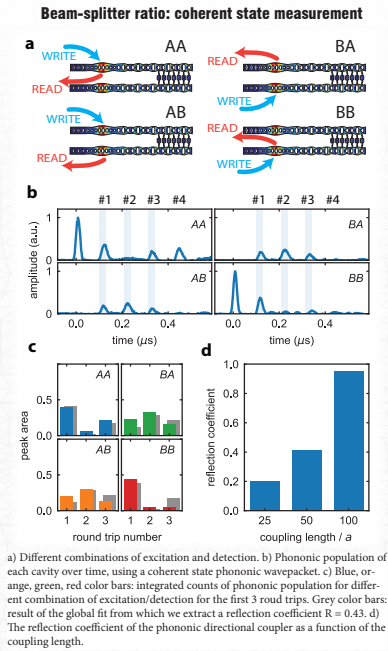
devices in room temperature and ambient pressure, so check the optical and mechanical spectrum. However, because of the broad features of mechanical peaks in room temperature and ambient conditions, the mechanical peaks that are less than 5 MHz distant are not resolvable in the spectrum of the devices. Therefore, for the basic characterization of the chip in these conditions, we always fabricate shorter devices (with larger FSR and NMS), matching our simulated version of the device, in order to be able to visualize the NMS and FSR. After this checks, we cooldown and measure the longer devices in mK temperatures.

REFERENCES

- [1] F. Arute et al., Quantum supremacy using a programmable superconducting processor, *Nature* **574**, 505 (2019).
- [2] H.-S. Zhong, H. Wang, Y.-H. Deng, M.-C. Chen, L.-C. Peng, Y.-H. Luo, J. Qin, D. Wu, X. Ding, Y. Hu, P. Hu, X.-Y. Yang, W.-J. Zhang, H. Li, Y. Li, X. Jiang, L. Gan, G. Yang, L. You, Z. Wang, L. Li, N.-L. Liu, C.-Y. Lu, and J.-W. Pan, Quantum computational advantage using photons, *Science* **370**, 1460 (2020).
- [3] J.-G. Ren, P. Xu, H.-L. Yong, L. Zhang, S.-K. Liao, J. Yin, W.-Y. Liu, W.-Q. Cai, M. Yang, L. Li, K.-X. Yang, X. Han, Y.-Q. Yao, J. Li, H.-Y. Wu, S. Wan, L. Liu, D.-Q. Liu, Y.-W. Kuang, Z.-P. He, P. Shang, C. Guo, R.-H. Zheng, K. Tian, Z.-C. Zhu, N.-L. Liu, C.-Y. Lu, R. Shu, Y.-A. Chen, C.-Z. Peng, J.-Y. Wang, and J.-W. Pan, Ground-to-satellite quantum teleportation, *Nature* **549**, 70 (2017).
- [4] M. Wallquist, K. Hammerer, P. Rabl, M. Lukin, and P. Zoller, Hybrid quantum devices and quantum engineering, *Phys. Scr.* **T137**, 014001 (2009).
- [5] G. Kurizki, P. Bertet, Y. Kubo, K. Mølmer, D. Petrosyan, P. Rabl, and J. Schmiedmayer, Quantum technologies with hybrid systems, *Proc. Natl. Acad. Sci.* **112**, 3866 (2015).
- [6] H. J. Kimble, The quantum internet, *Nature* **453**, 1023 (2008).
- [7] P. Delsing *et al.*, The 2019 surface acoustic waves roadmap, *J. Phys. D: Appl. Phys.* **52**, 353001 (2019).
- [8] S. Barzanjeh, A. Xuereb, S. Gröblacher, M. Paternostro, C. A. Regal, and E. M. Weig, Optomechanics for quantum technologies, *Nature Physics* **18**, 15 (2022).
- [9] M. Mirhosseini, A. Sipahigil, M. Kalaei, and O. Painter, Superconducting qubit to optical photon transduction, *Nature* **588**, 599 (2020).
- [10] W. Jiang, C. J. Sarabalis, Y. D. Dahmani, R. N. Patel, F. M. Mayor, T. P. McKenna, R. Van Laer, and A. H. Safavi-Naeini, Efficient bidirectional piezo-optomechanical transduction between microwave and optical frequency, *Nature Commun.* **11**, 1166 (2020).
- [11] M. J. Weaver, P. Duivestijn, A. C. Bernasconi, S. Scharmer, M. Lemang, T. C. v. Thiel, F. Hijazi, B. Hensen, S. Gröblacher, and R. Stockill, An integrated microwave-to-optics interface for scalable quantum computing, *Nature Nanotechnol.* [10.1038/s41565-023-01515-y](https://doi.org/10.1038/s41565-023-01515-y) (2023).
- [12] F. Fogliano, B. Besga, A. Reigue, L. Mercier de Lépinay, P. Heringlake, C. Gouriou, E. Eyraud, W. Wernsdorfer, B. Pigeau, and O. Arcizet, Ultrasensitive nano-optomechanical force sensor operated at dilution temperatures, *Nature Commun.* **12**, 4124 (2021).
- [13] A. Bienfait, K. J. Satzinger, Y. P. Zhong, H.-S. Chang, M.-H. Chou, C. R. Conner, E. Dumur, J. Grebel, G. A. Peairs, R. G. Povey, and A. N. Cleland, Phonon-mediated quantum state transfer and remote qubit entanglement, *Science* **364**, 368 (2019).

- [14] A. Bienfait, Y. P. Zhong, H. S. Chang, M. H. Chou, C. R. Conner, Dumur, J. Grebel, G. A. Peairs, R. G. Povey, K. J. Satzinger, and A. N. Cleland, Quantum Erasure Using Entangled Surface Acoustic Phonons, *Phys. Rev. X* **10**, 21055 (2020).
- [15] R. P. G. McNeil, M. Kataoka, C. J. B. Ford, C. H. W. Barnes, D. Anderson, G. A. C. Jones, I. Farrer, and D. A. Ritchie, On-demand single-electron transfer between distant quantum dots, *Nature* **477**, 439 (2011).
- [16] A. Zivari, R. Stockill, N. Fiaschi, and S. Gröblacher, Non-classical mechanical states guided in a phononic waveguide, *Nature Phys.* **18**, 789 (2022).
- [17] H. Qiao, É. Dumur, G. Andersson, H. Yan, M.-H. Chou, J. Grebel, C. Conner, Y. Joshi, J. Miller, R. Povey, *et al.*, Splitting phonons: Building a platform for linear mechanical quantum computing, *Science* **380**, 1030 (2023).
- [18] A. Wallucks, I. Marinković, B. Hensen, R. Stockill, and S. Gröblacher, A quantum memory at telecom wavelengths, *Nat. Phys.* **16**, 772 (2020).
- [19] A. Zivari, N. Fiaschi, R. Burgwal, E. Verhagen, R. Stockill, and S. Gröblacher, On-chip distribution of quantum information using traveling phonons, *Sci. Adv.* **8**, eadd2811 (2022).
- [20] R. Riedinger, S. Hong, R. A. Norte, J. A. Slater, J. Shang, A. G. Krause, V. Anant, M. Aspelmeyer, and S. Gröblacher, Non-classical correlations between single photons and phonons from a mechanical oscillator, *Nature* **530**, 313 (2016).
- [21] S. Hong, R. Riedinger, I. Marinković, A. Wallucks, S. G. Hofer, R. A. Norte, M. Aspelmeyer, and S. Gröblacher, Hanbury Brown and Twiss interferometry of single phonons from an optomechanical resonator, *Science* **358**, 203 (2017).
- [22] R. Riedinger, A. Wallucks, I. Marinković, C. Löschnauer, M. Aspelmeyer, S. Hong, and S. Gröblacher, Remote quantum entanglement between two micromechanical oscillators, *Nature* **556**, 473 (2018).
- [23] I. Marinković, A. Wallucks, R. Riedinger, S. Hong, M. Aspelmeyer, and S. Gröblacher, An optomechanical Bell test, *Phys. Rev. Lett.* **121**, 220404 (2018).
- [24] N. Fiaschi, B. Hensen, A. Wallucks, R. Benevides, J. Li, T. P. M. Alegre, and S. Gröblacher, Optomechanical quantum teleportation, *Nature Photon.* **15**, 817 (2021).
- [25] E. Knill, R. Laflamme, and G. J. Milburn, A scheme for efficient quantum computation with linear optics, *Nature* **409**, 46 (2001).
- [26] J. Wang, F. Sciarrino, A. Laing, and M. G. Thompson, Integrated photonic quantum technologies, *Nat. Photonics* **14**, 273 (2020).
- [27] X. Liu, A. W. Bruch, and H. X. Tang, Aluminum nitride photonic integrated circuits: from piezo-optomechanics to nonlinear optics, *Adv. Opt. Photonics* **15**, 236 (2023).

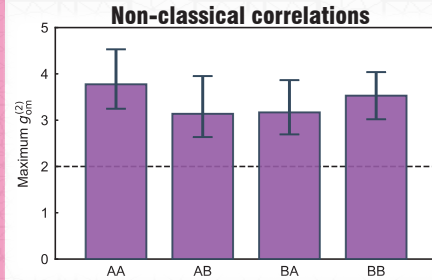
- [28] Y. Wang, J. A. Holguín-Lerma, M. Vezzoli, Y. Guo, and H. X. Tang, Photonic-circuit-integrated titanium: sapphire laser, *Nat. Photonics* **17**, 338 (2023).
- [29] K. Fang, M. H. Matheny, X. Luan, and O. Painter, Optical transduction and routing of microwave phonons in cavity-optomechanical circuits, *Nature Photon.* **10**, 489 (2016).
- [30] R. N. Patel, Z. Wang, W. Jiang, C. J. Sarabalis, J. T. Hill, and A. H. Safavi-Naeini, Single-mode phononic wire, *Phys. Rev. Lett.* **121**, 040501 (2018).
- [31] G. Madiot, R. C. Ng, G. Arregui, O. Florez, M. Albrechtsen, S. Stobbe, P. D. García, and C. M. Sotomayor-Torres, Optomechanical generation of coherent GHz vibrations in a phononic waveguide, *Phys. Rev. Lett.* **130**, 106903 (2023).
- [32] S. Weis, R. Rivière, S. Deléglise, E. Gavartin, O. Arcizet, A. Schliesser, and T. J. Kippenberg, Optomechanically Induced Transparency, *Science* **330**, 1520 (2010).
- [33] W. Fu, Z. Shen, Y. Xu, C.-L. Zou, R. Cheng, X. Han, and H. X. Tang, Phononic integrated circuitry and spin-orbit interaction of phonons, *Nature Commun.* **10**, 2743 (2019).
- [34] W. Jiang, F. M. Mayor, S. Malik, R. Van Laer, T. P. McKenna, R. N. Patel, J. D. Witmer, and A. H. Safavi-Naeini, Optically heralded microwave photon addition, *Nature Phys.* **19**, 1423 (2023).
- [35] J. C. Taylor, E. Chatterjee, W. F. Kindel, D. Soh, and M. Eichenfield, Reconfigurable quantum phononic circuits via piezo-acoustomechanical interactions, *npj Quantum Inf.* **8**, 19 (2022).
- [36] H. Tian, J. Liu, A. Siddharth, R. N. Wang, T. Blésin, J. He, T. J. Kippenberg, and S. A. Bhave, Magnetic-free silicon nitride integrated optical isolator, *Nat. Photon.* **15**, 828 (2021).
- [37] C. Spinnler, G. N. Nguyen, Y. Wang, M. Erbe, A. Javadi, L. Zhai, S. Scholz, A. D. Wieck, A. Ludwig, P. Lodahl, L. Midolo, and R. J. Warburton, A quantum dot coupled to a suspended-beam mechanical resonator: from the unresolved- to the resolved-sideband regime, *arXiv:2311.05353* (2023).
- [38] J. Chan, A. H. Safavi-Naeini, J. T. Hill, S. Meenehan, and O. Painter, Optimized optomechanical crystal cavity with acoustic radiation shield, *App. Phys. Lett.* **101**, 081115 (2012).



Abstract

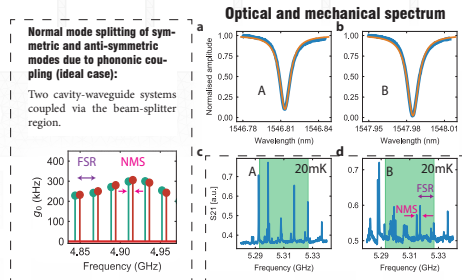
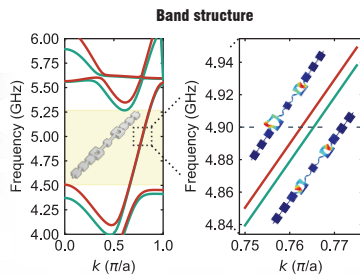
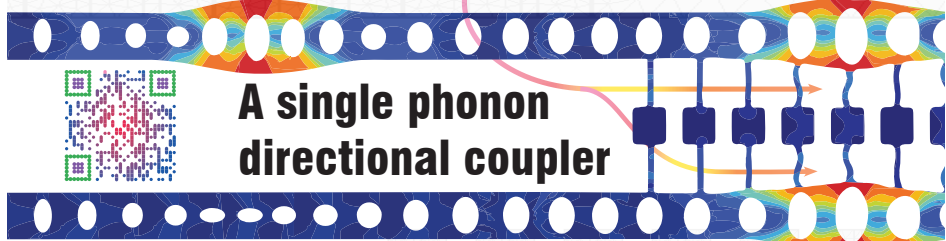
We demonstrate for the first time a 4-port directional coupler for quantum mechanical excitations – a crucial component for integrated phononic circuits.

Adjusting the length of the coupling region allows to realize phononic beam splitters with varying splitting ratios. By sending a single-phonon Fock state onto one of these phononic splitters, we demonstrate the capability of using the directional coupler directly in the quantum regime.



50:50 splitting of a single phonon Fock state

Second order correlation between Stokes and anti-Stokes scattered photons from write and read pulses. All values are above the classical threshold of 2.



Amirparsa Zivari*, Niccolò Fiaschi*, Lorenzo Scarpelli*, Menno Jansen, Roel Burgwal, Ewold Verhagen, and Simon Gröblacher

TU Delft

ERC NWO
KAVLI INSTITUTE
FOR NANOSCIENCE DUTCH

Poster for the paper Amirparsa Zivari*, Niccolò Fiaschi*, Lorenzo Scarpelli*, Menno Jansen, Roel Burgwal, Ewold Verhagen, and Simon Gröblacher, *A single-phonon directional coupler*, arXiv preprint arXiv:2312.04414 (2023)

5

CONCLUSION

"Knowledge is a deadly friend, if no one sets the rules"

[King Crimson - Epitaph]

In this thesis, we presented a platform based on routing highly confined GHz phonons for hybrid quantum networks and processors. This platform is scalable and can be used to integrate with different types of quantum systems such as photons (optomechanics) and superconducting qubits potentially. The use of GHz phonons, makes it possible to reach quantum ground state by passively cooling down the fabricated chip in a dilution refrigerator. Moreover, high frequency phonons have proven to be perfect intermediaries to couple different quantum systems, as they can efficiently couple to various quantum systems such as photons, superconducting and solid state qubits. The millisecond long lifetime of highly confined phonons in these structures, makes them robust against decoherence and is promising for quantum memory applications. Furthermore, highly confined phonons are perfect candidates for making scalable quantum devices with small foot-print. Our devices are suspended silicon structures with thickness of 250 nm with lateral extension of about only a few μm . The lateral extension includes the phononic structures that we use to support our phononic waveguides and simultaneously protect the 5 GHz phonons from dissipating into the silicon thin film. The actual size of our phononic waveguide is only 530 nm.

We started with the first step of routing confined single phonons in quasi 1D structure of phononic crystal waveguides in 2. The platform consists of an optomechanical cavity, which we use as a source and detector for phonons, coupled to a phononic waveguide. We showed that we can efficiently excite, route, and capture single mechanical excitations with our device. We also showed that this device can, in principle, be used for time-multiplexing quantum information and be used as a multimode optomechanical quantum memory.

Afterwards, in chapter 3 we improved the design of our phononic waveguide, as well as our fabrication recipe, leading to a significantly better quantum performance and reproducibility. We used this platform, to entangle two traveling phonons in time using

optomechanical heralding, and then showed the quantum nature of the system by violating Bell inequality. The findings of this chapter, strongly proves that this platform can be employed to route quantum information - i.e. a traveling entangled state - on chip, useful for realizing hybrid quantum devices on a chip at a node of a quantum network. The optomechanical Bell-test further promises that this platform can be used as a multimode quantum memory as well.

In chapter 4, we move one step closer towards having a complete on-chip platform for having full coherent control over single phonons. In this work, we realized a phononic directional coupler, measured and characterized it in both classical and quantum regime. Directional couplers are useful for creating entanglement on a chip between different spots. They can also be employed for classical applications such as information and power multiplexing. We showed that the splitting ratio can be varied by changing the coupler length and measured splitting of a coherent state of phonons for devices with different coupler length. We further proved single phonon splitting using a 50:50 beam splitter device.

With all these building blocks together, in this thesis we developed parts of a toolbox for having a full coherent control over highly confined mechanical vibrations on a chip. That would include phononic waveguides for routing, and phononic directional couplers for multiplexing. These platforms together with a phononic phase shifter, complete the toolbox for any on-chip quantum acoustic experiments and linear mechanical quantum operations. Our designs can also be integrated with other types of quantum systems, such as superconducting qubits without any major modification.

We use optomechanical interaction as a technique to excite and detect mechanical excitation in our devices. This process is highly probabilistic because of the weak phonon-photon interaction at low laser powers. While the excitation laser is kept low in order to avoid multi-phonon excitations, the reading laser power can be increased (which essentially increases the optomechanical coupling strength) to have a deterministic reading. However, due to the optical absorption in silicon devices, higher laser power leads to larger thermal heating of the device and eventually larger thermal phonon occupation, deviating from the ground state condition. This heating process is dominated by the defects on the surface of the silicon, created by dangling free bonds after fabrication that causes oxidation of the silicon surface [1, 2]. Therefore, this issue can be overcome, by doing further surface treatment and passivation of silicon devices [3]. Another alternative to improve the optical absorption and quantum performance is using 2D silicon structures, that are designed to dissipate thermal energy into the substrate of the material [4]. These structures tolerate more laser power, without deviating much from the mechanical ground state. While all these systems still rely on optomechanical interactions, one could replace the optomechanical cavity with a piezo resonator connected to a superconducting qubit [5]. In this way, strong coupling between the superconducting qubit and the phonons can be achieved. By utilizing the nonlinearity of superconducting qubits, deterministic excitation and detection processes can be obtained [6, 7].

REFERENCES

- [1] S. M. Meenehan, J. D. Cohen, S. Gröblacher, J. T. Hill, A. H. Safavi-Naeini, M. Aspelmeyer, and O. Painter, Silicon optomechanical crystal resonator at millikelvin temperatures, *Phys. Rev. A* **90**, 011803 (2014).
- [2] L. Qiu, I. Shomroni, P. Seidler, and T. J. Kippenberg, Laser cooling of a nanomechanical oscillator to its zero-point energy, *Phys. Rev. Lett.* **124**, 173601 (2020).
- [3] M. Borselli, T. J. Johnson, and O. Painter, Measuring the role of surface chemistry in silicon microphotronics, *Appl. Phys. Lett.* **88**, 131114 (2006).
- [4] H. Ren, M. H. Matheny, G. S. MacCabe, J. Luo, H. Pfeifer, M. Mirhosseini, and O. Painter, Two-dimensional optomechanical crystal cavity with high quantum cooperativity, *Nature Communications* 2020 11:1 **11**, 1 (2020), [arXiv:1910.02873](https://arxiv.org/abs/1910.02873).
- [5] M. Mirhosseini, A. Sipahigil, M. Kalaei, and O. Painter, Superconducting qubit to optical photon transduction, *Nature* **588**, 599 (2020).
- [6] K. J. Satzinger, Y. P. Zhong, H.-S. Chang, G. A. Peairs, A. Bienfait, M.-H. Chou, A. Y. Cleland, C. R. Conner, E. Dumur, J. Grebel, I. Gutierrez, B. H. November, R. G. Povey, S. J. Whiteley, D. D. Awschalom, D. I. Schuster, and A. N. Cleland, Quantum control of surface acoustic-wave phonons, *Nature* **563**, 661 (2018).
- [7] A. Bienfait, K. J. Satzinger, Y. P. Zhong, H.-S. Chang, M.-H. Chou, C. R. Conner, E. Dumur, J. Grebel, G. A. Peairs, R. G. Povey, and A. N. Cleland, Phonon-mediated quantum state transfer and remote qubit entanglement, *Science* **364**, 368 (2019).

CURRICULUM VITÆ

AMIRPARSA ZIVARI

14-02-1995 Born in Tehran, Iran.

EDUCATION

- 2013–2017 **B.Sc. in Electrical Engineering**
Sharif University of Technology, Tehran, Iran
Thesis: Imaging with millimeter waves
Promotor: Dr. Amin Khavasi
- 2017–2019 **M.Sc. in Electrical Engineering - Photonics & Optical communication**
Sharif University of Technology, Tehran, Iran
Thesis: Design and study of lenses with resolution beyond the diffraction limit
Promotor: Prof. dr. Behzad Rejaei
Promotor: Dr. Amin Khavasi
- 2020–2024 **PhD. Physics**
Delft University of Technology, the Netherlands
Thesis: A journey on quantum sound: developing a scalable platform for integrated hybrid quantum devices
Promotor: Prof. dr. Simon Gröblacher
Promotor: Prof. dr. Laurens Kuipers

LIST OF PUBLICATIONS

5. **Amirparsa Zivari***, Niccolò Fiaschi*, Lorenzo Scarpelli*, Menno Jansen, Roel Burgwal, Ewold Verhagen, and Simon Gröblacher, *A single-phonon directional coupler, in submission*, [arXiv:2312.04414](https://arxiv.org/abs/2312.04414).
4. **Amirparsa Zivari***, Niccolò Fiaschi*, Roel Burgwal, Ewold Verhagen, Robert Stockill, and Simon Gröblacher, *On-chip distribution of quantum information using traveling phonons*, *Science Advances* Vol 8, Issue 46 (2022).
3. **Amirparsa Zivari**, Robert Stockill, Niccolò Fiaschi and Simon Gröblacher, *Non-classical mechanical states guided in a phononic waveguide*, *Nat. Phys.* 18, 789–793 (2022).
2. **Amirparsa Zivari**, Mohammad Reza Tavakol, Amin Khavasi, and Behzad Rejaei, *Terahertz lensing effect in high-temperature superconductors*, *JOSA B* 36, no. 5 (2019): 1241-1245.
1. **Amirparsa Zivari**, Amirmasood Bagheri, Behzad Rejaei, and Amin Khavasi, *Propagation and refraction of left-handed plasmons on a semiconducting substrate covered by graphene*, *Optics Letters* 43, no. 9 (2018): 2010-2013.

* Indicates equal contribution

ACKNOWLEDGEMENTS

"I wanted you to know

You've always shared my deepest thoughts

You follow where I go"

- [Alan Parsons - Old and wise]

And here it goes the real journey!

To all those who accompanied me throughout this remarkable journey – words cannot express how grateful I am for your help and support.

First and foremost, I'd like to thank you **Simon**. When I came across GLAB, it was clear to me from the very beginning that I wanted to be part of this team. Thank you for welcoming me in the group, for having me as your PhD student, for believing in me, for teaching me all the invaluable lessons to become more determined in both life and research, and for always helping me to learn and to grow. It was an awesome experience working in this group. Thank you for your management and the teamwork that you taught all of us. For all the dedication you've shown to our projects, and for your lively and jovial personality. Thanks for giving all the great motivations and clarities when I was down and demotivated. For all the encouragements throughout my whole career, for all the fabulous group trips, conferences, all the fun we had and most importantly, thanks for teaching me how to drink and appreciate good wine! :)

Kobus, you've been great support all these years. I am grateful that I had you as my co-promoter. You have always helped me decide better in my career and PhD life with your advices and supports, and helped me getting calm when I was stressed.

Ewold, during my PhD journey I had the great opportunity to have a lot of collaborations and scientific discussions with you. I learned a lot during all those meetings and conversations here and there in conferences, about our projects and in general about physics. Thanks for all the lessons and feedbacks and comments, helping us developing and studying integrated quantum acoustics. Your wise approach has always been inspiring to me.

Roel and **Menno**, you've been amazing team players and scientist in all the projects we've done, and I'm forever proud of the works we've done together. It's always been wonderful to see you often in conferences Menno, good luck with you PhD, you're doing amazing.

And now, the best group ever, GiiiiLAAAAAAB!

I'll begin with my mentor, tutor, life advisor, and friend, **Rob**. We initiated the quantum acoustics together in this group. When I started my PhD, I was unfamiliar with all the lab and experiments, and you patiently and calmly taught me all those and helped

me with all the projects I did, experimentally, theoretically and most importantly mentally. I still remember our conversation on the stone bench in front of building 22, brainstorming about time-bin phononic entanglement. I enjoyed all the chats and lessons also during our "fresh air" breaks. You wisely guided me through many difficulties that I had, both in scientific and daily life. We worked hard, but was never tiring, thanks to Radiohead playing on the background. You were the best mentor ever! For me it was very easy to connect with you because of the wonderful music passion you have. I feel very lucky that I closely worked with you during my PhD and had your supervision and great supports in all the matters.

Then it goes to my official cleanroom mentor **Moritz**. You were such a hardworking and fun mentor. I am grateful for all the good vibe and energy you've brought and your readiness to help whenever needed. I learned a lot from your scientific attitude and your experiences in cleanroom and lab. Also I should thank my "unofficial" cleanroom mentor **Rodrigo**. Your experience and knowledge has always been impressing to me. I feel very happy that I still see you in conferences and have the chance to talk to you and learn from you.

Bas, your focus, efficiency and intelligence has always been a role model to me. Always ready to help and troubleshoot problems in the lab. You're a great scientist and have a great sense of humor, and I deeply hope to have a chance to work with you again in the future.

Matthijs, for all the great trips together and shared experiences, even the food poisonings! **Pieter** for all the hip-pop songs synchronized with the fridge pulse tubes. **Sezer**, for all the amazing chats, jokes, laughter and integration hints and tricks. You were very understanding and supportive and I really miss your presence in our group! **Max**, you helped me kick off with my projects at the start of my PhD. You were a great tutor, both in cleanroom and lab. Such a beautiful and friendly soul, and thank you for always being keen about my work and all the supports and good feelings and encouragements.

Nicco-mate, we shared most of this journey together. From entanglement, dancing in the lab, crying in the lab, to dancing in Veldhoven, drinking in Ventura, missing the poster in Leiden, our dedication and excitement about the electronics for physicists, complaining about quantum computation course, and I can go on and on. I miss ramming to D112 and ranting about stuff. I will cherish all these wonderful moments we shared. I learned a lot from you!

Nina, we've been close friends for many years now. From the beginning almost. You introduced me to Tazz and their fantastic banana cakes and tea. I am grateful for your unwavering support and encouragement throughout the challenges I faced during this journey. I'm proud to see all your achievements and am always impressed by your hardworking attitude and consistency. Cannot wait to witness your defense, you'll do great, as always.

Liu for being such a cheerful officemate and friend. And thanks for always reserving me a spot in the food truck lines. **Alex**, your passion for physics and serious learning attitude is exemplary. **Gaia** for always being organized and caring, **Xiong** for amazing lunch discussion, **Yong** for the great knowledge, helps and fantastic sense of humor. **Jin** for mastering the Poland poker, always the winner! For all the unlimited hype and good vibes! **Luca**, for all the fun moments and deep chats. We both share similar passion for

theories. **Harmen**, for all the nice and joyful lunch breaks. **Jan**, for all the laughter and fun moments in Chamrousse, Klooster, Bierfabriek, and fresh air breaks. I won't forget the microscope image of living samples, hilarious! You're a knowledgeable scientist and have a wonderful personality. I always enjoy our nerdy physics discussions and I am happy that I had the chance to also connect with you outside work as well. And I am happy that we still work together in the Quantum Acoustics team!

Lorenzo, you were always a kind friend to me. During many ups and downs. I'm proud of all the science we did together, all the passionate chats about physics, beam splitters, qubits, about life, about music, Beatles, pizza nights, jam sessions and everything! I learned tooons from you.

Jana, fabrication master, our qubit producer, organized, beautiful soul, kind, smart, fuuuunnnn, and always ready to help, listen and support. A safe person who is always there to go to. I'm extremely delighted that we grew closer. We share a lot. We started as colleagues and after some time you became not only a close person in my life, but an excellent student in music. I will keep progwashing you for the rest of your life, until you become a proper prog fan, and who knows, maybe one day you appreciate Jazz and dislike Techno! I won't be surprised :D. I am thankful, from the bottom of my heart, for all the calming supports, listening, understanding, house parties, singing and driving in French Alps, snow balls, for being such a good gig buddy, for all the thoughtful gifts and surprises and all the good things we've had along the way!

Emanuele, Manuuuuuuuu! My fresh air body. Co-founder of Journal Club. Klooster pact. I'm not gonna mention Innsbruck sauna, don't expect that one! Chess master, sporty. Thanks for all the positive feeling and energy you brought to my life. Thanks for being such an energetic and cheerful friend. I specially enjoyed the remarkable trips we've been together. Plus our trio nights. Plus journal club outings, games and everything. Plus the best game ever, POLAND POKERRRRRRR!!! You turned our lives completely upside down after introducing us to that game! Can't get enough of that! No one ever could!

Last but not least, I want to thank our secretaries **Karin and Maria**. Many things would have been impossible without you.

QPhoX folks

Alex you were always a close and supportive friend, with such a fun vibe. **Martin**, amazing guitarist and singer. I enjoyed our jam sessions, drinks and all these good moments together. Thank you for all the incredible helps in our qubit project. **Pim, Thiery and Nandini** for always bringing joy, and all the technical supports in lab and cleanroom. **Chris** for amazing chats, hints, advices and everything.

And to all the people in QN and Qutech. You proved that the excellence of a place is not measured by the appearance of its exterior, but by its people!

Sabrya, for helping me organizing and doing the paperwork for my defense. **Gesa**, the incredible assistance with my summary. **Sonia**, for the amazing happy attitude, lunch breaks, all the joy you brought to the department, all the elaborate advertisements of house cleaning robots, and for remembering me whenever you see the soft ice cream machine. **Tino**, for all the technical supports, and incredible knowledges. **Eliska**, for the Machine learning course and always being a help for simulations/codes. **Arash and Vini**,

for all the helps for the cluster, all the follow ups and time you dedicated to teach me how to use it. **Abel**, for the calmness and exciting chats about sky-diving, and healthy diets. **Rasa and Mattias**, for all the laughter, all the cute "persian" chats. **Patrick**, for all the outings we've had, for all the posh culture discussions and etiquettes, and always nailing the Halloween customs. **Lukas**, for the always-posh outfits, and all the passionate chats about guitars and jazz and music. **Samer**, for all the jokes and serious-but-cool personality. **Jasper**, all the ranting, and gossips, all the breaks in our office D109, all the helps with my defense bureaucracy. **Alex**, the best office mate ever! D109 misses you! A scientist by nature, run by curiosity, brilliant teacher, in the meantime always a friend to go to. For bringing all the good mood in the office, even whenever you were not at your best. All the jokes and laughs we had together. **Toeno and Yaroslav**, for organizing QN seminars. **Gary**, for all the knowledge, all the good perspectives in science. You taught us how things, if understood deeply, can be explained simply - with a spring and mass. And also, thanks for all the fantastic QN events. **Fred**, for the constructive mindset, smart and wise, enthusiastic about physics. **Ulderico**, all the laughs and fun rantings and chats. **Brecht**, for always wearing a beautiful smile and a happy face all the time, always energetic and filling everywhere with positivity. **Michael**, we share similar passion and taste in music. From all the nerdy chats about Djent, guitars, Schecter, 8 strings, to dancing to techno in Veldhoven. Thanks for sharing all these great moments, including our small breaks and chats about life and work and mental health and relationships. **Clinton**, brilliant scientist, always up for physics questions, diving deep into the problems, sharing all the great achievements in the projects and lab, and of course, the fun in Veldhoven. **Jean-Paul and Ines**, for their sweet personality and all the fun we had together in conferences all over the world. **Jacob and Sercan**, for all the helps setting up the uW setup in our lab. **Robbie**, a good and helpful lab neighbour. **Thijs**, a seasoned drummer, good at counting and polyrhythm. For all the wonderful jam sessions. **Onima**, whenever we chat, I always feel like I've been knowing you for years! All the great sense of humor, expert dancing, being FUNNNNN. **Daniel**, all the chats about camping and festivals. **Raymond**, for the Electronics course, for all the helps designing and improving the SNSPDS circuitry in our lab. **Sjoerd**, always ready to have fun, and always smiling and showing good mood! **Deza**, for the melodious voice, for the laughs and fun you bring. For organizing QN gatherings at psor. Also I want to thank all the people in the workshop specially **Ronald**, who helped us designing and fabricating the equipments in our labs in all these years.

To all the people who made the impossible, possible, in nanoscale level. To our exceptional Kavli nanolab cleanroom team.

Eugene, for his dedication, supports, helps and for all the trainings in the cleanroom, teaching us how to work with chemicals. For his kinda heart. **Charles**, for all the technical supports, always supportive and friendly. **Arnold and Anja**, for all the guidance with the ebeam, helping us making the nanoscale patterns. **Marco**, for notifying me whenever my cleanroom access was about to expire :D. **Roald**, for always being passionate about plasma physics, always a good tutor, with detailed explanations. And of course all the chats about death metal and black metal music. **Hozanna and Lodi**, for showing us how to see better, finer, with higher resolution, with greater precision and detail. **Marc**, for all the managements, helps and supports.

To the Mohsens! **Amirali**, Kohsin! First interaction, 2010, asking for my thermody-

namics notes. Flash forward, 2018, our giggles and jokes in non-linear optics class and talking passionately about quantum optics. Koocheh Fatemi, comfortably numb. Flash forward, 2022, Ventura, sharing a room, GRC conference. Flash forward, 2023 hiking in vineyards of Switzerland. 2024, around new year, BBQ in NL. And here we are now! I cannot express how blessed I feel that I have had you all these years by my side. In all the moments of my life. Ups and downs. We've journeyed through numerous years together, and many more lie ahead! Here is a big thank you to you, from the bottom of my heart!

Keyvan, Mosi! Writing down the scores in excel, in Olympiad summer school, 2012. Few years later, dancing and partying. Singing "Writing's On The Wall - Sam Smith", "Sway - Dean Martin", "Boarder line - King Krule" 2020, Delft and Amsterdam. Living together in a place we used to call home. Gina and tonic. Best Burrito in town, despite its sourness! Words cannot express how much I've missed you, and how grateful I am that I have a friend like you!

Kamran, driving and singing around Interlaken with Fariba and Mohsen, and then KFC & concerts. Opeth, Alter Bridge, Soen. More to come. The house parties, persian dances. *Jaaaaaan*. our ouches! *AAAAAAAKKKH!* Mohsen enough to be one! Intelligent, mature, always got my back, fun, kind heart, a friend! Whatever friendship is, You are the living embodiment it!

Ramin Agha, Sotooon. From lunch next to Ebnes, to introducing *THE* "blue" jacket to me, to all the trips, BBQs, board games, COD warzone, Dune, Oppenheimer, dancing to Black Cats, and traumatizing me with blind date shows. We share a lot in common, we've always had - except the passion for rubbish shows.

Yosra, people have mistaken us as siblings multiple times! Rightfully so! You were indeed the sister I've never had! Always fun, always bringing laughter. Thank you for all the life advices, for all the supports, for helping me when I had challenges. And for always finding my jokes funny :)

Khatereh, we've shared many years together and I am grateful for it. For all the cafes, panah, exit, park mellat, to Barsil. And for the joyful and beautiful life I had with you. Thank you! **Dr. AmirH**, for all the philosophical discussions. For always being calm and wise. I learned a lot from you. For organizing the amazing trips in Scotland, the Karaoke bar, and Inverness that we never made it to! **Parvin Khanoom**, for all the kindness and delicious food. For always being pure and loving me unconditionally.

Rajab, Seyed! For all the persian restaurant advertisement. For your amazing cuisine. For you passion about board games. For all the Dune discussions. You are always a go-to person for me, when I need a good friend to talk to. When I need someone to feel chill and calm with. Our friendship is rooted deep! **Parmida**, too close to be far. For all the gatherings at your place, when we were young back there. For all the dances to muse. Thank you for always checking up on me, even from the other end of the world. And for annoying me with Taylor Swift reels.

Sonakshi, the person who always brings people together. My unofficial paranymph of PhD, and an official paranymph in life. A friend who's always there to defend me. A lifetime therapist. Thanks for always tolerating my jumpiness and chaos. Thank you for being such a brilliant person in my life. For all the life advices. And for all the good people you brought into my life. For all the positive moments you made out of all those negativities. **Luca**, you taught me how to stay consistent and resilient by alternating be-

tween chest/arms and back/shoulders, while every day is legs day. I will keep these wise words in mind till my last breath MASTER. **Nicole**, for all the dances, laughing uproariously, for your talent in singing and for your amazing taste in music! For always pulling me up when I'm down and for all the kindness and hope you showed me in life. For always filling the room with such an energy and happiness. **Quentin**, you know sometimes I attribute songs with people. For you, I always think of Veridis Quo - Daft Punk. If you were a song, you would have been that, and you are what veridis quo is to me :). We were dancing to it on new year's eve, remember? With Nicole! Thank you for all those good moments, and for more to come. Your passion and dedication in cannabis is impressive! **Tina and Milan**, for all the kindness and warmth you bring, for all the happy moments, for all the gatherings, making Lego, and for always welcoming me. **Deniz**, for your big heart, for always being a good listener, an understanding friend. **Stephan**, for your amazing cocktails, for all the deep chats about phonons and electrons, for your awesome personality. **Stefan**, I'm always impressed by your enthusiasm in Sci-Fi. And also, thank you for your educative explanations of Bio-science. **Luigi** for your distinct jokes and humors.

Ursa, for singing Country Road, but the Slovenian version, Siva pot. For teaching me Salsa dance. **Rishabh**, for all the great moments we had together, for the fantastic board game nights. **Wouter**, for making me one of the best persian Fesenjoon dishes I've ever had.

Fatemeh and Alireza, Shahla va Seyyed! From Tarasht and Bandari, to Fancy dinner in Paris. For your big hearts, for showing your love to me unlimitedly. For supporting me and calming me when I was all over the place.

Belen and Bart, For all the joy you brought into my life. Everyone needs a friend like you. **Nikoletta**, for sharing your music with me. For being such a talented artist, for the jamming.

And to all those with whom we've bonded through music.

Suyash, for your Petrucci taste, for all the shredding together, all the jam sessions, Djent counting, all the recordings. **Danni**, for your chill vibe, nerdy chats, Lofi vibe, always sharp in music and guessing the key, for everything I learned from you. We started as jam buddies and I'm delighted that we grew closer and formed a good friendship. **Keyhan**, for your dedication to our jam sessions, for your amazing vocals, for gathering us together, for all the efforts in organizing jam sessions.

Last but not least, my beloved family. I owe the most gratitude to you.

Maman Roya, you are a loving mother, a wise advisor, and a caring friend. Since my childhood. I am blessed for having such a treasure in my life. Thank you for always being sharp on my studies, for always encouraging me to live my potentials. **Baba Mojtaba**, a supportive father whom you can always rely on. Thank you for all the love you gave me, for all your supports, for working hard for our family. **Daei Mohammad**, for all the emotional and academic supports throughout all these years. For being such an exemplary academic and role model for me. You showed me the true meaning of dedication and hardwork and passion. You've shown me that no milestone is unattainable with hard work.

And to all the individuals not acknowledged here, forgive my oversight due to my

imperfect memory.

Sincerely yours, Amirparsa Zivari
April – 2024

"All alone or in twos
the ones who really love you
Walk up and down outside the wall"
[Pink Floyd - Outside the wall]